Doctoral Dissertations   Graduate School

Winter 2015

Improving practices in nanomedicine through near real-time pharmacokinetic analysis

Isidro B. Magana
Louisiana Tech University

IMPROVING PRACTICES IN NANOMEDICINE THROUGH

NEAR REAL-TIME PHARMACOKINETIC ANALYSIS

by

Isidro B. Magaña, M.S.

A Dissertation Presented in Partial Fulfillment
of the Requirements of the Degree
Doctor of Philosophy

COLLEGE OF ENGINEERING AND SCIENCE
LOUISIANA TECH UNIVERSITY

March 2015

ProQuest Number: 3664387
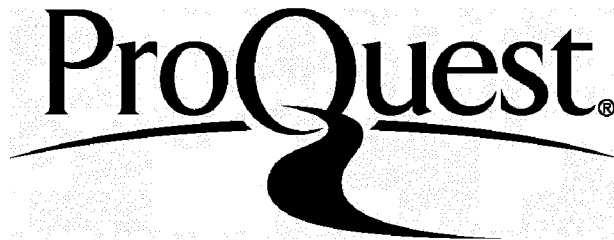
ProQuest 3664387

LOUISIANA TECH UNIVERSITY

THE GRADUATE SCHOOL

12 January, 2015
_____
Date

We hereby recommend that the dissertation prepared under our supervision
by Isidro B. Magana, M.S.
_____

entitled _____

Improving Practices in Nanomedicine Through Near Real-Time

Pharmacokinetic Analysis
_____

_____

_____

be accepted in partial fulfillment of the requirements for the Degree of
Doctor of Philosophy in Biomedical Engineering

_____
Supervisor of Dissertation Research

_____
Head of Department

Biomedical Engineering
_____
Department

Recommendation concurred in:

_____

_____

_____   Advisory Committee

_____

Approved: Approved:

_____   _____
Director of Graduate Studies   Dean of the Graduate School

_____
Dean of the College

ABSTRACT

More than a decade into the development of gold nanoparticles, with multiple

clinical trials underway, ongoing pre-clinical research continues towards better

understanding in vivo interactions. The goal is treatment optimization through improved

best practices. In an effort to collect information for healthcare providers enabling

informed decisions in a relevant time frame, instrumentation for real-time plasma

concentration (multi-wavelength photoplethysmography) and protocols for rapid

elemental analysis (energy dispersive X-Ray fluorescence) of biopsied tumor tissue have

been developed in a murine model. An initial analysis, designed to demonstrate the

robust nature and utility of the techniques, revealed that area under the bioavailability

curve (AUC) alone does not currently inform tumor accumulation with a high degree of

accuracy ($R2=0.56$), marginally better than injected dose ($R2=0.46$). This finding

suggests that the control of additional experimental and physiological variables (chosen

through modeling efforts) may yield more predictable tumor accumulation. Subject core

temperature, blood pressure, and tumor perfusion are evaluated relative to particle uptake

in a murine tumor model. New research efforts are also focused on adjuvant therapies

that are employed to modify circulation parameters, including the AUC, of nanorods and

gold nanoshells. Preliminary studies demonstrated a greater than 300% increase in

average AUC using a reticuloendothelial blockade agent versus control groups. Given a

better understanding of the relative importance of the physiological factors that influence

rates of tumor accumulation, a set of experimental best practices is presented. This

dissertation outlines the experimental protocols conducted, and discusses the real-world

needs discovered and how these needs became specifications of developed protocols.

APPROVAL FOR SCHOLARLY DISSEMINATION

The author grants to the Prescott Memorial Library of Louisiana Tech University the right to reproduce, by appropriate methods, upon request, any or all portions of this Dissertation. It is understood that "proper request" consists of the agreement, on the part of the requesting party, that said reproduction is for his personal use and that subsequent reproduction will not occur without written approval of the author of this Dissertation. Further, any portions of the Dissertation used in books, papers, and other works must be appropriately referenced to this Dissertation.

Finally, the author of this Dissertation reserves the right to publish freely, in the literature, at any time, any or all portions of this Dissertation.

Author _____

Date _11 February 2015_____

DEDICATION

This dissertation is dedicated to my family and friends for their help and support throughout my college career at Louisiana Tech University. Allie for her understanding and patience of my long work hours through the writing process- life as the dog of a PhD student can be ruff. My mother (Kathryn A. Magaña) and grandmother (Norma Allee) for their guidance, even through their personal battles with cancer. My father (Isidro Magaña) for instilling in my siblings and me a (as Rodney Shamburger once described it) "masochistic love of education". Without this love of education it is unlikely his three children would have, or be seeking, a PhD. Last and most of all, my two sisters (Anya R. Magaña-Jones and Kathryn V. Magaña) for having or pursuing a PhD, and therefore forcing me to get one to avoid being picked on at Thanksgiving every year, but slightly skewed to Katie for getting a non-engineering PhD.

TABLE OF CONTENTS

LIST OF TABLES

LIST OF FIGURES

ACKNOWLEDGMENTS

I would like to thank my committee: Dr. Patrick O'Neal, Dr. Katie Evans, Dr. Teresa Murray, Dr. Eric Sherer, and Dr. Mary Caldorera-Moore. All the members of my committee were always helpful not only with their time in the dissertation proposal and defense process, but also in experimental advice throughout my graduate career. I found that I communicated with each member of my committee regularly (compared to some of my peers this is rare) which was extremely helpful for me throughout my time in the graduate program at Tech.

In addition to the help of my committee, I would like to thank Dr. Sven Eklund for his help in the development of a new rapid elemental analysis protocol used for some of the experiments included in this body of work and Dr. James Spaulding for his help with the IACUC committee and his advice with the animal work.

The collaborative efforts of Nanospectra Bioscience, Inc. made my graduate work possible. The help of the team (including Dr. Jon Schwartz, Dr. Glenn Goodrich, and Kelly Sharp) in experimental design, troubleshooting, training, and general advice was invaluable.

CHAPTER 1

INTRODUCTION

1.1   Introduction to Cancer

Cancer is a blanket term used for several different diseases and types of conditions. These conditions all demonstrate an uncontrolled growth and potential spread of mutated cells. Cancer is observed across all genders, races, and ethnicities. Approximately 1,660,290 new cancer diagnoses and approximately 580,350 deaths from cancer are expected in the United States in 2013. This disease also carries a cost (in 2008) of $77.4 billion in medical costs and $124 billion in lost productivity. [1] Estimations based on current cancer research and clinical trials suggest that by the year 2022 the number of cancer survivors will increase from 13.7 million Americans in 2012 to around 18 million Americans. [2]

The nature of most tumors suggest that there is a problem in the regulations of tumor-suppressor genes, oncogenes and/or the apoptosis regulators. It is believed that it takes multiple mutations of the oncogenes and tumor-suppressor genes to result in malignant tumor. [3] Cancer cells demonstrate changes that lead to a defect in the normal regulatory systems of cell proliferation and homeostasis. [4] These problems with the cell proliferation and homeostasis are connected with a problem with the two pathways of apoptosis (Stress pathway, and death receptor pathway). [3]

Solid tumors account for approximately 85% of cancers, and are the subject of a large international research effort. [5] The successful outcome of tumor treatments often depends on physicians' experience and available techniques. [6], [7] Survival rates have improved over the past few decades with a one-year's survival rate going from 69.9% in 1975 to 81.8% in 2008, and a 10 year survival rate going from 41.9% in 1975 to 60.6% in 1999. [1], [2], [8] Tumors that are surgically accessible are removed. If surgical removal is not feasible, which can be the case for tumors that lie near sensitive tissues, such as head, neck, and brain, or those that have metastasized, often fall within the domain of radiation or chemotherapy. [9] Chemotherapy involves injecting an inherently toxic substance [10] and relies on the high metabolic activity of malignant cells to quickly absorb the chemotherapeutic agent. However, the uptake and retention of traditional chemotherapeutic small/macro-molecules can be hindered by abnormal blood and interstitial fluid pressures (IFP) in the tumors [11] and thus, even less systemically toxic agents (such as Herceptin), developed in recent years [12], can cause significant side effects.

Identified at least thirty years ago, the anatomical and physiological characteristics of tumors underwent much study in the 1980s [13], [14] and 1990s [15], but since these characteristics vary with tumor size, type, and location [16], [17], quantifying usable metrics to inform drug and nanoparticle design have been elusive. Although early empirical studies have identified the particle's size that provides substantial improvement over the weak uptake observed with macromolecules in some tumors [18], these studies are not general in form and do not necessarily apply to other particles or conditions.

Sensing and imaging technologies that are capable of quantitatively characterizing the scale of nanoparticles have enabled the development of the first round of nanomedical technologies at an experimental or prototype level. An examination of the literature and interaction with various companies currently involved in clinical trials suggest that the variability in the quality control of the manufacture, storage, and experimental protocols make comparisons difficult. [19]

Some of the nanomaterials currently found in the market for cancer therapies are nanocarrier-based drugs. A few examples are Zinostatin, Stimalmer, Oncaspar, Ontak, Zevalin, Bexxar, Myocet, and Abraxane. These carriers include protein conjugates, immunoconjugates, and liposomes. [20] Additional types of nanomaterials, such as Auroshells and Combidex, are currently undergoing clinical trials. These particles are gold nanoshells and iron oxide nanoparticles, respectively. [21] Gold nanoshells and nanorods have unique optical properties that allow for non-invasive, real-time monitoring of nanoparticle concentration in the blood. [22]–[24] However, whatever type of nanoparticle is chosen, of key importance in nanoparticle-based cancer treatment is the exploitation of the natural differences between cancerous and healthy tissue for the selective delivery to tumor cells in order to reduce damage to healthy cells. Indeed, some tumors present a unique physiology that distinguishes them from healthy tissue; in particular, they are characterized by an abnormal vasculature and the lack of functioning lymphatic vessels. [14] Studies have demonstrated that the vasculature of some tumors is quantifiably different from normal tissue in the lack of a complete basement membrane, abnormally large interendothelial junctions, permeability, and size [5], [14] and these differences are commonly exploited for passive delivery via the enhanced permeability

and retention effect (EPR). For example, the average pore cutoff size in tumors is much

larger (380–780 nm dia. [15]) than for normal blood vessels (10–20 nm dia. [25]) and

thus larger nanoparticles will be selectively absorbed in tumors over healthy tissue.

However, some other characteristics of tumor tissue, such as higher IFP than normal

tissue [26], lead to a less efficient delivery. Thus, a careful study of all these factors is

important in order to take better advantage of those properties resulting in an increased

delivery while minimizing the effect of those that would make the delivery less effective.

1.2   Nanoparticles in Development for Cancer Therapies

Several types of nanomaterials are currently under investigation in multiple stages of

preclinical and clinical trials for use in cancer therapies. Some of these nanomaterials

include liposomes and micelles (Doxil/Caelyx), polymer (Oncaspar), iron oxide

(NanoTherm), and gold nanoshells (Auroshell). [21] The nanomaterials are used due to

the ability to engineer specific characteristics to target tumors. Nanomaterials either

actively (by attaching molecules that bind to antigens or receptors on target cells) or

passively (by exploiting EPR) accumulate in tumor tissue. [20]

The EPR effect is a commonly found defect in the vessel walls of tumors. As tumors

rapidly grow the need for nutrients is significant, as a result healthy vasculature is unable

to keep up with the constant demand for more nutrients. The expansion of the vasculature

toward the tumor is supported by vascular endothelial growth factor and basic fibroblast

growth factor. An imbalance in the pro- and anti- growth factors leads to poorly regulated

expansion of the vasculature. This lack of oversight leads to poorly formed vessels and

defective basement architecture allowing larger particles and molecules to escape the

vasculature in these areas. These larger particles are not able to escape the well-formed (healthy or non-tumorous) vasculature. [27]

1.2.1   Active vs. Passive Tumor Targeting

1.2.1.1   *Passive Targeting*

Passive tumor targeting involves the EPR effect. This effect in combination with the poor lymphatic drainage creates an environment where specifically sized particles can preferentially accumulate, compared to normal tissue. This specific set of conditions is a result of the rapid angiogenesis necessary for the rapid and unchecked growth of tumor tissue. Research suggests that taking advantage of these factors alone particles up to approximately 400 nm are able to extravagate, but particles under 200 nm are most effective. [20] A model suggested that the pore size is more important than the particle size for effective extravasation. [28] Pore size (a factor in perfusion) can be modified by several methods including hyperthermia. [28], [29] Once in the target tissue the particle would complete an action it is designed to do, such as heat when energy (light or magnetic) is applied or release a chemotherapeutic agent.

1.2.1.2   *Active Targeting*

The purpose of active targeting is to avoid problems, such as poor perfusion, by designing particles to bind to specific cells after extravasation from the vasculature. This is typically done by attaching targeting agents (generally classified as proteins, nucleic acids, or receptor ligands) to the surface of the particle. These agents must be highly specific to the target tissue type, or the particle would complete its action on an undesired tissue. Some particles have such a high binding affinity that they have lost some penetration depth. [20] Active targeting techniques using surface modifications to gold

nanorods have demonstrated a small improvement compared to passive accumulated control groups. [30] This result brings up questions regarding the utility of active targeting and the importance of perfusion and injection route (regardless of targeting) in accumulation.

1.2.2 Types of Nanoparticles

1.2.2.1 *Liposomes*

Liposomes are spherical and made of a lipid bilayer, creating a core area potentially used for encapsulation of drugs. This method is advantageous due to the ability of the liposomes to preferentially accumulate in tumors due to the EPR effect. The preferential accumulation in tumors allows the chemotherapeutic agent in the liposome to be given in lower doses, and be less systemically toxic while retaining the desired toxicity and concentration in the target tumor. Liposomes also allow for the manipulation of properties such as size, drug release rate, bioavailability, and dosing schedule can increase efficacy while lowering damage to other tissues. The United States FDA first approved this type of therapeutic agent in 1990 as DOXIL (liposomal doxorubicin). [31]

1.2.2.2 *Hydrogel*

Hydrogels are network of cross-linked polymer chains that are hydrophilic and commonly used as tissue scaffolds. Several studies have been and are being conducted using cross-linkers that will degrade under specific conditions, usually to release an encapsulated drug. Tauro and colleagues have demonstrated potential use of poly(ethylene glycol) diacrylate (PEGDA) hydrogel nanoparticles to deliver chemotherapeutic agents to highly specific sites, and for use in treatment of glioblastoma. [32]

1.2.2.3   *Polymer*

Polymeric nanoparticles are developed and are similar in nature to the hydrogel

nanoparticles. In the same way as hydrogel nanoparticles, the polymeric nanoparticles are

being made from erodible polymers so when they erode they release an encapsulated

drug and then disappear. Poly(ε-caprolactone), poly(lactic acid), poly(glycolic acid) and

their copolymers are among the polymers under heavy investigation for use in cancer

therapies. Research on these nanoparticles is focusing on "smart" technologies, which

similarly to hydrogel nanoparticles, are sensitive to environmental stimuli. Some particles

will have active targeting toward a specific site and some will be passive targeting, but

triggered by site-specific conditions to release the encapsulated drug. Active targeting

will involve ligands and aptamers, and site triggering could focus on pH or thermo-

response. In addition, some particles could be produced with multiple "smart"

technologies. The use of polymeric nanoparticles could help in the location specific

delivery of chemotherapeutic agents, decreasing systemic toxicity and improving patient

outcomes. [33]

1.2.2.4   *Iron Oxide*

Ultrasmall superparamagnetic iron oxide (USPIO) nanoparticles have been evaluated

for use as an enhancement for magnetic resonance imaging (MRI). This contrast agent

would provide information to assist in the staging of axillary lymph nodes in breast

cancer patients. The Dextran-coated USPIOs demonstrated a half-life of 36 hours. The

use as a contrast agent due to uptake in normal lymph node macrophages and a lack of

uptake in tumor cells. [34]

1.2.2.5   *Gold Nanoshells / Nanorods*

Gold nanoshells are spherical particles with a dieletric core with a thin gold shell. The ratio of core to coating gives the nanoshell's tunable optical properties. [35] Gold nanoshells (diameter of approximately 155 nm) and nanorods (14 x 45 nm) have demonstrated utility in cancer therapies through the use of the tunable optical properties. One therapy involves the intravenous injection of gold nanoparticles and passive accumulation in tumor tissue. Once accumulation is complete the particles are exposed to a specific wavelength of light (by fiber optic), which excites and heats the nanoparticles, killing the tumor. This photothermal ablation of the tumor has two major advantages: killing the tumor along vascular lines (cutting the tumor off from its source of nutrients) and preferentially killing the tumor minimizing damage to healthy tissue surrounding the tumor. Once the tumor dies, the cells are disposed of by the immune system. [35]–[38]

1.3   Research Need & Presented Research

A goal for this research is to discover needs, and create specifications driven research to solve problems in pre-clinical and clinical implementation of gold nanoparticle driven therapies. This research is designed to answer questions about the use of gold nanoparticles that are applicable to clinical trials in the future. The results of each unique experiment will be used to construct a standard one compartment pharmacokinetic model. The use of near real-time pharmacokinetics will give us a unique and faster look at the physiological response to nanoparticles, giving us the ability to more rapidly make recommendations on treatments. Through these experiments, we will work to use pharmacokinetic parameters and models to make recommendations and create a set of "best" practices in cancer nanomedicine. These "best" practices should include a set of

standardized guidelines and specifications (shown in Table 1-1) to help in the design and

use of nanomaterials and implementation of near real-time pharmacokinetics.

Table 1-1: Real-world needs found during experimentation and design specifications of implemented solutions.

Real-World Need	Design Specification
Reliable Review of Data Quality	Save data for offline analysis
Uniform Data Output	MATLAB code for data quality review and creation of graphs and PK metrics
Loss of high quality pulsatile signal	Prevent loss of peripheral circulation by discontinuing anesthesia and keep animal in warm ambient environment
Ability for Rapid Blood Plasma Concentration Reading	Less than 5 minutes
NP Stains on Tail Interfere With NanoTracker Readings	Injection rate set to $\leq 18\mu L/min$
Tumor Uptake Data in Clinically Relevant Time Frame	Analyzed in less than 12 hrs.
Minimal Sample Prep for Elemental Analysis	Minimize "skilled" tasks to pipetting
Extended Circulation Nanoparticles	4-48 hr. maximum concentration in tumor
PK Metrics did not predict uptake	Quantify additional potentially important variables
Large Variation in maximum blood plasma concentration	Achieve ±10% of injection goal with 95% precision

The body of research presented in this dissertation is the product of iterative and

tangential improvements to rapidly develop protocols for use in translational pre-clinical

trials using gold nanoshells and nanorods in conjunction with clinical trials on gold

nanoshells. The flow of these experiments is shown in Figure 1-1, and the evolving list of

real-world needs and design specifications.
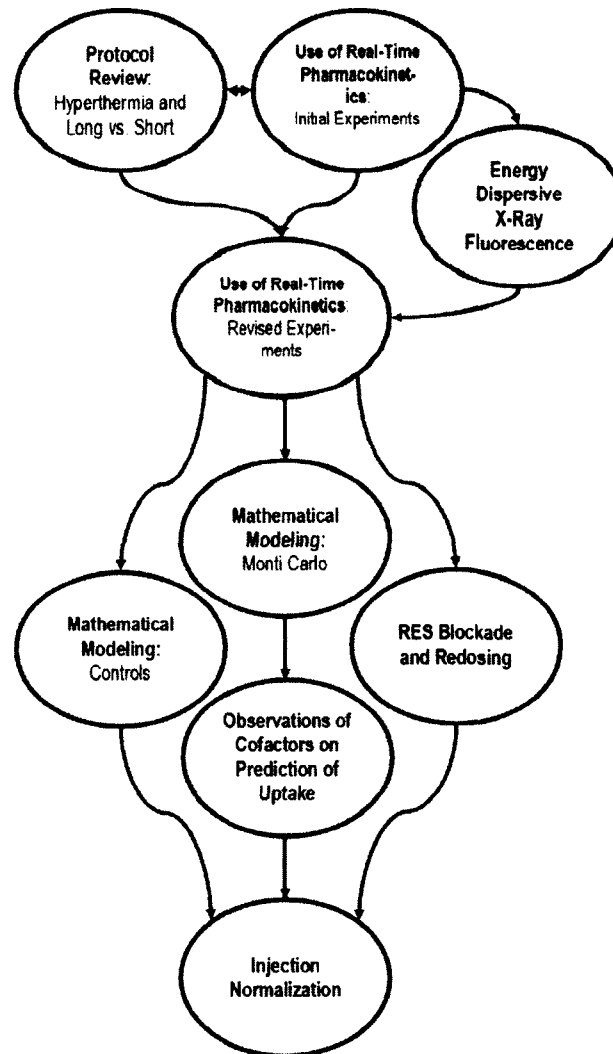
Figure 1-1: Flowchart to visualize experimental development.

The work started with a review of the standing pre-clinical protocols to

familiarize researchers with the protocols and make observations of improvements

(CHAPTER 4: Animal Protocol Review Using Gold Nanoshells). The recommendations

from this review were integrated into the work of both iterations of CHAPTER 6: Use of Real-Time Pharmacokinetics to Predict Tumor Uptake of Gold Nanorods. The initial experiments of CHAPTER 6: Use of Real-Time Pharmacokinetics to Predict Tumor Uptake of Gold Nanorods revealed a need to develop a rapid elemental analysis system to be able to observe a full set of data on one animal prior to the beginning of an experiment on another animal (and for future clinical work). This need for a rapid elemental analysis system lead to the work in CHAPTER 5: Development of an Energy Dispersive X-Ray Fluorescence (EDXRF) Technique for Elemental Analysis of Gold Nanorods, and this novel rapid elemental analysis technique was used in the revised experiments of CHAPTER 6: Use of Real-Time Pharmacokinetics to Predict Tumor Uptake of Gold Nanorods. The data from these revised experiments was used in three unique paths:

1) Can a control feedback system be created to control the injection phase? (Section 3.2: Mathematical Modeling- Controls)

2) Can adjuvant therapies affect the circulation pattern of nanorods during the accumulation phase? (CHAPTER 8: Reticuloendothelial System Blockade and Redosing of Gold Nanorods in a Murine Model)

3) This data set was used as experimental data for the confirmation of the Monte Carlo model presented in section 3.1: Mathematical Modeling- Monte Carlo.

The Monte Carlo model presented in section 3.1 suggested some parameters (pore size, particle size, blood plasma concentration of NPs, and blood pressure) of the model could affect the delivery of NPs to a solid tumor. Some of these parameters became the focus of our next study: CHAPTER 7: Observation of Cofactors on Prediction of Tumor Uptake of Gold Nanoshells.

The large variation of observed peak NP blood plasma concentration in the Observation of Cofactors on Prediction of Tumor Uptake of Gold Nanoshells CHAPTER 7), development of the control feedback system (Section 3.2), and the study of Reticuloendothelial System Blockade and Redosing of Gold Nanorods in a Murine Model (CHAPTER 8) demonstrated a need for more uniform delivery of NPs. This need for uniform delivery spurred the need for improved injection protocols (Section 10.1) and to make uniform delivery by observed blood plasma concentration enabled by the NanoTracker (CHAPTER 9: Injection Normalization). These studies combined have led to the development and improvement of pre-clinical protocols for the utilization of real-time blood plasma concentrations to improve the development of individual and population pharmacokinetic models of gold nanoshells and nanorods in a murine model.

CHAPTER 2

LITERATURE REVIEW

2.1   Gold Nanoshells and Nanorods

The gold nanoparticles (nanoshells and nanorods) discussed in this dissertation

are provided by Nanospectra Biosciences, Inc. (NBI). Their nanoshells are currently in

multiple pre-clinical and clinical trials under an investigational device exemption (these

nanoparticles do not chemically interact with the body and are therefore classified as

devices, not drugs). The nanoshells are approximately 150 nm in diameter with a mPEG

coating, stored in an iso-osmotic solution of 10% trehalose, and produced in the manner

described by Oldenberg and colleagues. [39], [40] Biodistribution of these gold

nanoshells has been conducted, and will not be evaluated in the experimental section of

this dissertation. James and colleagues demonstrated that at 1 day the gold was primarily

found in the organs of the RES (Liver- 311 PPM, Spleen- 1890 PPM). [40]

The gold nanorods provided by NBI are approximately 15 x 45 nm, PEGylated,

and suspended in an iso-osmotic solution of 10% trehalose. The nanorods are synthesized

using a modified version of the method developed by Jana and colleagues [41] described

by Goodrich and colleagues . [37] Biodistribution of these gold nanorods has been

conducted, and will not be evaluated in the experimental section of this dissertation.

Goodrich and colleagues demonstrated the primary accumulation of gold after one day

13

was in the organs of the RES (liver approximately 77% of injected dose and spleen approximately 6% of injected dose). [37] Tucker-Schwartz and colleagues used photothermal optical coherence tomography and PEGylated gold nanorods of similar size (synthesis roots that trace back to Jana and colleagues [41] through Murphy and colleagues [42]) to monitor the accumulation and dissipation in mammary tumors, and found the maximum accumulation to be at 16 hours. [43]

2.2   Clearance of Gold Nanoshells and Nanorods

Nanoparticles are subject to rapid opsonization by complement and other proteins. This opsonization is followed by removal from the blood by hepatocytes (particularly particles <100nm) and macrophages of the reticuloendothelial system (RES) within seconds of injection (creating short half-lives incompatible with passive targeting). [44], [45] The Kupffer cells (tissue macrophages of the liver) are unable to directly detect foreign bodies in the blood, so this process requires the opsonization of the nanoparticles while they are circulating. Opsonins found on liposomes (a nanoparticle of similar size and shape to gold nanoshells) fall in two categories: immune opsonins and non-immune opsonins. Immune opsonins include immunoglobulins, complement-related proteins (C-reactive protein, serum amyloid P, or mannose-binding protein) and components of the complement system (such as C3, C4 and C5); non-immune opsonins include serum proteins (such as albumin, α2-macroglobulin, apolipoproteins, laminin, fibronectin, etc.). [44], [45]

The interactions of complement and liposomes have been investigated but never fully understood. Some of the approaches taken to investigate these interactions include measurements in plasma complement levels (through systems like ELISA and

radioimmune assays) or changes in liposome structure (by release of a drug or molecule from the liposome); the latter demonstrates fewer parallels to gold nanoshells. Multiple studies have demonstrated the activation of complement through the classical pathway, through both antibody-dependent and antibody-independent methods. Some studies have demonstrated a difference in activating the classical or alternative pathway dependent on cholesterol content of the liposome. Scieszka and colleagues have demonstrated opsonization dependent on heat-labile serum components, and that C3bi was responsible for opsonization and uptake was enhanced by C5a. C3bi protein was proven responsible through experiments using serum-lacking C3. The activation of the complement system through intravenous injection of liposomes has also demonstrated sever anaphylactic reactions. These reactions can be mediated through improving administration techniques (such as adjuvant therapies or injection rate). [45]

Once a particle has been opsonized one of three methods are commonly used to make the phagocytic cells recognize the particle. The first method involves conformational changes of attached opsin proteins from an inactive to an active protein that is recognized by the phagocytic cells. The second method involve the attachment of a phagocyte to the particle by non-specific adherence to blood serum proteins. The third method involves the activation of phagocytes attracted to the activated complement proteins attached to the particle. [44]

2.2.1   PEGylated Nanoparticles

Charged and hydrophobic particles are more rapidly and efficiently removed by the reticuloendothelial system, compared to electrically neutral particles. This high removal rate created a need to make the particles electrically neutral or hide the particles

by adding a surface coating. [27] Masking nanoparticles from the RES is necessary to increase the circulation time to a period long enough for passive accumulation. This need created a group of "stealth" nanoparticles. The most common surface coating for stealth nanoparticles is polyethylene glycol (PEG). A form of PEG (DSPE-PEG) has been used to demonstrate a concentration dependent suppression of opsonizing proteins, and chol-PEG or PE-PEG have been used to demonstrate a concentration dependent ability to inhibit binding of C1q with the ability to almost eliminate the binding at high enough concentrations. [45] PEG uses steric hindrance to prevent the adsorption of opsonins and delaying the uptake by phagocytic cells. PEGylation of nanoparticles is a common method of evasion of the immune system and used in liposomes, polymeric nanoparticles, gold nanoshells, and gold nanorods. PEG has several problems including liposomes demonstrating a lower tumor accumulation compared to non-PEGylated liposomes, and PEG is responsible for the accelerated blood clearance found upon repeated injections of PEGylated nanoparticles. Given the known problems with PEG, other surface coatings (Polyoxazolines, Poly(amino acids), HPMA, Polyetaines, Polyyglycerols, or Polysaccharides) should be considered. [27]

2.2.2   Accelerated Blood Clearance (ABC)

Upon repeated injections of PEG liposome, a significantly shorter circulation half-life was noted; if the repeated injections were given after a long enough delay the pharmacokinetics returned to a similar to normal state. This phenomenon could be transferred to other mice through transfusion of serum, suggesting a soluble serum factor was the cause. [46], [47] Some studies point to PEG as the source of the ABC phenomenon, however a change in PEG (density or length) can prevent ABC. [45] The

importance of this phenomenon depends on the use of the particular nanoparticle. If the therapy is a one shot therapy, i.e. if the therapy can only be used once, it is not important what the immune response would be to repeated injections. In the case similar to the repeated doses of DOXIL administration should be spaced appropriately to improve the therapeutic index. [47]

2.2.3   Anti-PEG Immunoglobulin

Studies have suggested, through experimentation using "empty" PEGylated liposomes, that a peg specific IgM (known to exist since 1983) contribute to the ABC phenomenon. [48], [49] Ichihara and colleagues suggest that the mechanism responsible for ABC could be anti-PEG IgM released after the initial dose of PEGylated particles binds to a subsequent injected dose of particles. When the IgM attaches to the second dose of particles, the complement system is activated and the opsonization of particles that have activated C3 fragments. The attachments of complement and IgM create a rapid clearance of the particles through the Kupffer cells of the liver. [50]

Experiments have found PEG acts as a type two T cell-independent antigen and primes the B cells in the marginal zone of the spleen. This result was found through elimination of marginal zone B cells through the use of cyclophosphamide. The T cell-independence was discovered through the use of nude mice. Marginal zone lymphocytes were eliminated through the use of cyclophosphamide eight days prior to the injection of liposomes and serum was collected five days after the injection of liposomes. ELISA procedures were used to investigate presence of IgM and IgG, which demonstrated a low level of anti-PEG IgM and IgG (implying the importance of the marginal zone B cells in production of anti-PEG immunoglobulins). A separate study showed anti-PEG IgG at

three to five days and anti-PEG IgM three to ten days after the injection of liposomes,

with a peak concentration around five days. Both IgM and IgG levels returned to normal

by fourteen days after the initial injection of liposomes. The investigation of

immunoglobulin response in the absence of T cells was conducted using nude BALB/c

mice, and demonstrated anti-PEG IgM ten days after the initial injection of liposomes.

Implying a T cell-independent mechanism for the production of anti-PEG IgM. [48]

Through experimentation, Ishida and colleagues were able to establish a T cell-

independent anti-PEG IgM response. This finding was discovered when anti-PEG IgM

was found in nude mice and not in SCID mice, suggesting the important mechanisms for

creation of anti-PEG IgM were in the B-cells and not in the T-cells. Additional injections

of liposomes did not cause isotype switching from IgM to IgG. These findings support

PEG acting as a type two T cell-independent antigen, and contribute to the current

understanding that B cells of the spleen are the critical component in the ABC

phenomenon. The T-cell independent antigens (PEGylated particles in this case) did not

induce memory B-cells that produce IgG, explaining the loss of the ABC phenomenon

given enough elapsed time from initial injection to subsequent injection. Testing for T

cell-independence involved testing using three groups of mice: normal, nude, and SCID

mice. The levels of serum immunoglobulin was similar in normal and nude mice, but for

all practical purposes absent in SCID mice, suggesting the T cell-independence.

Experiments conducted to suggest the importance of the spleen involved the removal of

the spleen from rats and subsequent injections of liposomes; results showed

immunoglobulin production was reduced in rats with no spleen. Liposomes were

repeatedly injected at seven day intervals to demonstrate the T cell-independence of PEG

as an antigen. This study showed the first injection to result in the maximum anti-PEG

IgM production, limited isotype switching, and no generation of B cell memory;

implying, T-cell independence. Serum samples for all the experiments were collected five

days after injection of PEGylated liposomes and separated by centrifugation using serum

separating agents. [50]

Studies have been conducted to elucidate if ABC is caused by an increase in

phagocytic activity of liver macrophages or if an increase in efficiency of opsonization is

to blame. Rat livers were perfused with PEGylated liposomes designed to cause optimal

ABC. With the absence of serum in the solution, no improved liver uptake was noted.

This finding suggests the liver uptake is not changed but the opsonization is. In addition,

procedures were followed to heat treat the serum; the results demonstrated a lower

serum-dependent liver uptake. These findings demonstrate the first dose of PEGylated

liposomes do not increase the activity of the Kupffer cells, and complement activation is

responsible and essential for ABC. [51]

2.3   NanoTracker

The NanoTracker is a non-invasive device developed to give near real-time

optical monitoring of intravascular nanorods and nanoshells. This device works on the

same basic technology as a pulse oximeter, pulse photometry. Michalak and colleagues

says "We develop a pulse photometer capable of accurately measuring the

photoplethysmogram in mice and determining the ratio of pulsatile changes in optical

extinction between 805 and 940 nm, commonly referred to as R. these wavelengths are

selected to correspond to the extinction properties of gold nanoshells". [23] Michalak and

colleagues later describes the instrumentation involved. "Our device consists of a probe

compatible with mouse anatomy, analog circuitry, a data acquisition card, and LabVIEW

software". [23] The probe includes an LED that emits at four unique wavelengths (660,

735, 805, and 940). This LED is purchased through Marubeni out of Santa Clara,

California. Only the 805 and 940 nm wavelengths are used in the probe. A photodiode

(Hamamatsu Hamamatsu City, Japan) is used on the other side of the subject to record

the changes in emitted light through the subject. The additional analog circuitry consists

of filtering and timing systems, among other things.

The NanoTracker, a multispectral pulse photometer, is commonly used for mice

under light anesthesia or no anesthesia to detect the intravascular concentration of

nanorods. The NanoTracker helps by providing the levels of nanoshells or nanorods in

the vasculature, displayed as optical density. The NanoTracker does this by observing

pulsatile changes in optical extinction between 805 and 940 nm, and calculating a ratio

between the wavelengths known as R shown in Eq. 2-1, where V_{AC} is the alternating

current voltage, V_{DC} is the direct current voltage, λ_1 is wavelength 1, and λ_2 is

wavelength 2. [23]

$$R = \frac{log\left(\frac{V_{DC}}{V_{DC} - V_{AC}}\right)_{\lambda_1}}{log\left(\frac{V_{DC}}{V_{DC} - V_{AC}}\right)_{\lambda_2}} \sim \frac{\left(\frac{V_{AC}}{V_{DC}}\right)_{\lambda_1}}{\left(\frac{V_{AC}}{V_{DC}}\right)_{\lambda_2}} \qquad \textbf{Eq. 2-1}$$

The NanoTracker then simultaneously solves Eq. 2-2 and Eq. 2-3 to solve for the

optical density of the nanorods (OD_{NR}) and oxygen saturation (S), using the R values,

effective attention coefficients of oxygenated whole blood ($\mu_{Hbo_2}^{\lambda}$) at wavelength (λ), and

effective attention coefficients of deoxygenated whole blood ($\mu_{Hbo_2}^{\lambda}$) at wavelength (λ).

$$R_{805/940} = \frac{S\left(\mu_{HbO_2}^{805}\right) + (1-S)\left(\mu_{Hb_r}^{805}\right) + \mu_{NR}}{S\left(\mu_{HbO_2}^{940}\right) + (1-S)\left(\mu_{Hb_r}^{940}\right) + 0.20180D_{NR}}$$ **Eq. 2-2**

$$R_{660/940} = \frac{S\left(\mu_{HbO_2}^{660}\right) + (1-S)\left(\mu_{Hb_r}^{660}\right) + 0.3523\mu_{NR}}{S\left(\mu_{HbO_2}^{940}\right) + (1-S)\left(\mu_{Hb_r}^{940}\right) + 0.2018\mu_{NR}}$$ **Eq. 2-3**

The use of the NanoTracker allows us to obtain as many data points on the blood plasma concentration curve as we would like, rather than being restricted by the amount of blood we can safely draw from the mouse for *ex vivo* optical density measurements. This ability to obtain as many data points as desired is advantageous so we build a more reliable blood plasma concentration curve. Another main advantage of the NanoTracker is the potential for use in near real-time applications of pharmacokinetic models and feedback controls during nanoparticle infusion.

2.4 Pharmacokinetics

"In Brief, pharmacokinetics is concerned with quantitatively accounting for the whereabouts of a drug after it has been introduced into the body. The analysis is carried out through the entire time course for the drug in the body". [52] The importance of pharmacokinetics is not always apparent; however, until the full biodistribution of nanorods is fully understood we will not be able to even speculate at what toxicity problems could be faced. Even basic pharmacokinetic modeling is not a trivial task. This section discusses two basic models, the one compartment and population pharmacokinetic models. More advanced model such as a physiologically based models would be beneficial for a better understanding of the biodistribution. Physiologically based pharmacokinetic models typically include significantly more compartments to account for more biological systems. De Jong and colleagues conducted biodistribution studies, and demonstrated a presence of

gold nanoparticles (of multiple sizes) in the blood, liver, spleen, lung, brain, heart, and

kidney at 24 hours. [53]

2.4.1   One Compartment Model

A one compartment non-physiologically based model, shown in Figure 2-1, is

currently being used due to the availability of data. The one compartment model for the

experimental data would represent the blood volume of the mouse. Concentration of

nanoparticles in the blood volume of the mouse is available in the form of experimental

data. The blood volume in a twenty-gram mouse is approximately 1.44 mL or 72 ml/kg.

The model uses Eq. 2-4 to give a concentration as a function of time.
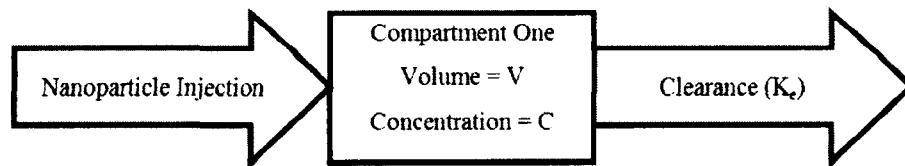
Figure 2-1: Box Diagram demonstrating one compartment model.

$$C = C_0 e^{-k_e t}$$ **Eq. 2-4**

Where C is the concentration, C_0 is the initial concentration, k_e is the elimination

rate constant, and t is time. The initial concentration is calculated using Eq. 2-5.

$$C_0 = \frac{D}{VOD}$$ **Eq. 2-5**

Where D is the initial dose and VOD the volume of distribution. Using this basic

model the half-life $(t_{1/2})$ is calculated using Eq. 2-6.

$$t_{1/2} = \frac{\ln(2)}{k_e} = \frac{0.693}{k_e}$$

<div align="right">Eq. 2-6</div>

This model demonstrates the removal of the nanoparticles from the blood as a function of time. This model does not account for differences in the accumulation or release of nanoparticles from tissues, but only the overall removal of the nanoparticles from the blood.

Other models, such as two compartment physiological models, would provide a better model of the movement of nanoparticles. These models would depend on the availability of real-time data reflecting accumulation in target tissues.

2.4.2   Population Pharmacokinetics

Population pharmacokinetics (popPK) investigate the variability between subjects given the same treatment, also referred to as inter-subject variability. The focus of popPK involves studying and attempting to account for the inter-subject variability in terms of subject specific variables, such as age, sex, or weight. Studies often do not collect enough data for the pharmacokinetic parameters of an individual to be calculated. This lack of available data has skewed the meaning of popPK to focus on analysis involving scarce data. The developed popPK analysis techniques are applicable to studies with ample data, but become a more valuable source of analysis in studies with scarce data. The nature of sparse data does not allow for traditional analysis techniques. The need for novel analysis techniques created several approaches such as nonlinear mixed effects modeling (Beal & Sheiner 1982), non-parametric maximum likelihood (Mallet 1986), Bayesian (Racine-Poon & Smith 1990). Nonlinear mixed effects modeling is the most popular method, due in part to the software package NONMEM. [54]

The title popPK conspicuously points toward the primary focus of the analysis

techniques, populations not individuals. [54] This focus is a counterintuitive connection

with nanomedicine, where the focus is individualized medicine. However, the ability of

popPK modeling to reveal sub-group specific effects (observed through covariates) can

help the clinician choose have more realistic expectations of treatments should start to

obtain the desired outcome.

2.5   Elemental Analysis

Experimental studies in nanomedicine employ different types of metal

nanoparticles. For example, gold nanoparticles are being used in animal and human trials

for assessing the feasibility of photothermal ablation of inoperable solid tumors. [21],

[35], [55] A potential way to enhance efficacy in such cancer therapies is to increase

feedback through additional clinical signs during the accumulation and treatment phases.

Nanoparticle systems could be coupled with individualized pharmacokinetics and

elemental analysis of ex vivo tissue to confirm uptake and retention into the tumor.

Concurrently, innovative medical devices are being developed to provide near-

instantaneous pharmacokinetic feedback, [23], [36] suggesting the need for an elemental

analysis technique that provides similarly rapid quantitative feedback of biodistribution.

These analyses could assess when, and to what degree, the particles were accumulating in

the tumor, or if they were being eliminated by the RES. The use of rapid elemental

analysis coupled with real-time pharmacokinetic [23], [36] measurements could help

predict the most appropriate time for animal or human ablation (e.g. photothermal) of the

tumor. For animal studies, a faster technique can have a major impact for companies

involved in nanomaterial quality control and product development. For human trials, the

ability to measure, or predict, the accumulation of the nanoparticles in the target tissues could improve treatment outcomes for some of the approximately 52,000 anticipated deaths due to cancers targeted by this therapy each year, in the United States. [1]

Biodistribution of gold nanorods is normally analyzed through inductively coupled plasma mass spectrometry (ICP-MS) or instrumental neutron activation analysis (INAA). [30], [37], [40] ICP-MS requires elaborate and time-consuming sample preparation (up to 104 hours). [56] INAA does not require a long sample digestion and preparation, but requires longer analysis. [40] Although both of these techniques are accurate, they take from days to weeks to get results, longer than a clinical treatment time of one day. If the data were available within the clinical treatment time, we hypothesize that some accuracy could be sacrificed compared to these standard methods.

Energy Dispersive X-Ray Fluorescence (EDXRF) is a technique used for bulk and ppm elemental analysis that is rapid, robust and requires little sample preparation time. [57] EDXRF has been previously used for quantitative in vivo and ex vivo analysis of gold in tissues like kidney and liver. [58], [59] Previous work with biological samples demonstrates the need for thin samples, so that matrix effects can be neglected. [60] Common EDXRF protocols require a long process of drying, crushing, and pressing samples into pellets. [60], [61] Based on guidance from the literature towards optimizing a rapid sample preparation, the key aspects of this protocol include: sample thickness, geometry, and homogeneity. [60]

CHAPTER 5 outlines the procedure developed for a benchtop EDXRF elemental gold analysis of gold nanorods ($\approx$ 15 x 45 nm), an optically absorptive cylindrical nano-object used in nanomedicine. [37], [62] The protocol presented in CHAPTER 5 includes

tissue digestion/homogenization in potassium hydroxide followed by desiccation in the

sample cup before EDXRF analysis. Using subcutaneous mouse tumors, the elemental

analysis was completed in less than 12 hours from the time of tissue collection.

CHAPTER 3

MATHEMATICAL MODELING

The results of CHAPTER 6 demonstrated poorer than expected correlations between tumor uptake and standard pharmacokinetic metrics. This less than optimum correlation generated a desire to observe additional variables. To find these variables we turned to collaborative modeling efforts, and then continued with experimental verification in CHAPTER 7.

Many people have used mathematical modeling of tumor and tumor vasculature toward different goals. Jain and colleagues used a model, established by their lab in 1988, to study the changes on interstitial fluid pressure based on changes to "normalize" the vasculature. [63] Chapman and colleagues used their modeling efforts to examine the fluid flow through the leaky vasculature of the tumor. [64] Frieboes and colleagues used a mathematical model to understand some of the variables that may help to explain tumor growth and invasion. [65] Howard and colleagues demonstrated the use of the unit density sphere model as a practical alternative for clinical use compared to the computationally demanding but more accurate Monte Carlo algorithms. [66] Soltani and colleagues used a computational fluid dynamics simulation based on previous works to study some of the changes in pressure and introduced new parameters in this model. [11] Goh and colleagues worked to develop a two-dimensional simulation platform to

27

demonstrate the transport of Doxorubicin to hepatomas, an elaboration of previous work. [67]

Goh and colleagues worked to create a two-dimensional simulation from a one-dimensional simulation. The goal was to be able to explore the special and temporal variations of doxorubicin concentrations and the penetration into the tumor and healthy tissue. Other areas this model was designed to study are lymphatic drainage, and intracellular kinetics. They were able to show that changing the injection volume does no result in significant changes in drug concentration in the tumor or healthy tissue. They also found that diffusion is the main transport mechanism of free doxorubicin. Goh says that some ways to improve the model would be to test the assumption of spatially independent physiological parameters, for fast growing tumors the boundaries between zones should be examined, and the use of a heterogeneous distribution of drug molecules in the blood. [67]

Soltani and colleagues used previous models and assumed a spherical tumor. Some of their assumptions included drug particles flow with the interstitial fluid. This study demonstrated an increase in necrotic radius decreases the maximum pressure inside the tumor, also they demonstrated that if a tumor is completely necrotic the interstitial fluid pressure is zero. They also found that the transport of a drug into a smaller tumor, defined as being below critical tumor radius, is easier than larger tumors. They also demonstrated that there is a critical necrotic radius. Above the critical necrotic radius the effective pressure is such that it is easier for drugs to reach the center of the tumor. [11]

The work of Howard and colleagues is focused on the treatment of non-Hodgkin's Lymphoma. The model used is trying to demonstrate usefulness for patient specific

dosimetry-based treatments. This planning requires an accurate assessment of the

radiation absorbed by the healthy tissue. The majority of these calculations are

predetermined by Monte Carlo algorithms and use a "reference man" for the anatomy. An

optimal situation would allow for 3D imaging of the patient to be used in the Monte

Carlo algorithm rather than the "reference man." They have created a unit density sphere

model incorporated in previously established models. This ideal situation would create an

extremely calculation heavy treatment system, therefore becoming less clinically

available. The conclusions of this study show the sphere model is more applicable due to

the lower computational needs, but can be less accurate and therefore not useful in all

applications. [66]

The work of Chapman and colleagues focuses on modeling the fluid flow through

the capillary of a tumor. Their model describes fluid flow through solid tumors, and uses

a number of different capillary lengths. Some of the assumptions they used in their model

include using blood as a Newtonian fluid, where the model could be improved by using

blood as a shear-thinning fluid. Other assumptions that they used and could be changed to

improve the model include the viscosity of blood. They claim that as the plasma leaks out

of the capillary it would alter the hematocrit and therefore change the viscosity; this

change would create a need for additional feedback in their model. They also suggest that

their model could be improved if further work included a pressure-dependent capillary

radius. [64]

3.1   Monte Carlo

Mathematical modeling of tumor and tumor vasculature have been proposed and implemented to address different goals. With their model established in 1988 [68], Jain and colleagues studied the effect of antiangiogenic agents on the tumor IFP. [63] The IFP of various tumors was calculated based on the transport properties of the capillary wall and interstitium and a decrease in the IFP of the tumors after antiangiogenic treatment was reported. The decrease in IFP occurs because the capillary walls are less permeable than before the treatment. From the point of view of the nanoparticle-based treatment, this imposes a trade-off between a more efficient delivery due to a larger pressure gradient from the capillary to the tumor, but through a less permeable wall. The fluid flow through the leaky vasculature of the tumor was also studied using modeling. [64] In that model, the flow along the capillaries, across the capillary walls, and through the interstitium were described by Poiseuille's [25], Starling's [69], and Darcy's laws [70], respectively. However, in their study the authors treated blood as a Newtonian fluid.

Frieboes and colleagues used a mathematical model to understand some of the variables that may help to explain tumor growth and invasion. [65] Soltani and Chen [11] developed a numerical model to study the fluid flow in the tumor interstitium where the tumor tissue was assumed to be spherical and the fluid flow was governed by conservation of mass and momentum. They studied the fluid velocity and interstitial fluid pressure as a function of the tumor size. Chang and colleagues, developed a network model to study the delivery of colloidal drugs [9] where the tumor interstitium was represented by a 2-D square network while the movement of colloidal particles in the interstitium was simulated by the Brownian dynamic simulation method. Drug delivery

for different drug concentrations and different interstitial pressures was studied in that work.

Models to predict nanoparticle transport and uptake in tumor tissue have also been discussed in the literature. Goodman and colleagues [71] developed a mathematical model of nanoparticle transport in a non-uniform porous spheroid representing a tumor. Nanoparticle diffusion into spheroids and particle binding and dissociation at the cell surface was modeled. The effect of the number of binding sites and pore distributions in the spheroid on the nanoparticle transport and accumulation is studied. Nanoparticle accumulation was predicted to be non-uniform but correlated with the porosity of each region in the tumor model. Stylianopoulus and colleagues [72] developed a methodology to calculate the diffusion coefficients of macromolecules and nanoparticles in collagenous tissues resembling the interstitium. The tissues were modeled as three-dimensional, stochastic, fiber networks with varying degrees of alignment. The study predicted that the structure and orientation of collagen fibers in the extracellular space affects the isotropy of nanoparticle distribution, with more aligned fibers resulting in a more anisotropic distribution. Frieboes and colleagues [73] modeled the accumulation of nanoparticle in tumor vasculature at different tumor stages. Their model simulates the growth of cancer tissue and predicts the accumulation of nanoparticle in its vasculature for different sized nanoparticle. They predict that increasing the affinity of nanoparticles for vessels results in their accumulation at the tumor inlet leading to a poor delivery to the tumor core and outlet vessels; in contrast, reducing the vascular affinity produces a more uniform nanoparticle distribution but also reduces the overall nanoparticle delivery. Mishra and colleagues [74] on the other hand, study the tumor response to the

nanoparticles delivered. Their model describes the nanoparticle concentration in the tumor cell and the tumor cell movement. Their model predicted an exponential reduction of tumor size as a long-term response to the treatment for both 10 nm and 100 nm nanoparticle. The effect of nanoparticle's shape and size has also been addressed, [75] reports experimental evidence that size, shape, and surface properties all play a role in the nanoparticle accumulation in the vasculature with 1000 nm × 400 nm plateloids being predicted to provide a rapid and larger than ever reported before accumulation of nanoparticle in tumor. A mathematical model is then used to predict the probability of nanoparticle adhesion to the blood vessel that shows maximum adhesion for nanoparticle of 1000 nm in size in agreement with the experiment. The model also predicts that lateral drifting diminishes with size and it is smaller for spherical than for anisometric nanoparticle, as lateral drifting allows periodic interactions with the lateral wall, show smaller and more symmetric nanoparticles lower accumulation

The objective of the computational model developed by the Derosa group is to track nanoparticles in the blood stream and into the tumor through the capillary wall and to predict nanoparticle delivery as a function of controllable parameters that can be adjusted to optimize the delivery. [28] Nanoparticle transport is obtained from the velocity of the blood flow over imposed with Brownian motion. The blood vessel in the model is designed as a cylindrical tube with a single pore of a size in the range of the tumor capillary wall pores. This model is able to predict the dependence of the nanoparticle's delivery to the tumor tissue on blood pressure, interstitial pressure, size, and concentration of nanoparticles in the blood stream, and pore size. The model incorporates the parameters that characterize tumors and distinguish them from normal

tissue (such as high IFP and larger pore size), and simulates nanoparticle flow through the capillary wall as an extravasation event. Since drug and medical device development relies on design specifications that meet end-user needs and integrate a process for evaluation of performance metrics, the model presented here seeks to serve as a tool to predict the effect of relevant parameters on the uptake of medical nanoparticles, and thus provide parameters that can be used for future designs.

A model to simulate nanoparticle delivery to leaky solid tumors is presented. The study indicates that nanoparticle delivery increases with pore size. Hyperthermia [76], or any other mechanism which increases the pore size in the tumor blood vessel wall, is predicted to increased drug delivery. Smaller particle size leads to the same effect of increasing delivery; however, deliver is found to be more sensitive to pore size than to particle size. The reason is that in addition to increasing the pore/nanoparticle size ratio, the velocity of the fluid entering the pore increases with pore size, thus increasing the drag force. This effect has been observed in the velocity profile near the pore. Increased concentration of the nanoparticles in the blood leads to a linear increase in the number of nanoparticles delivered, but the relative efficiency with which they are delivered is virtually independent of the concentration.

The model proposed by the Derosa group [28] and described below shows agreement with the experimental information available and produces results that satisfy the author's logic in those cases where no experimental evidence is available. Application to other cases leads to provocative predictions, such as the different dependence of delivery on nanoparticle size for different tumor IFPs. It was found that the sensitivity of nanoparticle delivery to particle size decreases when IFP decreases (increasing the

pressure gradient from the capillary to the tumor). For the case studied here, for instance, there is a clear decrease in nanoparticle delivery with size until an IFP of about 18 mmHg; for lower IFP, the delivery is virtually insensitive to particle size. The same effect is observed as blood pressure increases, due to the same reason that the pressure gradient across the pore increases. All of these predictions would benefit from experimental verification and the authors expect this paper can motivate those experiments.

Although the collective effect of delivery through several pores is an aspect of this process that has not been considered in the work, this can be treated as the cumulative delivery through one pore at a time by appropriately adjusting the nanoparticle concentration. However, IFP changes as blood flows in the tumor will need to be taken into account, where large doses are to be simulated, any large accumulation of particles may change the IFP, and thus studies of the interstitium are called for. Predictions of total doses delivered to a tumor can be obtained by taking into consideration the decrease in nanoparticle concentration as they flow down the blood capillary.

Finally, it is important to mention that nanoparticle aggregation, if the aggregate are numerous enough and make it to the capillary, will certainly affect nanoparticle delivery, as shown in this work. Although particle size is a factor in delivery and aggregation will lead to much larger particles, nanoparticle aggregates formed within the body are quickly removed from the blood circulation by the liver and spleen. [77], [78] Aggregates would circulate for such a short period of time that their presence in the capillary bed could be neglected. Hence, nanoparticle aggregations are not considered in the model.

The Monte carol model developed by the Derosa group was designed to simulate

a blood capillary with one pore. The nanoparticles used were spherical in shape and

similar to the gold nanoshells discussed in CHAPTER 4 and CHAPTER 7 (given the

correct size). The NPs were acted upon by two forces, the flow of blood and Brownian

motion. The flow of blood was modeled using a pressure-driven flow model of a non-

Newtonian fluid in a cylindrical tube with "sticky" walls, which provided a parabolic

velocity profile with the maximum velocity at the center of the capillary. The Brownian

motion component was calculated using randomly assigned distances and angles for

movement. COMSOL was used to establish a zone where the pore had an effect on the

movement of the particles. This zone was established by creating two simulations in

COMSOL (with and without a pore) and noting the zone where the pore has an effect on

the fluid flow. The progression of a NP through the Monte Carlo modeled cylinder is

outlined in Figure 3-1. The O'Neal group contributed to the work of Podduturi and

colleagues by providing physiological relevance to the model parameters and

contributions of early data for the Derosa group to evaluate the functionality of the

model. [28]

NPs are randomly distributed across the cylinder

NPs are moved one at a time and identified by zone.
(no particle is selected for a second time until all
have been selected)

For NPs in zone 2 a time step is divided into multiple
smaller time steps

The NP is displaced due to Brownian motion

If the NP enters the pore or exits the bottom of the
cylinder, a new NP is delivered to the cylinder to keep
a constant concentration

Figure 3-1: Progression of a NP through the Monte Carlo model. Adapted from the work of Podduturi and colleagues. [28]

This work is unique in the portion of the nanoparticle delivery system it is modeling. The papers discussed and referenced in this section provided background information on the state of mathematical modeling of this system at the time of this work, and provided guidance for parameter values to contribute to the development of this model. The collaborative work between the Derosa and O'Neal groups, in conjunction with the data presented in CHAPTER 6: Use of Real-Time Pharmacokinetics to Predict Tumor Uptake of Gold Nanorods, resulted in a peer-reviewed publication titled "Simulation of Transport and Extravasation of Nanoparticles in Tumors Which Exhibit Enhanced Permeability and Retention Effect". [28]

3.2   Controls

Collaborative work investigated the use of a controller with the objective of output tracking. Meaning the controller was attempting to make the blood plasma

concentration of nanoparticles remain within a desired (assumed) "therapeutic window" for the longest time possible with a minimal effort (minimize number of injected particles). The control implementation chosen involved a linear quadratic regulator state tracking design. This work used the blood plasma concentration curves from 0 to create a "Master Mouse" for each group (A and B) to observe the behavior of the nanorods. The model then continues to use four different injection profiles: linear (constant injection rate), positive quadratic (increasing injection with time progress), negative quadratic (faster initial rate and slowing with time progress), and an exponential curve. All results demonstrated similar total control efforts, but the positive quadratic had the minimal effort. [79] This work with a controller will be significantly more interesting once a therapeutic window has been established, and we are able to use these control systems to target specific AUC values or maintenance in a therapeutic window for a specific time to achieve a desired result. These controls will be able to minimize system effort and create a constant AUC.

This work is in conjunction with the data presented in CHAPTER 6: Use of Real-Time Pharmacokinetics to Predict Tumor Uptake of Gold Nanorods, and resulted in a peer-reviewed conference proceedings titled "LQR Tracking of a Delay Differential Equation Model for the Study of Nanoparticle Dosing Strategies for Cancer Therapy". [79]

CHAPTER 4

ANIMAL PROTOCOL REVIEW USING
GOLD NANOSHELLS

4.1 Specifications and Introduction

The purpose of this set of experiments is to follow and review the established

protocols. These experiments will inform protocol updates implemented in CHAPTER 6:

Use of Real-Time Pharmacokinetics to Predict Tumor Uptake of Gold Nanorods. The

primary focus these protocol reviews is a retrospective analysis of the pulse photometer

data collection and processing, and the need to continue blood draw protocols

(APPENDIX A: Mouse Blood Draw Protocol). The result of these experiments include

recommendations for protocol updates to be used in CHAPTER 6: Use of Real-Time

Pharmacokinetics to Predict Tumor Uptake of Gold Nanorods. These experiments are

broken down into two separate trials: Hyperthermia and Long vs. Short.

4.1.1 Hyperthermia

As part of a continued effort to decrease injected volume, several parameters are

being studied to look for changes in circulation times. One of these parameters leads us to

study how hyperthermia will affect the circulation time of nanoparticles. Studies have

shown that hyperthermic conditions up to 42°C show increased extravasation. [29] The

previous study looked at hyperthermia over a specific period, where the study presented

here keeps the subject in elevated ambient environment conditions through the entire

accumulation phase. Some believe the effect of temperature difference on the circulation time is mainly based on peripheral vasodilatation in hot environments. Regardless of mechanism, previous studies have observed pore cutoff size increased to greater than 400 nm at 42°C. This increase in pore size allowed significant accumulation of particles up to 400 nm, when compared to normothermic conditions. [76] With more blood being sent through peripheral circulation to dissipate heat more nanorods may be able to avoid the macrophages of the RES mainly located in the liver and spleen. However, some studies have suggested that fever range hyperthermia could increase immune efficiency. [80] If this effect is observed with the RES, the nanorods could be cleared from the blood more rapidly. This study was designed to look for observable differences in circulation time between the hyperthermic subjects and control subjects.

4.1.2   Long vs. Short

A third study will look into the difference in tumor accumulation and circulation time depending on the time over which the injection of a standard amount of nanoparticles is given. For example, a standard amount of nanoparticles will be given over a period of less than thirty seconds for one group and another experimental group would receive their injections over a period of ten to fifteen minutes. This study will be conducted without tumors then repeated using tumors. The iterations of the experiment will provide data on circulation time and tumor accumulation.

4.2   Materials and Methods

All of the studies involve animal work conducted under protocol approved by the Louisiana Tech University Institutional Animal Care and Use Committee (IACUC). The

animals were handled in accordance with the 'Guide for the Care and Use of Laboratory Animals'.

4.2.1   Hyperthermia

Eight naive BALB/c female mice with intact thermoregulatory systems were used to study the effects of hyperthermia on circulation half-life of experimental gold nanoshells (NBI, Houston, TX).

The experimental group of mice was placed in a forty-two degree Celsius environment for a minimum of forty-five minutes prior to injection. The mice were anesthetized using isoflurane anesthesia (given at 1 liter per minute at 4% for induction and 2% for maintenance), and the nanoshells (a standard dose of 4.5 µL/g) were injected over 10 seconds via tail vein. Once any procedure on the experimental mice was completed, the mouse was put back in the forty-two degree Celsius environment.

The control mice were placed in a thirty-six degree Celsius environment for a minimum of forty-five minutes prior to injection. The mice were anesthetized using isoflurane anesthesia (given at 1 liter per minute at 4% for induction and 2% for maintenance), and the nanoshells (a standard dose of 4.5 µL/g) were injected over 10 seconds via tail vein. After injection, the mice were kept at room temperature (20-26°C) throughout the experiment.

4.2.2   Long vs. Short

Four naive BALB/c female mice with intact thermoregulatory systems were used to study the effects of injection rate on circulation half-life of experimental gold nanoshells (NBI, Houston, TX).

The experimental group of mice was placed in a thirty-six degree Celsius environment for a minimum of forty-five minutes prior to injection. The mice were anesthetized using isoflurane anesthesia (given at 1 liter per minute at 4% for induction and 2% for maintenance), and the nanoshells (a standard dose of 4.5 μL/g) were injected over 1 minute via tail vein. Once any procedure on the experimental mice was completed, the mouse was returned to housing during the accumulation phase.

The control group of mice were placed in a thirty-six degree Celsius environment for a minimum of forty-five minutes prior to injection. The mice were anesthetized using isoflurane anesthesia (given at 1 liter per minute at 4% for induction and 2% for maintenance), and the nanoshells (a standard dose of 4.5 μL/g) were injected over 10 minute via tail vein. Once any procedure was completed, the mouse was returned to animal housing, for the duration of the accumulation phase.

4.2.3   Intravenous Catheters and Cannulation

Intravenous cannulas were made using 2 French Polyurethane Catheter tubing (Access Technologies, Skokie, IL Cat. No BC-2P). On one end, used as the needle for vascular access, a 28-gauge needle was removed from an insulin syringe (Tyco/ Healthcare ½ mL 28G x ½" insulin syringe REF # 1188528012, VWR Cat. # 84009-742) and attached to the tubing. On the other end of the tubing a 27 gauge needle (Becton Dickinson 27G x ½" REF 305109, VWR Cat. # BD305109) was added for slip tip or luer lock access to the cannula. Injection solution was loaded in a 1mL insulin syringe (Becton Dickinson 1 mL syringe REF 329650, VWR Cat. # BD329654). Injection volume and rate were ensured using a syringe pump (New Era Pump Systems, Inc. Farmingdale, NY. Model # NE-1010).

4.2.4   Temperature Control

Temperature regulation of the mice prior to injection was achieved using a shaking incubator, with the shaker off (Labnet International, Inc. Edison, NJ. Model # 211DS). During injection and while the mice were under anesthesia the temperature was controlled using a heating pad (Physitemp Instruments, Inc. Clifton, NJ. Model # TCAT-2LV) and a space heater for ambient air temperature (Sunbeam Products, Boca Raton, FL. Model # SFH111).

4.2.5   Gold Nanoshells

PEG modified gold nanoshells were obtained from NBI. The absorption spectra of the nanorods was obtained using a UV/Vis spectrophotometer (Beckman Coulter DU 800 Brea, CA.). A 1% dilution of nanorods was made using 10% Triton X to obtain the absorbance at 600, 805, and 940 nm. These values are required as input values of the NanoTracker to ensure proper calculations.

4.2.6   Blood Plasma Concentration Observations

Blood plasma concentration was observed (under isoflurane anesthesia) at intervals of approximately 20 minutes post injection, 90 minutes post injection, end of the first half life, 1.33 half-lives, 1.66 half-lives, and at the end of the second half life. These times were based on an assumed six-hour half-life, and altered if an extremely long or short half-life was noted. If it was not possible to collect data at those exact times for any reason the data point was taken early or late to get as close to the correct time as possible.

4.2.6.1   *NanoTracker*

Blood plasma concentration was collected using the NanoTracker; data points were taken before and after the blood draw. The operator manually recorded the blood

plasma concentration values, and attempts were made to ensure data was of sound quality

(standard deviations less than 0.03, on the mean of an averaged 5 seconds of data).

4.2.6.2 *Blood Draw Protocol*

The blood plasma concentration was confirmed using an established ultraviolet–

visible spectroscopy (UV/Vis) protocol (APPENDIX A: Mouse Blood Draw Protocol).

The blood for the UV/Vis protocol was collected by snipping the end of the tail and

collecting five micro-liters of blood using a pipette coated in Ethylenediaminetetraacetic

acid (EDTA).

4.2.7 One-Compartment Pharmacokinetic Model

The data from each mouse was manually entered to a spreadsheet and plotted. The

data was assumed to fit a standard one-compartment pharmacokinetic model; an

exponential trend line was added and used to calculate relevant pharmacokinetic metrics.

4.3 Results

Table 4-1 displays the half-life for each mouse involved in the hyperthermia study

for data collected from both the NanoTracker (NT) and absorbance spectrometry

(UV/Vis). Both groups demonstrated similar half-lives; a t-test was used to demonstrate

strength of the similarity between the two groups. The number of mice in each group

suggests that a t-test is not fully applicable in this situation, but it is simply being used to

demonstrate the strength of the similarity between these two groups. The third column

(the second UV/Vis) excludes the data for mouse 1. This piece of data causes a 22% drop

in the average half-live value for hot mice. When this extreme outlier is removed the data

demonstrates no statistically significant difference between the experimental and control

groups. The data in the UV/Vis groups have a higher probability of error due to the

complicated protocol and the need for extreme accuracy in each step. This accuracy would have been difficult for a newly trained group to obtain. This inexperience means the NT data should be considered more accurate for this study. This data suggests that there is no difference in the circulation patterns of nanoparticles based on ambient temperature during circulation. This finding suggests that any future study demonstrating different pharmacokinetics during accumulation/circulation would be attributed to differences in uptake and retention in tumors rather than differences in immune response.

Table 4-2 displays the half-life for each mouse involved in the long vs. short study for data collected from both the NanoTracker (NT) and absorbance spectrometry (UV/Vis). Both groups demonstrated similar half-lives; a t-test was used to demonstrate strength of the similarity between the two groups. The number of mice in each group suggests that a t-test is not fully applicable in this situation, but it is simply being used to demonstrate the strength of the similarity between these two groups. These data suggest that there is no difference in the circulation patterns of nanoparticles based on length of injection. This finding suggests that any future study demonstrating different pharmacokinetics during accumulation would be attributed to differences in uptake and retention in tumors rather than differences in immune response.

4.3.1 Hyperthermia

The hyperthermia experiments demonstrated an average half-life of 150 and 160 minutes for cold and hot mice, respectively (shown in Table 4-1).

Table 4-1: Half-life (in minutes) for cold and hot mice calculated from NanoTracker and Blood Draw (UC/Vis) protocols.

		NT	UV/Vis
Cold	Mouse 1	170	115
	Mouse 2	98	128
	Mouse 3	180	135
	Mouse 4	150	128
	Average Cold	150	126.5
	STDEV	37	8.35
Hot	Mouse 1	81	9
	Mouse 2	99	33
	Mouse 3	201	115
	Mouse 4	258	113
	Average Hot	160	67.5
	STDEV	84	54.59

When the groups of mice were compared, the p-values from a T-Test were 0.83 and 0.08 for NanoTracker, and UV/Vis, respectively. These p-values suggest we are unable to reject the null hypothesis of the means being equal, for $\alpha=0.05$; there is not sufficient evidence to prove these groups are dissimilar. These sample sizes do not reflect a large enough population for parametric statistics to provide useful insights. Graphs of the blood plasma concentration (representing the concentration of compartment 1 in a one-compartment model) are shown for hot and cold mice (Figure 4-1 and Figure 4-2, respectively).
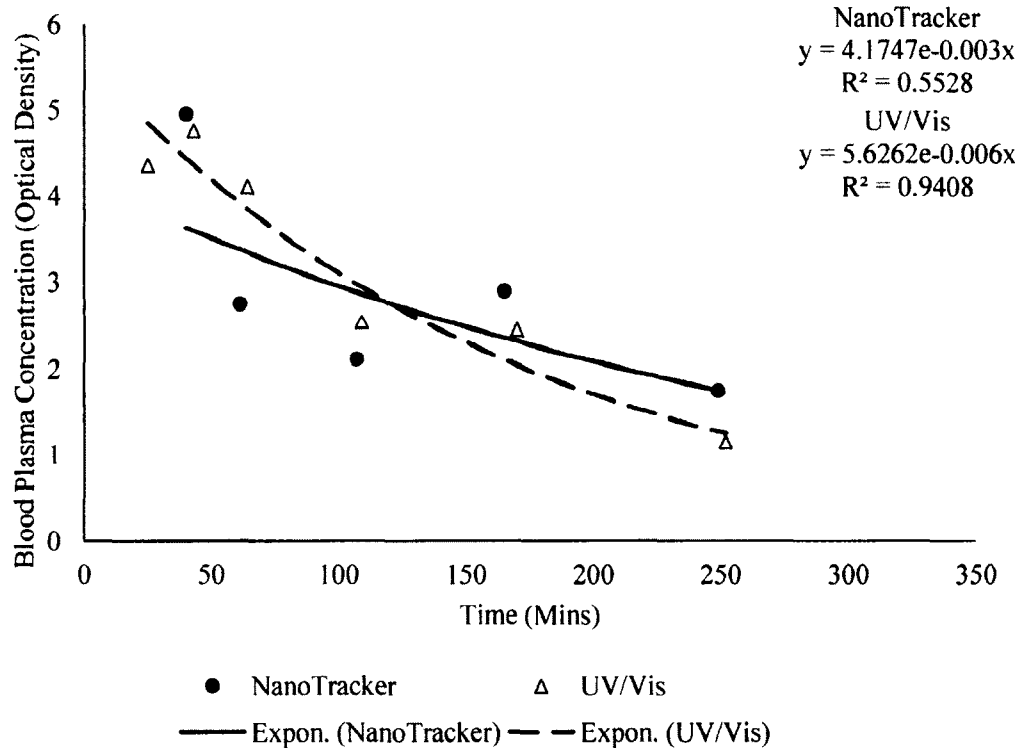
Figure 4-1: Blood Plasma Concentration vs. Time Hot Mouse 3. This chart is an example of the data charted for the one compartment exponential decay of a mouse kept in a hot environment with NanoTracker and blood draw data.
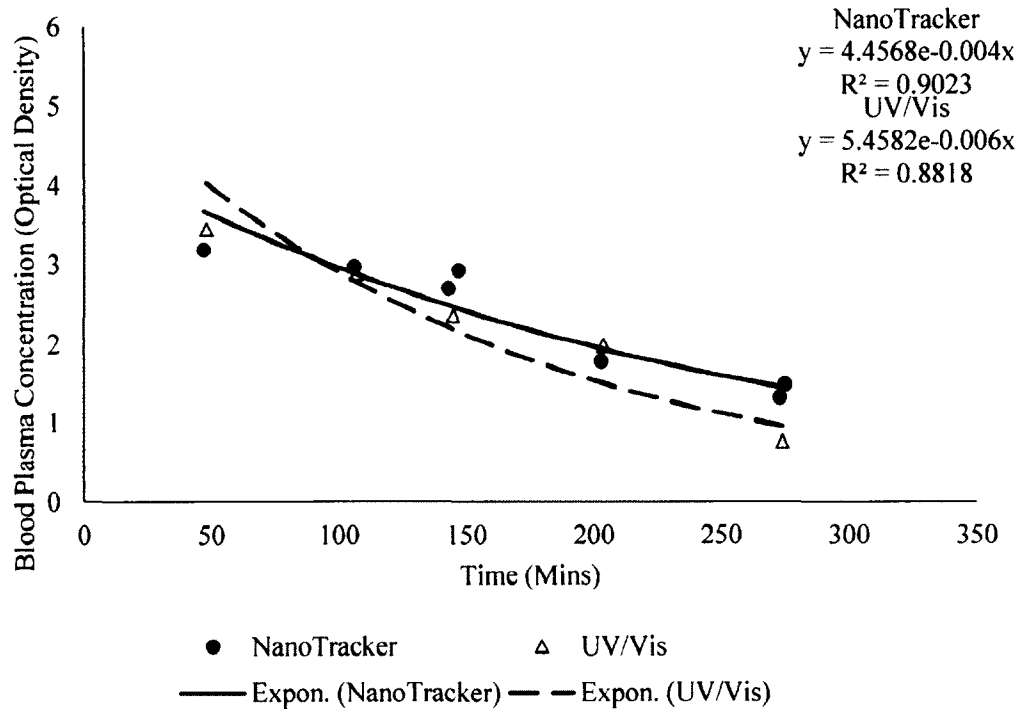
Figure 4-2: Blood Plasma Concentration vs. Time Cold Mouse 1. This chart is an example of the data charted for the one compartment exponential decay of a mouse kept at room temperature with NanoTracker and blood draw data.

4.3.2   Long vs. Short

The long vs short experiments did not demonstrated a large change in half-life in the long mice, but did in the short mice (shown in Table 4-2).

Table 4-2: Half-life (in minutes) for long and short mice calculated from NanoTracker and Blood Draw (UV/Vis) protocols.

		NT	UV/Vis
Long	Mouse 1	113	119
	Mouse 2	106	77
Short	Mouse 1	166	118
	Mouse 2	84	142

When the groups of mice were compared, the p-values from a T-Test were 0.74

and 0.32 for NanoTracker, and UV/Vis, respectively. These p-values suggest there is no

significant difference between the means of the long and short mice, for α=0.05. These

sample sizes do not reflect a large enough population for parametric statistics to provide

useful insights. Graphs of the blood plasma concentration (representing the concentration

of compartment 1 in a one compartment model) are shown for long and short mice

(Figure 4-3 and Figure 4-4, respectively).
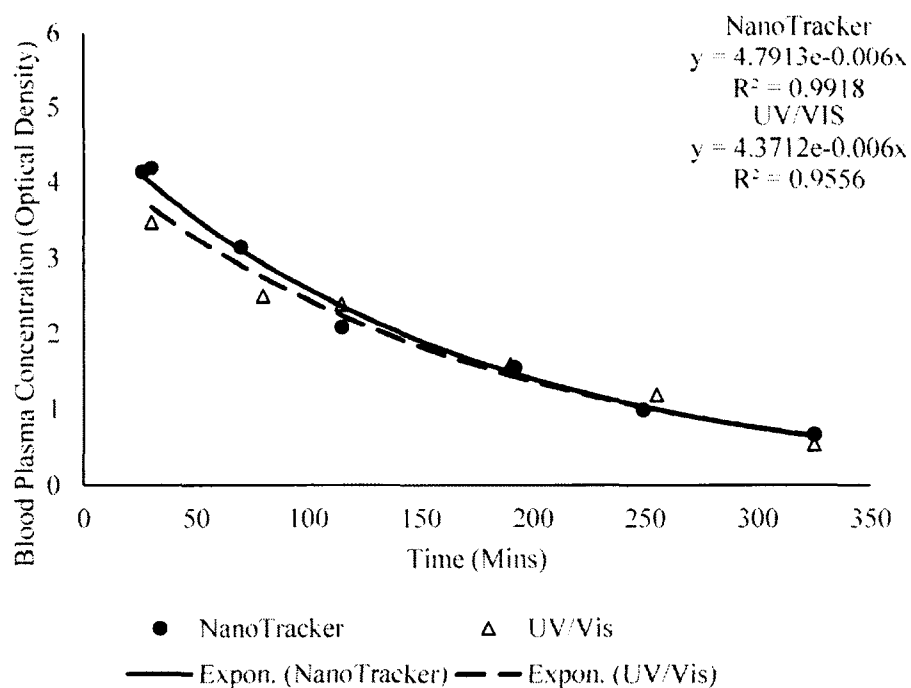
Figure 4-3: Blood Plasma Concentration vs. Time Long Mouse 1. This chart is an example of the data charted for the one compartment exponential decay of a long injection with NanoTracker and blood draw data.
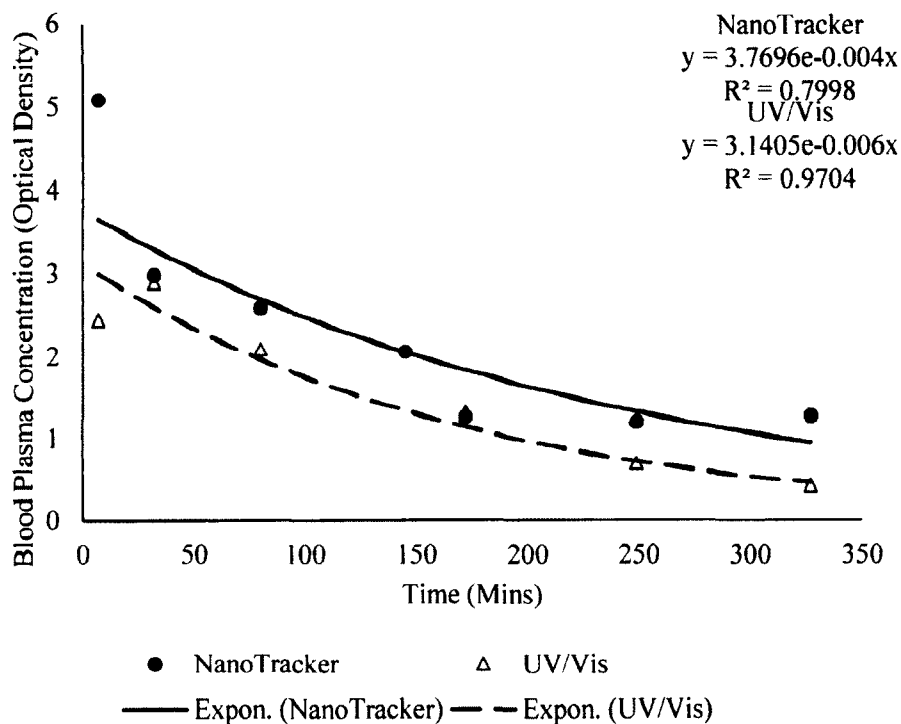
Figure 4-4: Blood Plasma Concentration vs. Time Short Mouse 1. This chart is an example of the data charted for the one compartment exponential decay of a short injection with NanoTracker and blood draw data.

4.4   Discussion and Review of Specifications

The data itself does not represent a large enough population to draw significant conclusions. A power analysis of the group suggests a necessary sample size (in each group) of 58 and 10 for Hyperthermia and Long vs. Short, respectively (α=5% β=80%). The large number of mice required to demonstrate a significant result for the hyperthermia experiment suggested continuing these protocols for a significant result would require too many animals and was thus was unrealistic. The continuation of these protocols to a significant result would also not fulfill the primary goal of this study, a

retrospective review of protocols. The small number of completed mice was able to provide necessary researcher experience to complete a primary stage retrospective protocol review.

The primary goal of these experiments was a retrospective protocol review. The most obvious lesson learned is regarding collecting and saving data, given the need to ensure all data meets standards. It is extremely difficult to observe the standard deviations of the two channels and record the piece of data in the five seconds while the number flashes across the screen. It is impossible to calculate the heart rate and ensure that all three heart rates are within 20% of the mean for each second, and the AC signal amplitude is between three and 100 mV each second. In addition, it was determined the data signal deteriorated with time. This problem resulted in two recommendations: ensure the mouse is kept warm during the time of data collection (to encourage adequate peripheral blood flow), and discontinuing the practice of collecting NanoTracker data under anesthesia. The final major protocol change is related to the confirmation of each point using blood draw protocols. The use of drawing blood from the animal comes into question due to the sampling without replacement. This sampling will result in a large change of blood volume of a mouse. This change in volume has caused other researchers to not observe blood plasma concentration during the accumulation phase of a tumored experiment. With the primary goal of future studies to involve the pharmacokinetic modeling of the accumulation phase, it was necessary to eliminate the blood draws.

A review of specifications is presented in Table 4-3, and the data from this set of experiments was presented at the "Southern Biomedical Engineering Conference" in

Arlington, Texas on April 30, 2011. The abstract from this presentation was published in

the associated conference proceedings. [81]

Table 4-3: Summary of observed protocol problems and solutions.

Observed Problem	Solution
Inability to meet heart rate and AC magnitude data requirements, and difficulty observing standard deviation	Save data and create rapid review algorithm.
Non-uniform creation of graphs and large amount of anticipated data from future saved files	Create MATLAB code to rapidly process "good" data and create uniform graphs.
Data quality deterioration.	• Discontinue use of anesthesia during data collection • Use space heaters to keep mouse warm
Impractical for use of blood draws related to tumored experiments, in addition they create a large human "bandwidth" problem for processing.	Discontinue blood draw protocol.
Staining on tail post Au nanoshell injection	Slow injection rate to reduce risk of staining on tail.

CHAPTER 5

DEVELOPMENT OF AN ENERGY DISPERSIVE
X-RAY FLUORESCENCE (EDXRF)
TECHNIQUE FOR ELEMENTAL
ANALYSIS OF GOLD
NANORODS

5.1   Introduction and Specifications

Throughout the work in the initial experiments of CHAPTER 6: Use of Real-

Time Pharmacokinetics to Predict Tumor Uptake of Gold Nanorods we found a need for

tumor uptake data faster than the traditionally used INAA. The old elemental analysis

methods required batches of tumors to be sent off for analysis taking 4 to 6 weeks. This

delay was found to be unreasonable for use in preclinical protocol and particle

development. In addition to the pre-clinical problems, the methods were impossible for

implementation in clinical settings where the data would be needed in under 12 hours for

use in clinical decisions. These needs led to these specifications:

- Tissue analysis completed in less than 12 hours

- Minimized skilled tasks to minimize potential error

Our lab group has chosen EDXRF as a system for elemental analysis of tissue

samples for several reasons, the main reason being the machine is readily available. This

quick turn around on samples makes our research go much smoother with a greater level

of confidence in our work. We are able to have the amount of gold in a tumor within 36

hours of the initial injection of nanorods into the mouse. This information is very important in guiding the next animal experiments.

This device uses x-ray excitation of a sample to characterize the elemental composition. X-rays are used to excite electrons from ground state to create an electron hole. This hole is filled by an electron in an outer shell. The energy difference from the electron moving from higher to lower energy is released as an x-ray. The released x-rays are then measured by an energy-dispersive spectrometer.

The specifications for the development of this elemental analysis protocol are:

- Complete sample analysis 12 hours after collection.

- Minimal sample preparation.

5.2 Materials and Methods

5.2.1 Animal Experiments

All experiments were conducted using BALB/c female mice inoculated with CT26.WT tumors on the subcutaneous flank. The accumulation experiment was performed on animals with a target tumor size of greater than 5 mm in length and width. All animals were handled and cared for in accordance with the Louisiana Tech University and Nanospectra Biosciences, Inc. (NBI, Houston, TX) Institutional Animal Care and Use Committees.

5.2.2 Temperature Control

Prior to injection and for three and a half hours after injection the animal was kept under specific temperature control (35-39°C), to facilitate intravenous cannulation and to normalize the extravasation of the gold nanorods. [37]

5.2.3   Dose Groups

For this experiment, two dose groups were used. Both of the groups were based on the multiples of standard dose administered by NBI. The first group received 4.5 µL/g subject weight of 100 optical density gold nanorods (Dose group A) and the second group received 9 µL/g of 100 optical density gold nanorods (Dose group B).

5.2.4   Anesthesia

For this experiment we used 2,2,2-Tribromoethanol (Sigma-Aldrich T48402) mixed with 2-Methyl-2-Butanol (Alfa Aesar A18304), more commonly referred to as Avertin, administered via intraperitoneal (IP) injection. The working solution of Avertin was administered at 30 µL of solution per gram body weight. Booster injections (0.5x) were delivered as necessary.

5.2.5   Injection

Nanorod injections were administered via intravenous cannulation of the tail vein, using a 28 GA needle. The injections were given at a rate of 9-18 µL/minute depending on dose volume and expected remaining time under anesthesia.

5.2.6   End of Experiment and Organ Collection

At the end of the experiment, defined as when the blood plasma concentration of circulating nanorods reached one optical density, [36] a 20 µL IP injection of a Ketamine/ mix was administered as heavy anesthesia. A dissection was started from the base of the abdominal cavity to sacrifice the animal by exsanguination via cardiac puncture using a 22 GA needle/syringe prefilled with 100 µL of heparin. After animal sacrifice, the following tissues were collected for further study: heart, lungs, liver, kidneys, spleen, and tumor.

5.2.7   EDXRF Sample Prep

A wet weight of the tissue was obtained at the time of extraction. A 20% w/w

KOH solution was added to the tissue based on the sample weight (3 μL/mg). The tissue

and base solution were placed in a shaker or rocker until the tissue liquefied,

approximately four to six hours. Aliquots of 35 μL (selected to cover our area of

detection: 15 mm x 12mm, containing approximately 0.04 g of tumor tissue) were placed

in EDXRF sample cups on a Prolene® thin film support (Chemplex Industries Inc., 4μm

thick, Cat. # 3017). The tissue solution was then dried in the sample cup for two hours in

a vacuum oven at 30° C under 15 in Hg vacuum to reduce the movement of sample. The

samples were analyzed in an ARL Quant'X (Thermo Scientific) EDXRF spectrometer (4-

50 KV x-ray generator, Be window, with 80°geometry between x-ray tube, sample, and

detector) using a thick Palladium filter (Mid-Zc range) for two minutes (50% dead time).

Three replicates were prepared from most tissue samples. Each sample cup was scanned

ten times which produced up to 30 spectra for each tumor. The spinner was turned on

during each scan to minimize error from the sample placement in the cup.

5.3   Results

The doped tumor samples were plotted and fit with a linear trend line (Eq. 5-1,

where PPM is the calculated sample concentration in parts per million and PI is peak

intensity in counts per second per milliamp) for use as a calibration curve (shown in

Figure 5-1).

$$PI = 0.0729 * PPM + 0.0174 \hspace{3cm} \text{Eq. 5-1}$$

This method has a detection limit (3σ) of 1.4 ppm and a sensitivity of 0.07 cps/mA/PPM.

The plot shows:

$$y = 0.073x + 0.0127$$
$$R^2 = 0.9838$$

with Peak Intensity of Gold (cps/ mA) on the y-axis and Gold Concentration (PPM) on the x-axis.
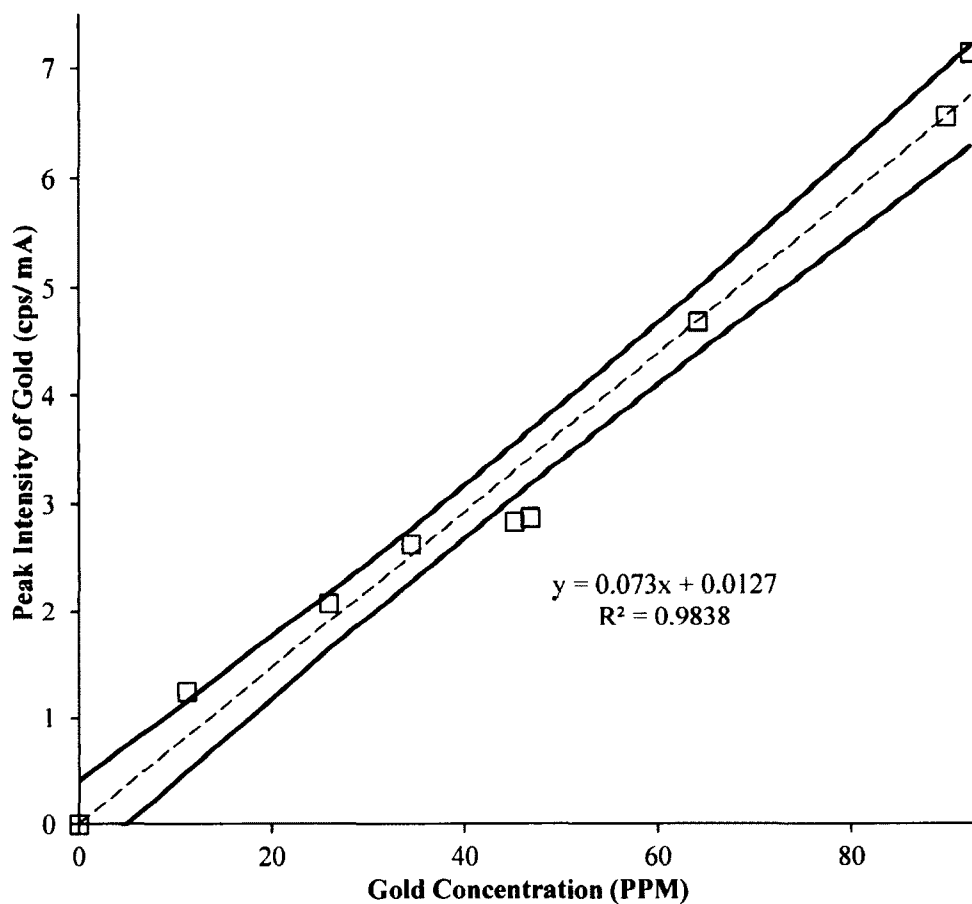
Figure 5-1: EDXRF Calibration. This graph demonstrates the raw calibration points (□), used calibration curve (dashed line), and a 95% confidence interval (solid line).

5.4   Discussion

The EDXRF protocol for gold in tissue was designed with the following aims: quick and easy sample preparation, thin samples, and quantitative results. A 20% KOH solution was chosen, after experimentation, to minimize the time for liquefaction of the tissue. Thin sample geometry was implemented because thick samples were impractical

given the amount of tissue available, and to avoid intermediate sample thickness. An

aliquot of 35 µL of tissue was selected to create a thin sample area entirely in the

detection geometry of the detector. Quantitative results were obtained using the same

tissue dilutions and same sample scan time; doped tissue samples for calibration were

able to provide a linear relationship between counts and tissue concentration.

The calibration curve was used to obtain the values of concentrations (in ppm) for

tumor samples (dose group A: n=8, mean = 10.7 PPM, STDEV = ±5.8 PPM, and dose

group B: n=9, mean = 25.3, STDEV = ±6.9 PPM). An analysis of the peak intensity

(CPS/mA) versus the gold concentration (PPM) using different tissue types showed an R^2

correlation of greater than or equal to 0.93, despite having different slopes (0.0733-

0.0856 cps/mA/PPM). We hypothesize that the small variations observed in reported

slopes were attributable to variations in tissue densities given that the regressions were

similar when multiple preparations of the same tissue type were analyzed. The calculated

concentration values for gold in tumors were similar to the work published by Huang and

colleagues, which used industry standard methods. [30] Commercial laboratories that

employ INAA or ICP-MS to analyze gold concentration report a detection limit in the

low PPB range. This EDXRF analysis method demonstrates a detection limit of 1.4 ppm

(3σ) and a sensitivity of 0.07126 cps/mA/PPM. This higher detection limit is acceptable

due to the clinical requirements of rapid results in the PPM range.

The majority of the problems encountered were due to the presence of other

elements that spectrally overlapped with one or more of the peaks of interest, as seen in

previous work. [82] The zinc $K\beta_1$ peak (9.570 Kev) overlaps the $L\alpha_1$ peak for gold (9.712

Kev). Other peaks were explored for potential use; a second peak, the $L\beta$ peak (11.204-

11.914 Kev), for gold overlapped the Kα₁ bromine peak (11.906 Kev). The bromine

peak was attributed to the use of avertin (2-2-2-tribromoethanol) as the anesthesia for this

experiment. The bromine peak was only observed in tissue samples where avertin was

used as the anesthesia. For this reason, the use of anesthesia may influence the elemental

analysis of tissues and should be considered among the criteria for selecting anesthesia in

experimental design.

5.5   Elimination of Zinc Peak

The running hypothesis of the lid of the machine being the source of the zinc was

further evaluated after the publication of the paper. The primary focus of this evaluation

was to find a cover for the EDXRF sample cups that is x-ray opaque. Multiple potential

covers were evaluated: a glass cup (Figure 5-2), a plastic cup (Figure 5-3), a golf ball

(Figure 5-4), an iron pipe cap (Figure 5-5), and a utility square (Figure 5-6). Due to the

presence of zinc peaks, the plastic cup and golf ball were eliminated from potential use. It

was decided the plastic cup was not x-ray opaque and the golf ball included zinc in the

core of the golf ball. Out of the three remaining items (which appeared to be x-ray

opaque), the utility square was chosen for the ease of use. It delivered a thin enough layer

placed on the cup to minimize risk of movement during machine cycling. The evaluation

of the spectrum was continued and began with an examination of the potential

contaminants of the Prolene film (the contaminants of the utility square were known from

Figure 5-6). Sample spectra were obtained of cups without and with a Prolene film using

a utility square cover (Figure 5-7 and Figure 5-8, respectively), and no new contaminants

were found. The next stage involved scanning tissue with no exposure to gold and tissue

doped with gold (Figure 5-9 and Figure 5-10, respectively). The Spectrum collected for

both of these samples demonstrated a zinc peak. This finding demonstrates the zinc is an

endogenous trace element. The search for an x-ray opaque cap was a wasted effort.
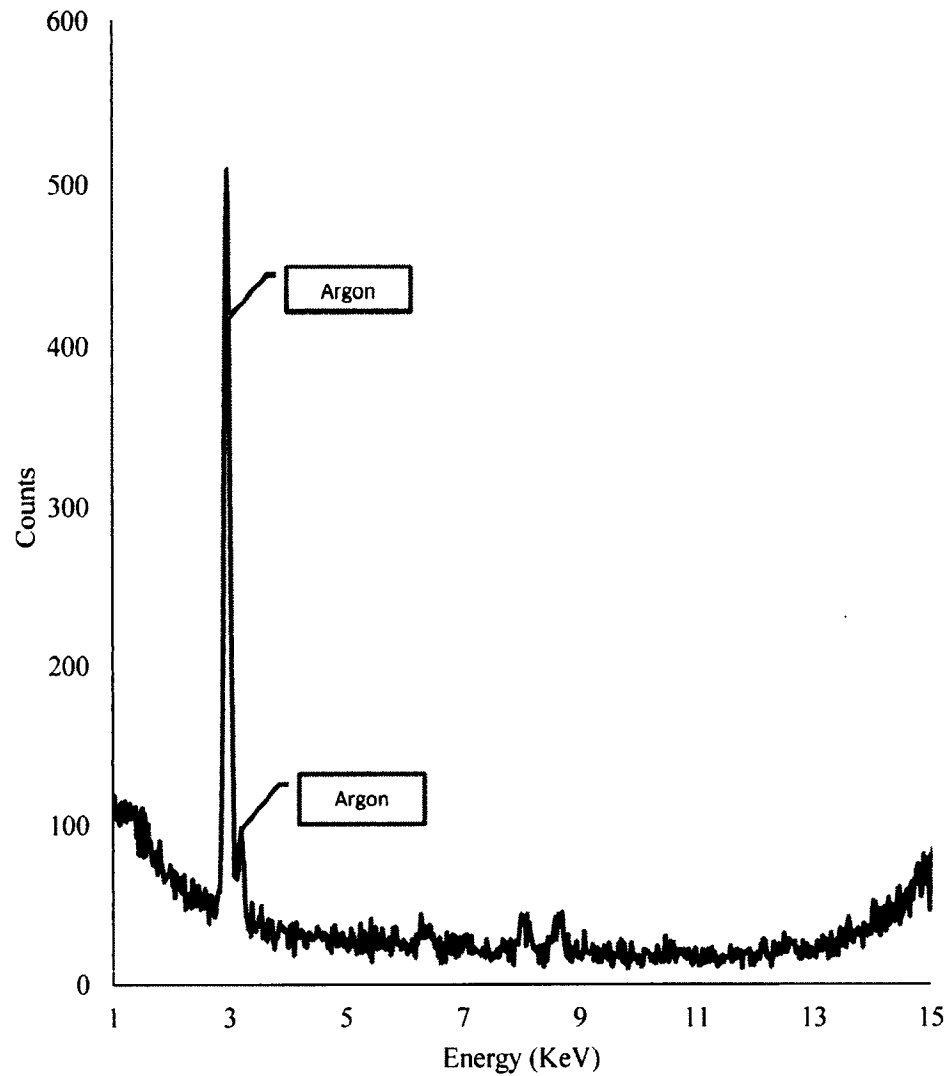
Figure 5-2: EDXRF Spectrum of a glass cup. Showing an argon peak.
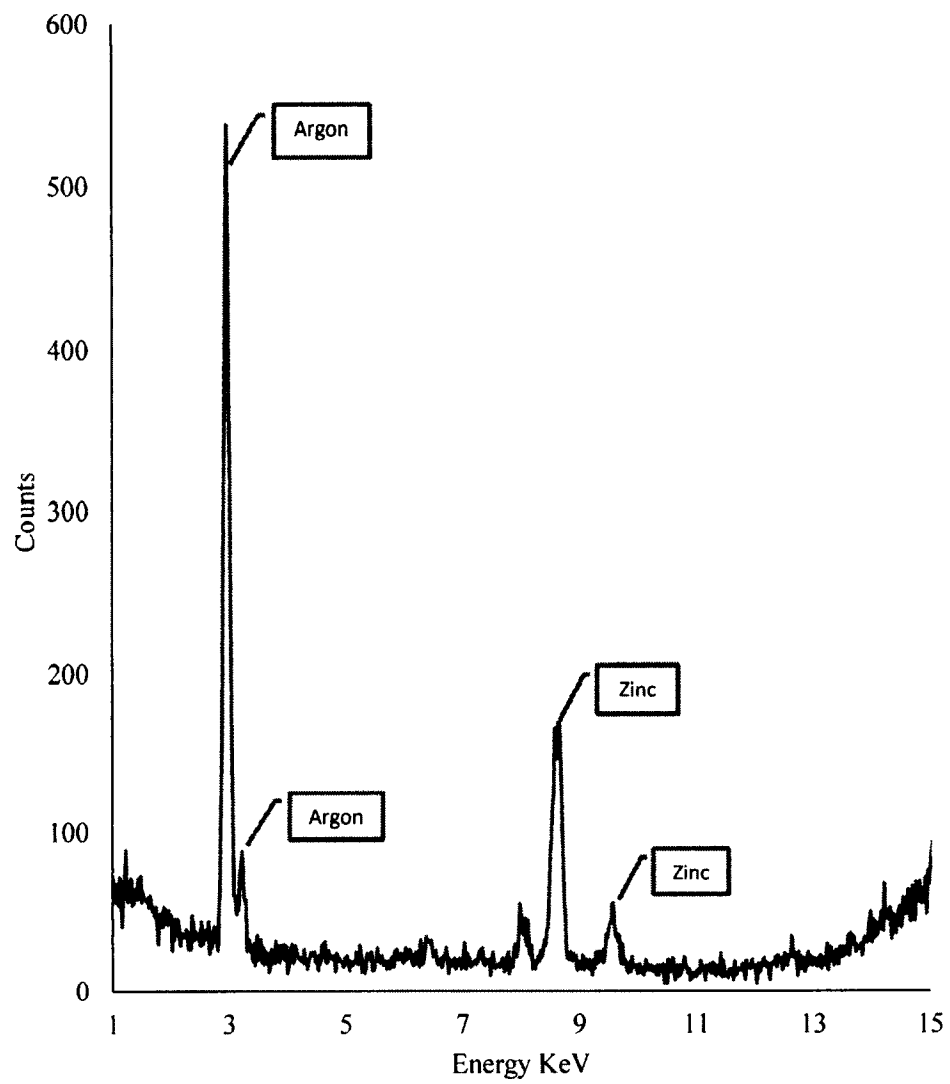
Figure 5-3: EDXRF Spectrum of a plastic cup. Showing argon and zinc peaks.
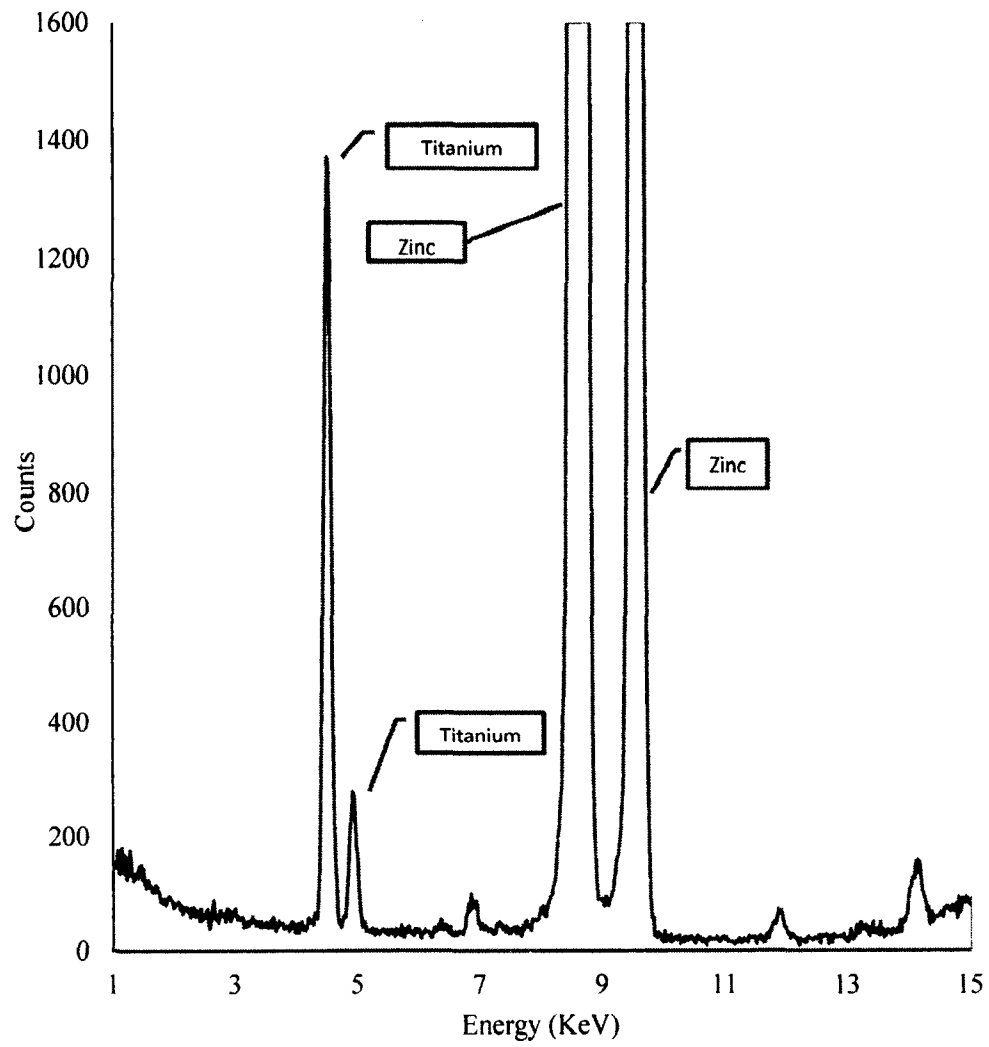
Figure 5-4: EDXRF spectrum of a golf ball. Showing titanium and zinc peaks.
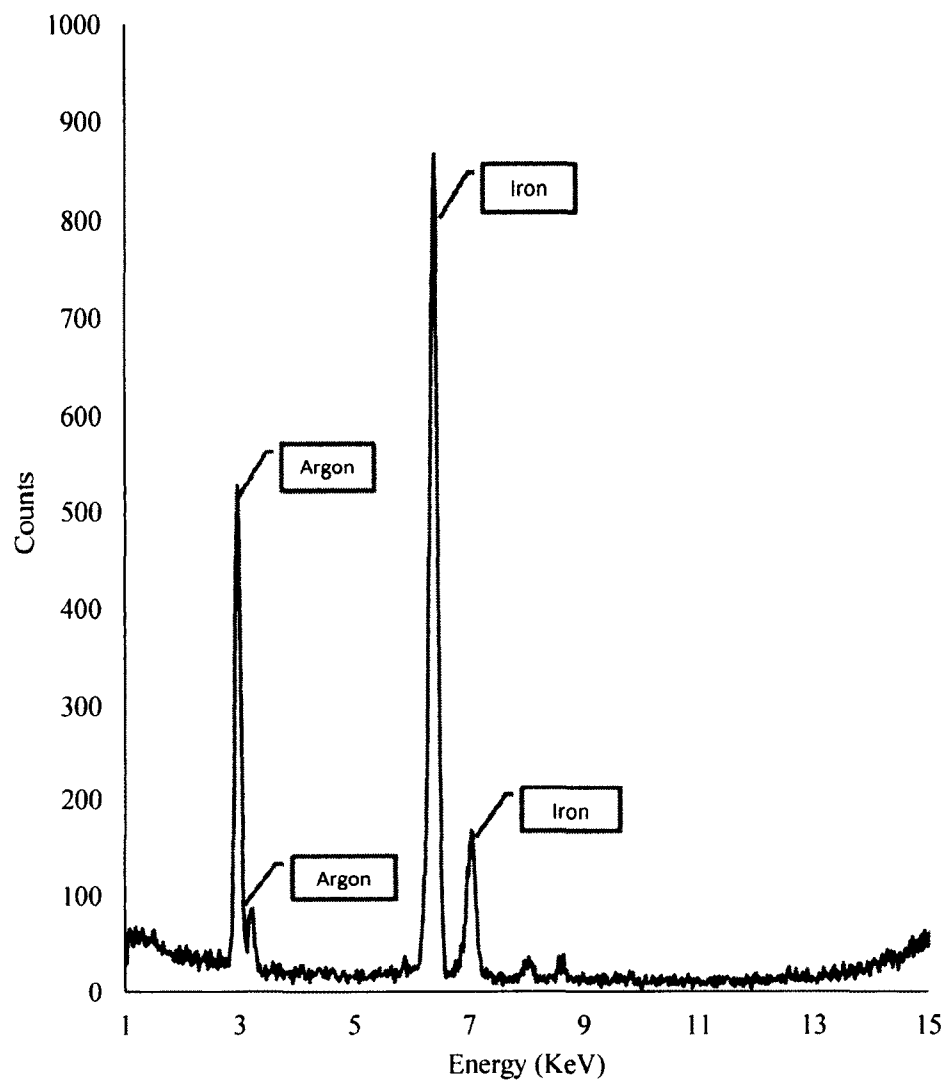
Figure 5-5: EDXRF spectrum of an iron pipe cap. Showing iron and argon peaks.
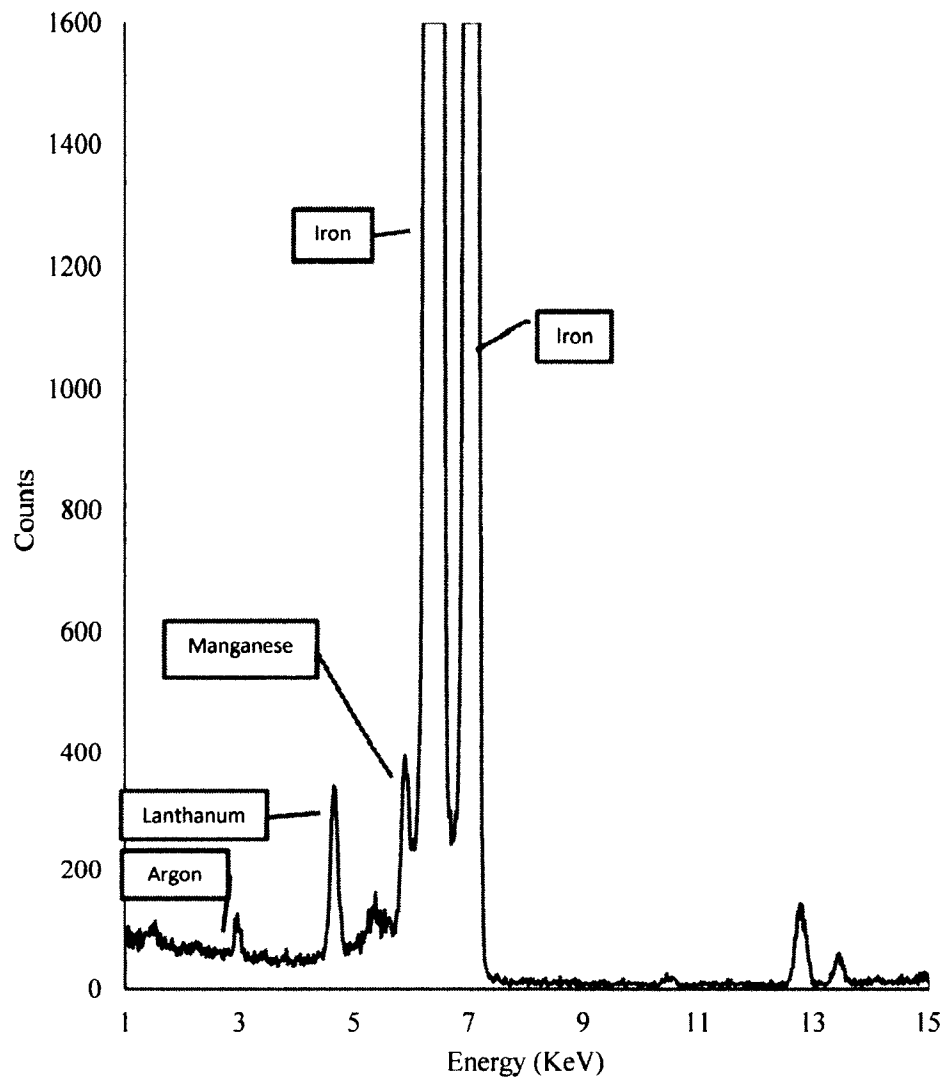
Figure 5-6: EDXRF spectrum of a utility square. Showing argon, lanthanum, manganese, and iron peaks.
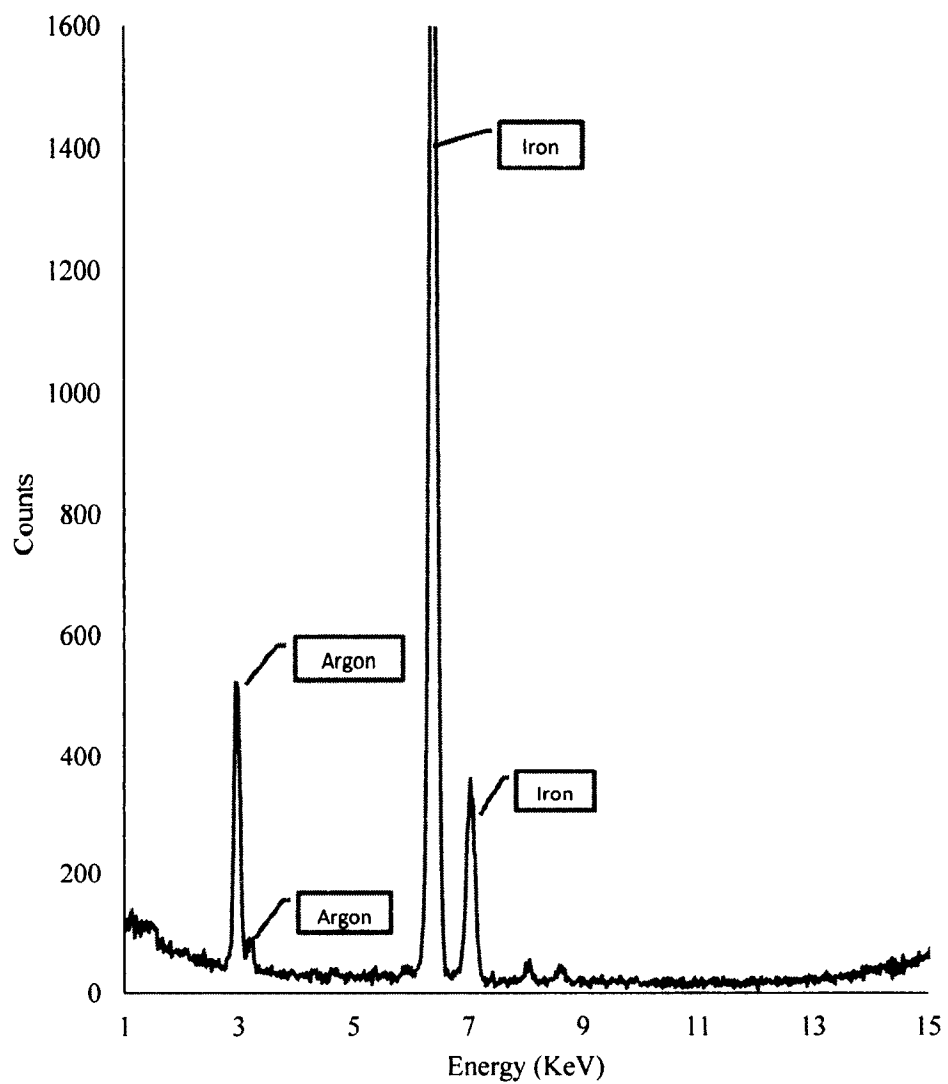
Figure 5-7: EDXRF spectrum of an empty EDXRF sample cup with no Prolene film capped with the utility square. Showing argon and iron peaks.
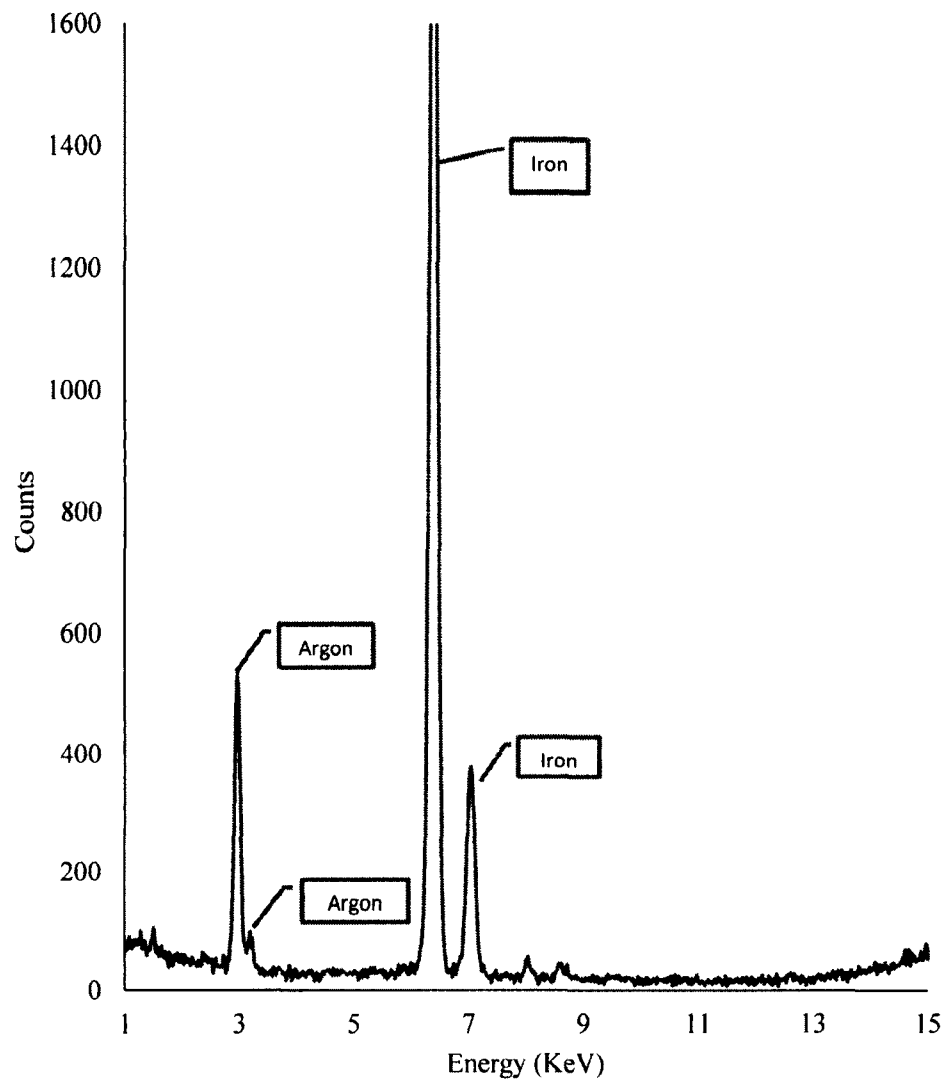
Figure 5-8: EDXRF spectrum of an empty EDXRF sample cup with a Prolene film capped with the utility square. Showing argon and iron peaks.
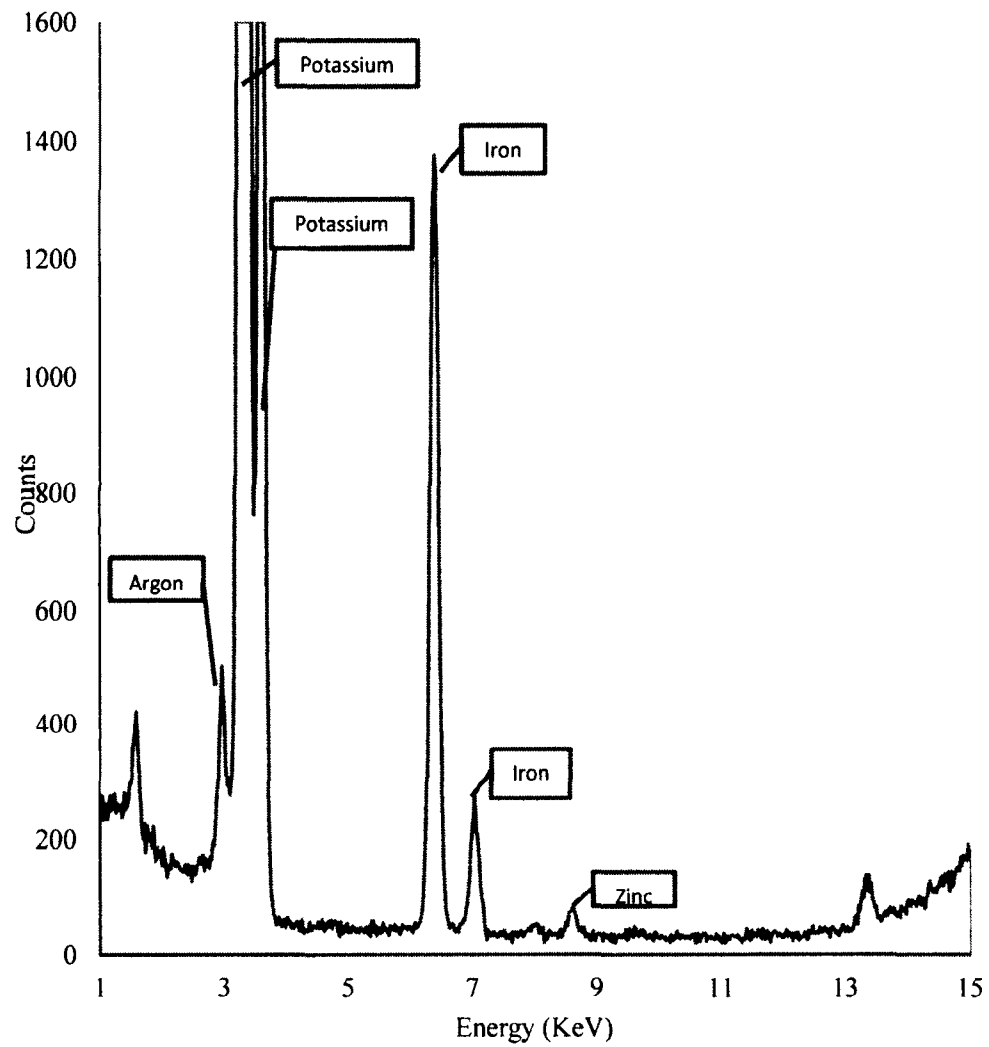
Figure 5-9: EDXRF spectrum of tumor with no gold exposure on a Prolene film capped with the utility square. Showing argon, potassium, iron, and zinc peaks.
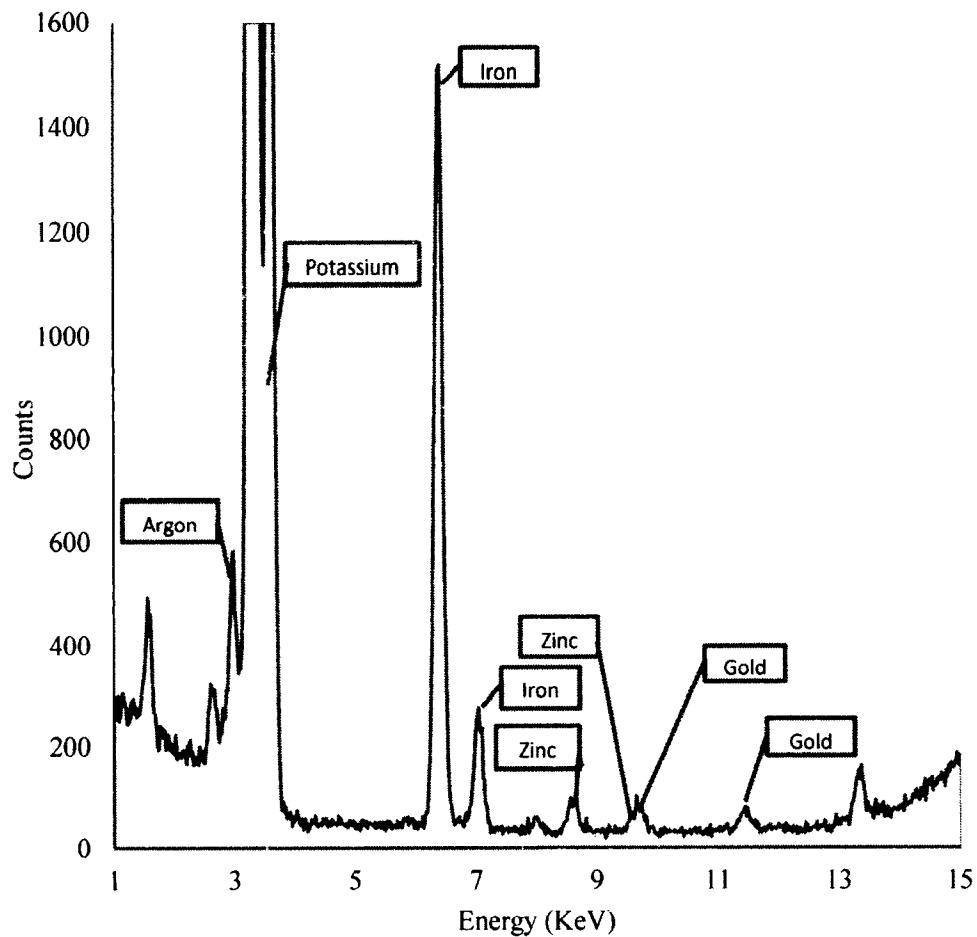
Figure 5-10: EDXRF spectrum of tumor doped to 33 PPM of gold on a Prolene film capped with the utility square. Showing argon, potassium, iron, zinc, and gold peaks.

5.6   Review of Specifications

Without this extended effort, the project met the original specifications

demonstrated in Table 5-1. The data from this project was initially presented at the 2012

BMES Annual Meeting on October 27, 2012 in a presentation titled "Real-Time

Measurement of the Bioavailability Curve of Experimental Gold Nanorods Towards

Dose Optimization," and is included in a publication titled "Feasibility of energy

dispersive x-ray fluorescence determination of gold in soft tissue for clinical

applications". [83]

Table 5-1: Summary of CHAPTER 5 specifications.

Specification	
Complete sample analysis 12 hours after collection.	As described in materials and methods, the time needed for all steps combined can provide analysis in 12 hours.
Minimal sample preparation.	The materials and methods section describes the sample preparation. The quick nature of the sample preparation (compared to other methods) was decided to be faster and simpler. In addition, the required skills are limited to reproducible pipetting.

CHAPTER 6

USE OF REAL-TIME PHARMACOKINETICS
TO PREDICT TUMOR UPTAKE
OF GOLD NANORODS

6.1   Introduction and Specifications

The work in this chapter involves protocol improvements informed by the work in

CHAPTER 4: Animal Protocol Review Using Gold Nanoshells, and demonstrates the

need for the Mathematical Modeling work in CHAPTER 3. In addition, the initial

experiments demonstrated the need for a rapid elemental analysis system developed in

CHAPTER 5.

Nanoparticle directed photothermal ablation of tumors relies heavily on the

accumulation of nanoparticles in target tissues. An appropriate accumulation of particles

is required for proper thermal confinement and ablation of the target tumor. Preclinical

studies of tumor accumulation are being conducted in an effort to more accurately predict

the accumulation of nanoparticles. This preclinical study in a murine model works to

relate the area under the blood plasma concentration curve to uptake and retention in the

tumor.

Many nanoparticles are currently approved by the FDA or under investigation by

groups seeking FDA approval, despite the fact that various pharmacokinetic parameters

that determine the accumulation and retention of these particles in the target organ are

mostly unknown. Some of these particles include Combidex for MRI contrast, and NanoTherm Aurimmune, and Auroshell used for cancer therapy. [21] The optimization of treatment variables, such as therapeutic dosage, circulation half-life, and clearance rates, is critical in maximizing the efficacy of a treatment modality. The majority of nanorods are removed from the blood by two pathways: opsonization and elimination by the RES, and accumulation in tumor tissue due to the EPR. [20], [37], [84], [85] These two being the major pathways of removal suggests a correlation between tumor uptake and retention and bioavaibility should exist. The purpose of the tumored studies is to correlate standard pharmacokinetic metrics to the uptake and retention of gold nanorods in tumors.

This set of experiments is based a hypothesis that pharmacokinetic metrics will be a more accurate predictor of tumor uptake alone and on the following specifications:

- Blood plasma concentrations will be collected in near real-time.

- Discrete blood plasma concentrations will be processed quickly (less than 5 minutes) after collection for inclusion in an actively changing one-compartment pharmacokinetic model.

- Elemental analysis of tumor tissue is completed in under 12 hours post experiment. Additional data processing time is limited to one hour after completion of instrumentation time.

6.2   Materials and Methods

All of the studies involve animal work conducted under protocol approved by the Louisiana Tech University and Nanospectra Biosciences, Inc. Institutional Animal Care

and Use Committee (IACUC). The animals were handled in accordance with the 'Guide

for the Care and Use of Laboratory Animals'.

All tumored studies involve naïve BALB/c females inoculated with 1.5 X 10^5 (50

ml injection volume) CT26.WT murine colon carcinoma tumor cells (ATCC) were

obtained from NBI. When animals arrived at Louisiana Tech University Center for

Biomedical Engineering and Rehabilitation sciences, the mice were kept in general

animal housing until the tumors were the proper experimental size, approximately 100

cubic centimeters.

6.2.1   Initial Experiments

This study involved the use of eight naïve, tumor inoculated BALB/c female

mice. The mice were divided into two groups: Group A (4.5 μL/g) and Group B (9 μL/g).

This experiment was designed to explore the differences in circulation half-life and other

pharmacokinetic parameters between the two dose groups.

6.2.1.1   *Temperature Control, Anesthesia, and Injection*

The mice were put in a thirty-six degree Celsius environment (Labnet

International, Inc. Edison, NJ. Model # 211DS) for a minimum of forty-five minutes

prior to injection. The mice were anesthetized using isoflurane anesthesia (given at one

liter per minute at four percent for induction and two percemt for maintenance), and the

nanorods were injected over up to ten minute via tail vein at a rate of up to 18 μl/min.

Once any procedure was completed, the mouse was returned to animal housing, between

procedures, for the duration of the accumulation phase.

6.2.1.2   *Blood Plasma Concentration Data Collection*

Blood plasma concentration data was taken at intervals of approximately 20 minutes post injection, 90 minutes post injection, end of the first half life, 1.33 half-lives, 1.66 half-lives, and at the end of the second half life. These times were based on an assumed six-hour half-life, and altered if an extremely long or short half-life was noted. If it was not possible to collect data at those exact times for any reason the data point was taken early or late to get as close to the correct time as possible. The concentration in the blood was calculated by using the NanoTracker, and confirmed using an established ultraviolet–visible spectroscopy (UV/Vis) protocol (APPENDIX A). The blood for the UV/Vis protocol was collected by snipping the end of the tail and collecting five micro-liters of blood using a pipette coated in EDTA, under Isoflurane anesthesia. NanoTracker points were taken before and after the blood draw.

6.2.1.3   *End of experiment*

The mouse was sacrificed when the blood plasma concentration reached an optical density of $1\pm10\%$. The mouse was sedated using a ketamine and zylazine mixture, and then sacrificed by exsanguination via cardiac puncture. Liver, kidneys, spleen, tumor, heart, and lungs were collected for EDXRF analysis.

6.2.1.4   *Data Analysis*

Data analyzed post experiment to create blood plasma concentration curves using Microsoft Excel. The Excel spreadsheet was designed to take the raw tabular spectra from each blood draw and calculate an adjusted optical density for each time point. From this spreadsheet, the data was plotted (optical density versus time).

6.2.2   Revised Experiments

This experiment involved seventeen tumor inoculated BALB/c female mice. The mice were divided into two dose groups (Group A and Group B) to investigate the differences in pharmacokinetic metrics, blood plasma concentration and tumor uptake based on injected dose.

6.2.2.1   *Temperature Control*

The mouse was placed in an environment with an ambient temperature of thirty-five degrees Celsius for two and a half hours using a shaking incubator, with the shaker off (Labnet International, Inc. Edison, NJ. Model # 211DS). For at least one hour prior to the injection, the ambient temperature was increased to thirty-nine degrees Celsius.

During injection and while the mice were under anesthesia the temperature was controlled using a heating pad (Physitemp Instruments, Inc. Clifton, NJ. Model # TCAT-2LV) and/or a space heater for ambient air temperature (Sunbeam Products, Boca Raton, FL. Model # SFH111)

After the injection, the mouse was returned to the incubator kept in a thirty-nine degree Celsius environment for the first three and a half hours of the accumulation phase. After the first three and a half hours, the mouse was returned to a room temperature environment for the remainder of the experiment.

6.2.2.2   *Anesthesia and Injection*

Intravenous cannulation was established after the mouse was under anesthesia. Avertin anesthesia (APPENDIX C) was administered by intraperitoneal injection at the dosage of 25 micro-liters per gram of body weight, while the air flow was maintained

steady at a rate of one L/min with the help of an Oxygen concentrator (Invacare Model: IRC5LX02, Elyria, OH) during the experiment.

The nanorod injection was done by cannulating one of the lateral tail veins. Once an intravenous cannula has been established and flushed with saline the NanoTracker was attached to the tail. The nanorods were injected at a rate of up to 18 micro-liters per minute using a syringe pump (New Era Pump Systems Inc., Model#NE-1010). The~100 OD nanorods were intravenously injected at the dosage of 4.5 μL/gm (Group A) or nine μL/gm (Group B) body weight at the rate of up to18 μl/min. The NanoTracker was used to monitor the condition of the mouse while under anesthesia.

6.2.2.3   *NanoTracker Data Collection*

The NanoTracker was used to read the blood plasma concentration of nanorods. The NanoTracker was attached to the tail of the mouse in a warm environment, with the help of a Physitemp TCAT-2LV controller pad set to 38°C and carefully monitored space heaters.

Once temperature stabilization was achieved, the probe was placed on the awake animal's tail and the NanoTracker was allowed to collect data. Five-second averages of the values of R were computed to assess signal stability.

Data collection was designed around an assumed six-hour circulation half-life of the nanorods, and with approximately five data points in the first half-life, two in the second and one in the third half-life. Data should be collected were close to the following time points as possible: 5, 45, 120, 240, 360, 450, 720, and 1080 minutes.

6.2.2.4   *End of Experiment*

The mouse was sacrificed when the blood plasma concentration reached an

optical density of one plus or minus ten percent. The mouse was sedated using a ketamine

and zylazine mixture, and then sacrificed by exsanguination via cardiac puncture. Liver,

kidneys, spleen, tumor, heart, and lungs were collected for EDXRF analysis.

6.2.2.5   *Data Analysis*

The collected data was be sorted by MATLAB code. A code was specifically written

to extract the data points that meet all the criteria for data standards. Anticipating

potential transient problems such as motion artifact or low perfusion, the signal was

deemed acceptable only if the following criteria were met:

- AC magnitude was in the range of 10-100 mV peak-to-peak

- the standard deviation of R was less than 0.03

- The heart rate measured on all three channels (660, 805 and 940 nm) were within

  ten percent of each other.

The data extracted from the raw experimental data and the average optical density

value was used to produce a blood plasma concentration curve (using a single decay

exponential model). This curve was used to calculate the area under the curve (AUC),

which was used as a pharmacokinetic parameter in the experiment. In addition, the peak

value and the half-life of the clearance curve were calculated.

6.2.2.6   *EDXRF Tumor Sample Preparation*

Using the wet weight of the tumor, obtained the day of extraction, 20% (m/m)

KOH was added at the rate of three μL KOH/mg of tumor. The tissue was left at room

temperature, in a low speed shaker until all tissue dissolved in the solution. From each

tumor sample, 30 μL (of tissue + KOH solution) was pipetted in up to three unique

EDXRF cups, as many as the mass of tumor tissue will allow. The solution was then

dried down in a vacuum oven at 30° C under 15 in Hg vacuum until tissue sample is

completely dry, this normally takes up to four hours. The dried samples were run in the

EDXRF machine (Quant'X, Thermo Electron Corporation) and run each sample with ten

replicates.

The machine calculated a ppm (parts per million) value for the concentration of

gold in the tumor.

6.2.2.7 _EDXRF Tumor Sample Data Analysis_

The ppm calculations were manually verified by using the calibration set in the

machine. The spectra from the calibration set (of known concentration values) were

extracted and the area under the curve of the gold L-α1 peak (9.94 to 9.30 KeV) was

extracted. From these values, the peak intensities were calculated and a calibration curve

was established. The calibration curve compared the peak intensity values (cps/mA)

against known concentration (ppm) values.

6.3   Results

6.3.1   Initial Experiments

The initial experiments demonstrated an average half-life of 276 and 462 minutes

for group A and B, respectively. Table 6-1 gives the calculated half-life, average, and

standard deviation for each group.

Table 6-1: Half lives for all mice in study (n=8) by dose group with averages.

	Group A	Group B
Mouse 1	323	452
Mouse 2	251	547
Mouse 3	287	389
Mouse 4	243	460
Average	276	462
STDEV	37	65

The results of this study demonstrate a significant difference between the half-lives of Dose Group A (n=4, mean=276.16 min) and Dose Group B (n=4, mean=461.92 min) (T-Test: p-value=0.0025, α=0.05).

6.3.2   Revised Experiments

The results of the rapid elemental analysis are displayed on a chart with the EDXRF calibration data (Figure 6-1). The tumor concentration ranged from 6.84-41.49 PPM. Figure 6-2 through Figure 6-9 show scatter plots of tumor accumulation plotted versus pharmacokinetic metrics. Of these, the highest R^2 correlations came from Injected dose (Figure 6-5, R^2=0.458) and Area under the Blood Plasma Concentration Curve (Figure 6-2, R^2=0.4503). Table 6-2 lists the computed half-lives for all mice in the study, and shows the large increase in average half-life from 271 minutes (group A) to 408 minutes(group B). The p-values from Table 6-3 demonstrate tumor weight is the only parameter where we are unable to reject the null hypothesis (the means of the dose groups are equal) (α=0.05).
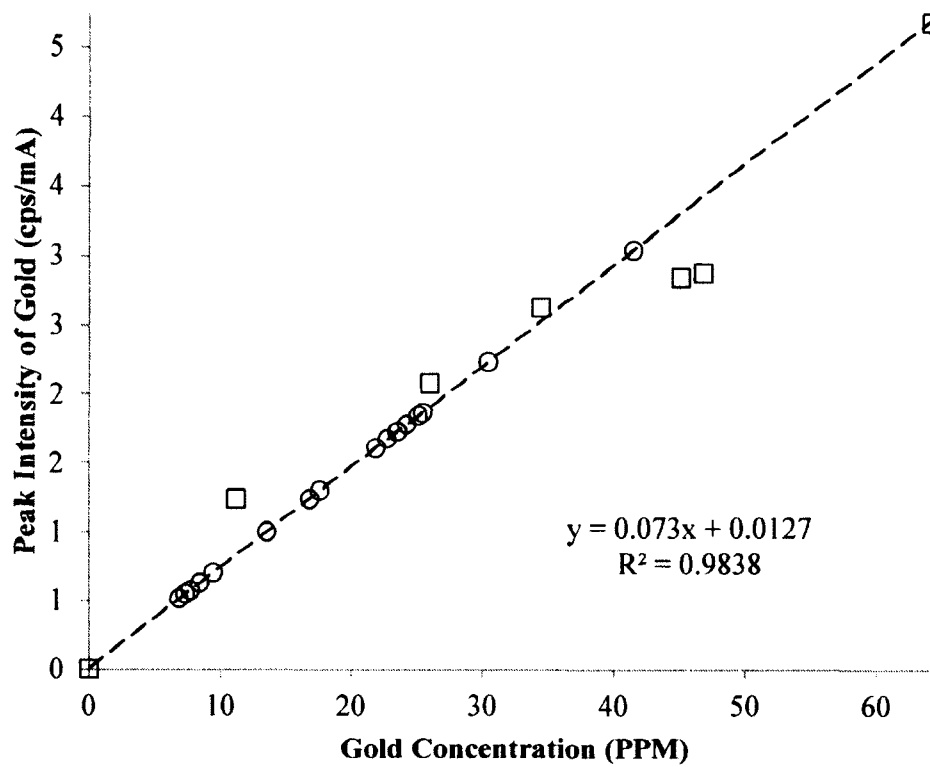
Figure 6-1: This graph demonstrates the raw calibration points (□), calibration curve (dashed line), and individual tumors (o).
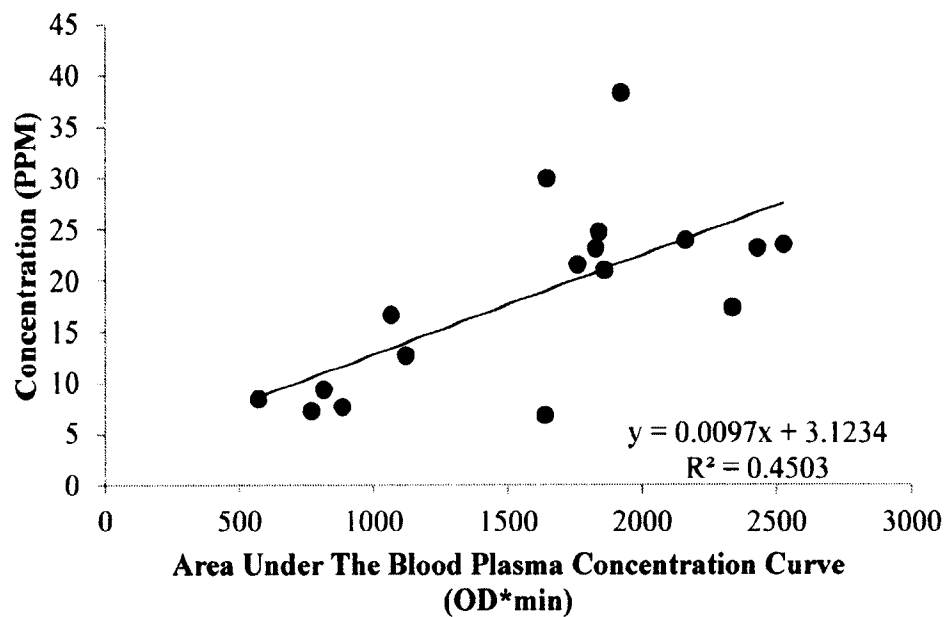
Figure 6-2: Tumor concentration versus area under the curve. R^2=0.4503.
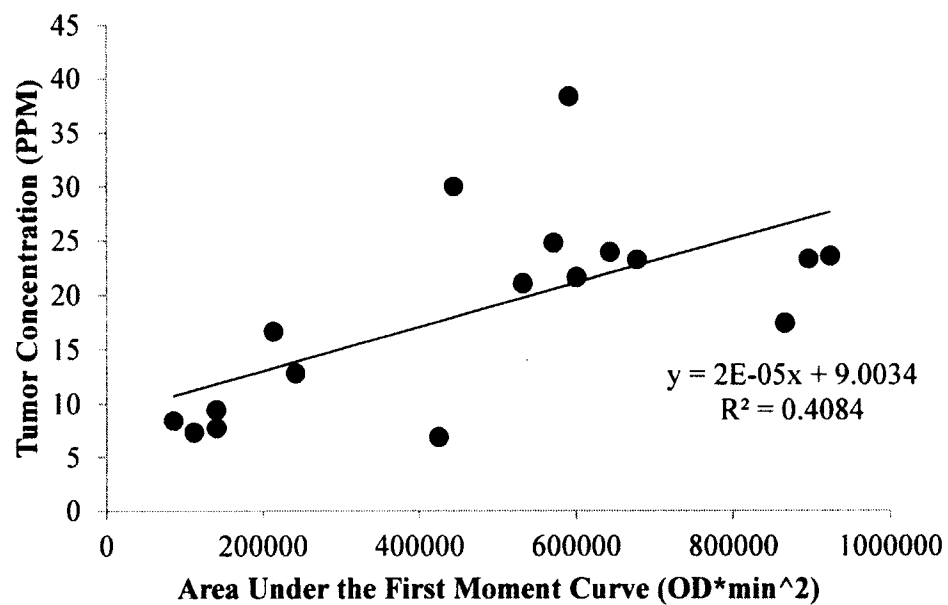
Figure 6-3: Tumor concentration versus area under the first moment curve. R^2=0.4084.
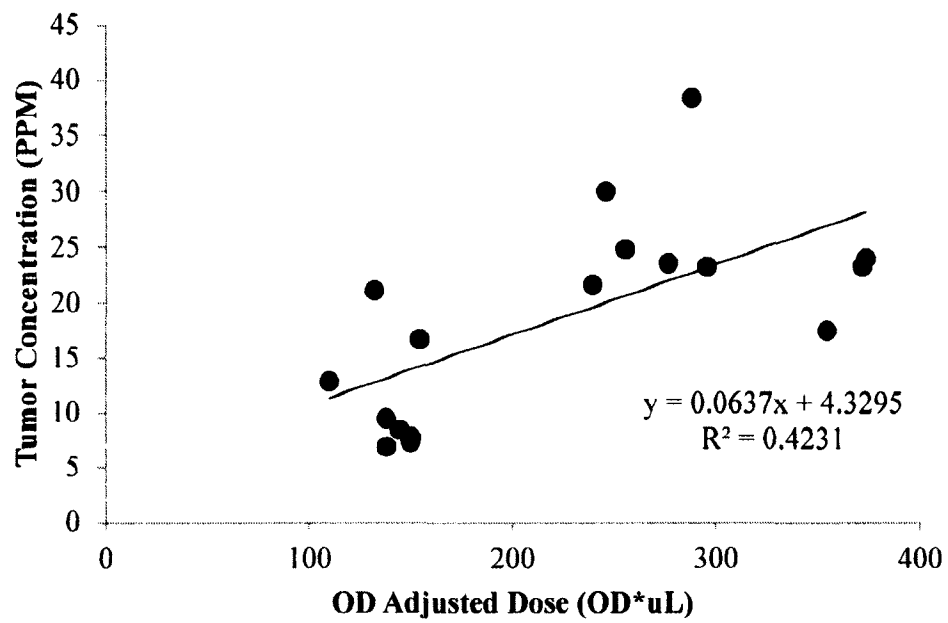
Figure 6-4: Tumor concentration versus OD adjusted dose. R^2=0.4231.
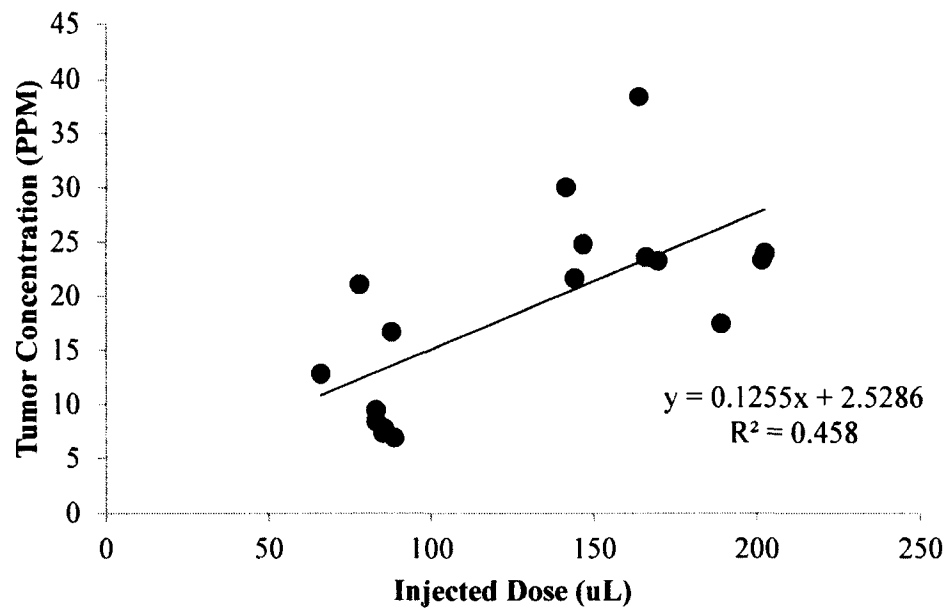
Figure 6-5: Tumor concentration versus injected dose. R^2=0.458.
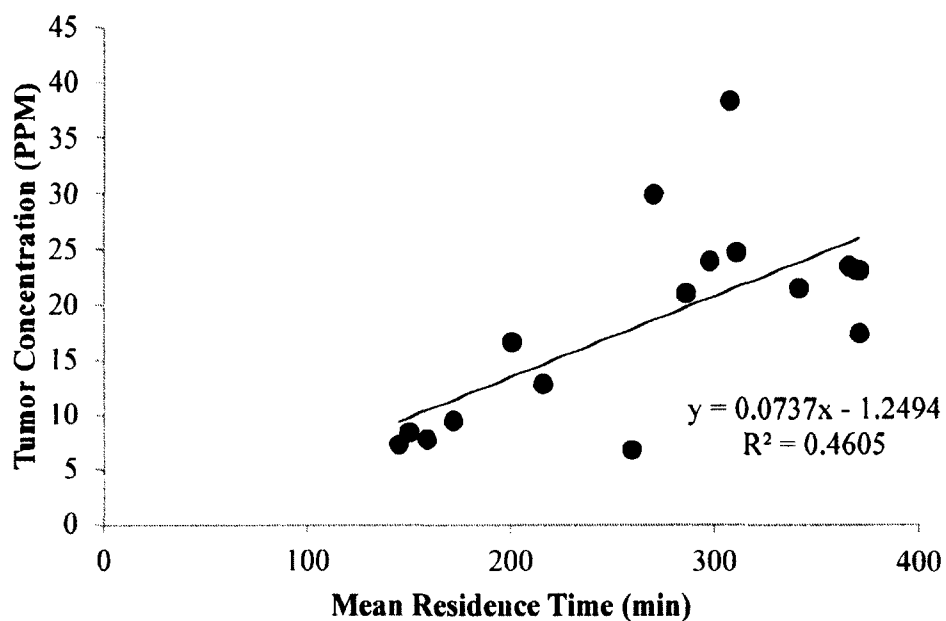
Figure 6-6: Tumor concentration versus mean residence time. R^2=0.4605.
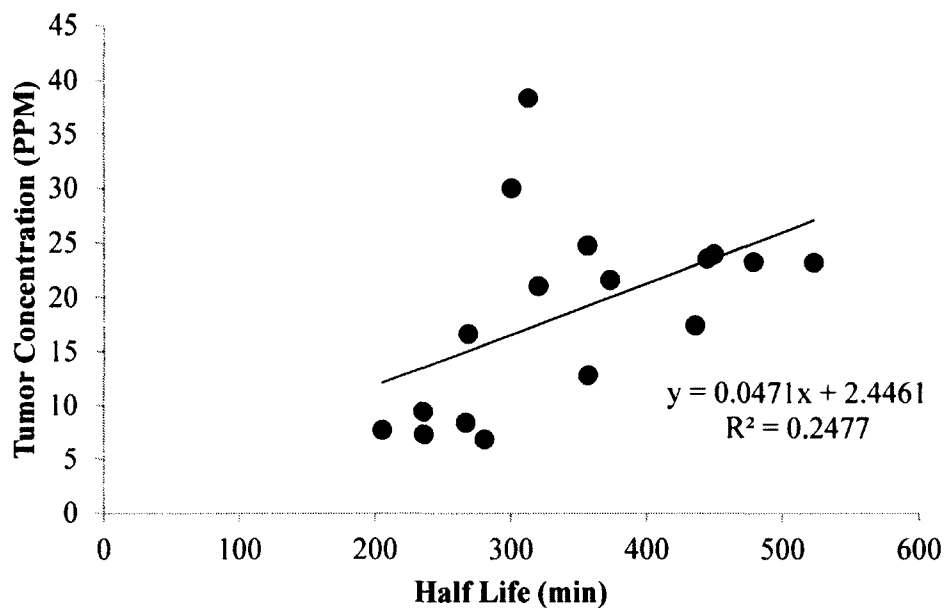
Figure 6-7: Tumor concentration versus half-life. R^2=0.2477.
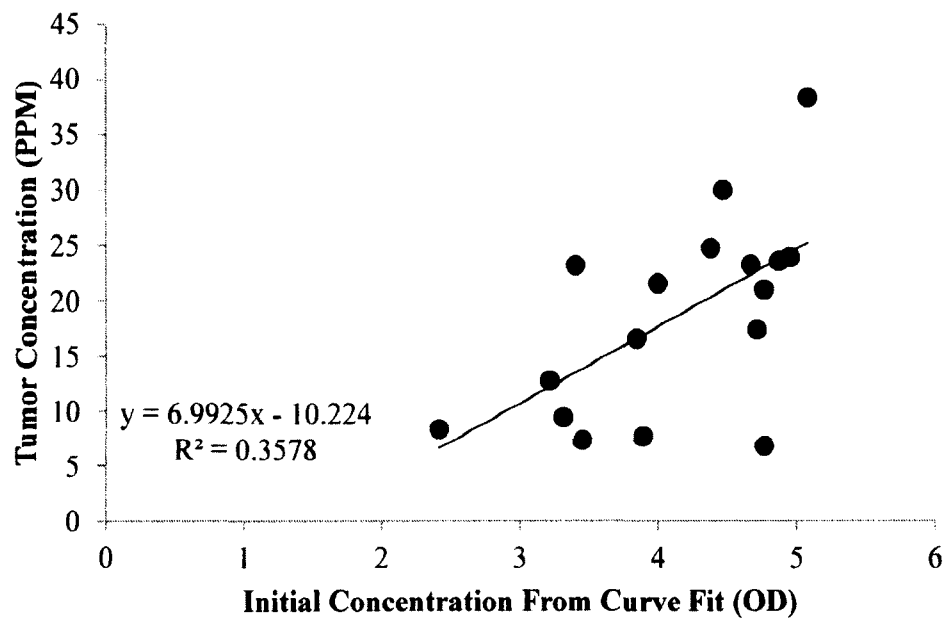
Figure 6-8: Tumor concentration versus initial plasma concentration from exponential curve fit. R^2=0.3578.
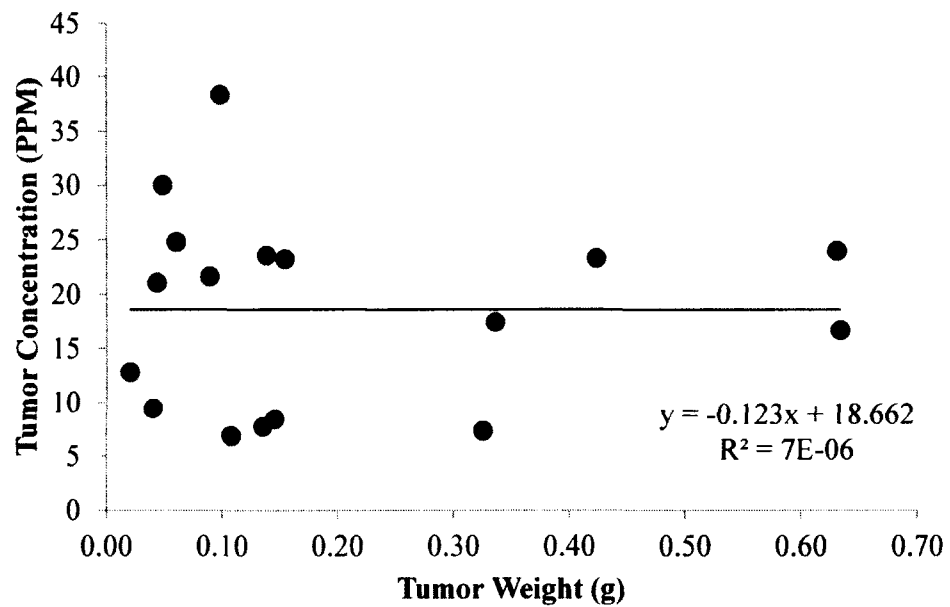
Figure 6-9: Tumor concentration versus tumor weight. R^2=0.000007.

Table 6-2: Half lives for all mice in study (n = 17). Dose group A (n = 8) and dose group B (n = 9) with averages and standard deviations.

	Group A	Group B
Mouse 1	320	444
Mouse 2	357	313
Mouse 3	205	523
Mouse 4	267	373
Mouse 5	235	300
Mouse 6	281	356
Mouse 7	268	435
Mouse 8	236	478
Mouse 9		449
Average	271	408
STDEV	49	76

Table 6-3: P-values for comparison of pharmacokinetic and accumulation parameters between dose groups A and B.

	p-value
Concentration (PPM)	0.000129721
AUC (OD*min)	0.000120694
AUMC (OD*MIN^2)	4.20157E-05
OD Adjusted Dose	6.24664E-07
injected dose (μL)	5.33305E-08
mean residence time	1.87732E-05
Elimination rate constant	0.00044814
half-life (min)	0.000579249
initial concentration from fit (OD)	0.026590645
Tumor Weight (g)	0.703795196

6.4 Discussion and Review of Specifications

The initial experiments elaborated on problems in the protocol, NanoTracker data saving problems, found in the experiments discussed in CHAPTER 4: Animal Protocol Review. Initial intermediate solutions created from the work discussed in Animal Protocol Review CHAPTER 4 were used in the initial experiments. The final solutions implemented because of the previous work and this work are discussed in CHAPTER 4.

In addition to the problems with the NanoTracker data extraction, problems and delays with the elemental analysis protocols caused the loss of those tissue samples. These problems were corrected prior to the beginning of the revised experiments. The elemental analysis technique was more thoroughly established prior to beginning of experiments. To correct the problems with the NanoTracker data a more structured method of saving data was established. Through the initial experiments, we also found a need for more strict data inclusion rules to be established. In addition the UV/Vis blood

draws were eliminated from future procedures due to the potential for human error and the sampling of large (by % of total) volumes of blood without replacement.

6.4.1   Initial Experiments

The half-life data demonstrate an average half-life of 276 minutes and 462 minutes for dose groups A and B, respectively. After statistical testing (t-test) we were able to reject the null hypothesis (equal means) with a p-value of 0.0025 (α=0.05).

6.4.2   Revised Experiments

After analysis of the concentration of gold in the tumors the parameter with the highest correlation (R^2=0.4605) is a linear correlation with mean residence time. Other parameters such as injected dose, area under the blood plasma concentration curve, OD adjusted dose, area under the first moment curve, initial concentration, half-life, and tumor weight which have R^2 values of 0.458, 0.4503, 0.4321, 0.4084, 0.3578, 0.2477, and 0.000007, respectively. These correlations demonstrate the pharmacokinetic parameters which best predict tumor accumulation are mean residence time, injected dose, and area under the blood plasma concentration curve.

Each of these parameters demonstrate a significant difference between dose group A and dose group B except for tumor weight. This finding is logical because all of the other parameters listed involve differences based on given dose, where the tumor weights were controlled to be similar irrespective to dose group.

A review of specifications is presented in Table 6-4, and a subset of this data was presented at the 2012 BMES Annual Meeting on October 27, 2012 in a presentation titled "Real-Time Measurement of the Bioavailability Curve of Experimental Gold Nanorods Towards Dose Optimization," and is a subset of the data in an in-progress publication

titled "A Study of Gold Nanorod Bioavailability and Tumor Uptake in a Murine Model."

This data was also published in a conference proceedings paper titled "LQR Tracking of

a Delay Differential Equation Model for the Study of Nanoparticle Dosing Strategies for

Cancer Therapy". [79]

Table 6-4: Review of specifications.

Specification	Status
Blood plasma concentrations will be collected in near real-time	Specification met through elimination of blood draws and use of NanoTracker
Discrete blood plasma concentrations will be processed quickly (less than 5 minutes) after collection for inclusion in an actively changing one-compartment pharmacokinetic model.	Specification met through use of MATLAB code designed to streamline and create reproducible data analysis
Elemental analysis of tumor tissue is completed in under 12 hours post experiment. Additional data processing time is limited to one hour after completion of instrumentation time.	This specification was met using a rapid elemental analysis protocol discussed in CHAPTER 5.

CHAPTER 7

OBSERVATION OF COFACTORS ON
PREDICTION OF TUMOR UPTAKE
OF GOLD NANOSHELLS

7.1   Introduction and Specifications

An initial analysis using AUC to predict uptake (CHAPTER 6) was unsuccessful

and had large outliers (R^2=0.32, n=8). Recent collaborative modelling efforts examined

the relationship between extravasation and anatomical and physiological variables. [28]

The physiological variables evaluated in the model include vessel-wall pore size,

perfusion, and blood pressure, with flow rate held constant. Based on this modeling

effort, some of these parameters have been collected to study in an effort to control or

improve the predictability of tumor accumulation.   Hyperthermia (38+ deg. C) allows for

the modulation of pore size and flow rate in the subdermal ectopic tumor model used.

[76] Particle size or coatings were not modified because of current status in clinical trials.

Blood pressure was not chemically altered due to a fear of side effects, but was monitored

due to a concern that pressure may be modified during the injection phase and early in the

accumulation phase due to the injected volume or rate of infusion. [86]

This study was designed to test preliminary protocols to monitor mouse blood

pressure, core body temperature, and tumor perfusion. The retrospective review of the

preliminary protocols should include review of the protocols for feasibility and ability to

implement the protocol during the experiment, and determine the efficacy of the current

protocol.

7.2   Materials and Methods

All of the studies involve animal work conducted under protocol approved by the

Louisiana Tech University and Nanospectra Biosciences, Inc. Institutional Animal Care

and Use Committee (IACUC). The animals were handled in accordance with the 'Guide

for the Care and Use of Laboratory Animals'.

7.2.1   Investigation of Cofactors

Nine BALB/c female mice were inoculated with 1.5×10^5 (50 ml injection

volume) CT26.WT murine colon carcinoma tumor cells (ATCC). Pre-experiment

ambient temperature protocols were followed: 35°C for two and a half hours followed by

a minimum of one hour at 39°C immediately prior to injection. Experiment groups were

divided in two groups a "hot" group to remain at 39°C until the end of experiment, and a

"cold" group to return to room temperature (20-25°C) after injection. At a minimum of

one hour prior to injection thermal images of the tumor were collected. The mice were

injected with PEGylated gold nanoshells (four and half µL/g 100 OD). Blood plasma

concentration observations were collected using the NanoTracker to develop a blood

plasma concentration curve and develop pharmacokinetic models. Blood pressure and

rectal temperature was collected at each NanoTracker reading. Elemental analysis of the

tumor samples were conducted using a rapid energy dispersive x-ray fluorescence

technique. [83]

7.2.2   Intravenous Catheters and Cannulation

Intravenous cannulas ware made using two French Polyurethane Catheter tubing

(Access Technologies, Skokie, IL Cat. No BC-2P). On one end, used as the needle for

vascular access, a 28 gauge needle was removed from an insulin syringe (Tyco/

Healthcare ½ mL 28G x ½" insulin syringe REF # 1188528012, VWR Cat. # 84009-742)

and attached to the tubing. On the other end of the tubing a 27 gauge needle (Becton

Dickinson 27G x ½" REF 305109, VWR Cat. # BD305109) was added for slip tip or luer

lock access to the cannula. Injection solution was loaded in a one-milliliter insulin

syringe (Becton Dickinson one-milliliter syringe REF 329650, VWR Cat. # BD329654).

Injection volume and rate were ensured using a syringe pump (New Era Pump Systems,

Inc. Farmingdale, NY. Model # NE-1010).

7.2.3   Temperature Control

Temperature regulation of the mice prior to injection was achieved using a

shaking incubator, with the shaker off (Labnet International, Inc. Edison, NJ. Model #

211DS). During injection and while the mice were under anesthesia the temperature was

controlled using a heating pad (Physitemp Instruments, Inc. Clifton, NJ. Model # TCAT-

2LV) and a space heater for ambient air temperature (Sunbeam Products, Boca Raton,

FL. Model # SFH111).

7.2.4   Gold Nanoshells

PEG modified gold nanoshells (FTS20130919) were obtained from NBI. The

absorption spectra of the nanoshells was obtained using a UV/Vis spectrophotometer

(Beckman Coulter DU 800 Brea, CA.). A one percent dilution of nanorods was made in

DI water to obtain the absorbance at 600, 805, and 940 nm. These values are required as input values of the NanoTracker to ensure proper calculations.

7.2.5   Blood Plasma Concentration Observations

Blood plasma concentration was observed at intervals of approximately: 5, 45, 120, 240, 360, 450, and 720 minutes post injection. These times were based on an assumed six-hour half-life, and altered if an extremely long or short half-life was noted. If it was not possible to collect data at those exact times for any reason the data point was taken early or late to get as close to the correct time as possible.

Blood plasma concentration was collected using the NanoTracker. Data was saved in a raw data directory with the name of the file corresponding to the minutes after injection when data save started. The only metric able to me monitored quickly as the data was passing on the screen was the standard deviation of the two ratios. An effort was made to collect ten "good" data points to ensure 30 seconds of good data (30 seconds is equal to six – five second data points). The required six points was given an extra four points in case some of the other data metrics were not met and some had to be eliminated. All save files were processed by MATLAB code, and if irregularities were found the data was collected again.

7.2.6   One-Compartment Pharmacokinetic Model

Each saved data file (per observation) was processed through MATLAB (APPENDIX B: Sample MATLAB processing code). The MATLAB code was able to provide filtering for noise and unreliable data points. In addition, the MATLAB code created data files and exported charts. The files and charts included metrics of standard

one-compartment pharmacokinetic models including: exponential trend line, r^2, half-life, area under the curve, area under the first moment curve, and mean residence time.

7.2.7   End of Experiment and Animal Termination

The end of experiment was determined to be when the blood plasma concentration reached one optical density plus or minus ten percent. The animal was sacrificed by exsanguination via cardiac puncture, under heavy anesthesia (an intraperitoneal injection of a ketamine (100mg/ml)/zylazine (100mg/ml) mixture at 0.1 ml/10g of body weight). The tumor was collected for elemental analysis; the liver, spleen kidneys, heart, and lungs were collected for potential elemental analysis. [83]

7.3   Results

The tumor accumulation for hot mice ranged from 9-12.6 PPM and the cold mice were 21.9 and 12.4 PPM (shown in Table 7-1).

Table 7-2 elaborated further on standard pharmacokinetic metrics used for evaluation of each injection. The core body temperature and systolic blood pressure measurements did not demonstrate a significant difference between (p-values of 0.14 and 0.065, respectively) the two different test groups. The data is demonstrated in tukey plots for core body temperature (Figure 7-1) and systolic blood pressure (Figure 7-2). The NanoTracker data was used to construct all and average data graphs for hot (Figure 7-3 and Figure 7-4) and cold mice (Figure 7-5 and Figure 7-6). These figures demonstrate the NanoTracker data processed in the form of a rapidly produced one compartment pharmacokinetic model.

Table 7-1: Tumor Accumulation by Mouse. Average tumor accumulation is 13.1 ± 5.2 PPM.

Mouse Number	Experimental Group	Tumor Accumulation (PPM)
20131210A-4	Hot	9.0
20131210B-0	Hot	9.3
20131210B-1	Hot	12.6
20131210A-2	Cold	21.9
20131210A-5	Cold	12.4

Table 7-2: Pharmacokinetic Metrics by Mouse. AUC- Area Under the blood plasma concentration Curve, SBP- maximum observed Systolic Blood Pressure, DBP- maximum observed Diastolic Blood Pressure, Tem- maximum oberved core body Temperature, MRT- Mean Residence Time, $T_{1/2}$- circulation half-life, a- model predicted initial concentration, α- model predicted elimination rate constant, r^2- model correlation coefficient.

Mouse Number & Group	AUC	SBP	DBP	Temp	MRT	$T_{1/2}$	a	α	r^2
A-1 Hot	131.8	133	69	35.7	56.1	368	1.25	-0.002	0.88
A-4 Hot	244.3	132	106	38.7	79.9	183	1.8	-0.004	0.65
B-0 Hot	985.3	144	117	38	250.5	414	2.58	-0.002	0.92
B-1 Hot	271.1	111	62	38.6	110.3	362	1.41	-0.002	0.53
B-2 Hot	567.3	129	96	38.2	167.9	425	2	-0.002	0.98
A-2 Cold	447.0	118	82	38.8	131.6	266	2.1	-0.003	0.95
A-3 Cold	391.3	160	87	38.1	125.1	217	1.99	-0.003	0.97
A-5 Cold	586.0	117	87	38.7	160.9	241	2.46	-0.003	0.86
B-3 Cold	781.5	149	91	32.8	167.7	248	3.19	-0.003	0.89
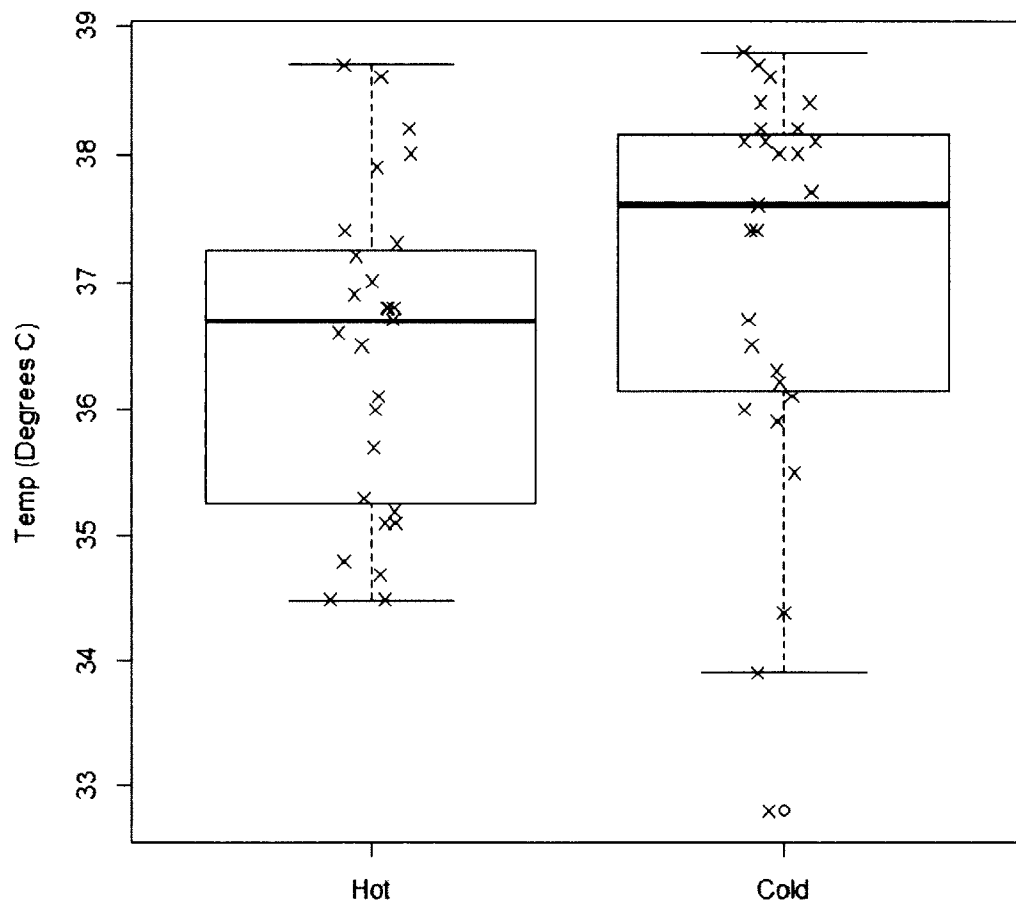
Figure 7-1: Tukey boxplot, with outliers (○). Individual temperature observations are shown (X). The average core temperature was 36.46 ± 1.26 °C and 37.04± 1.56 °C for hot and cold mice, respectively. A student's t-test demonstrated a p-value of 0.140 (α=0.05).
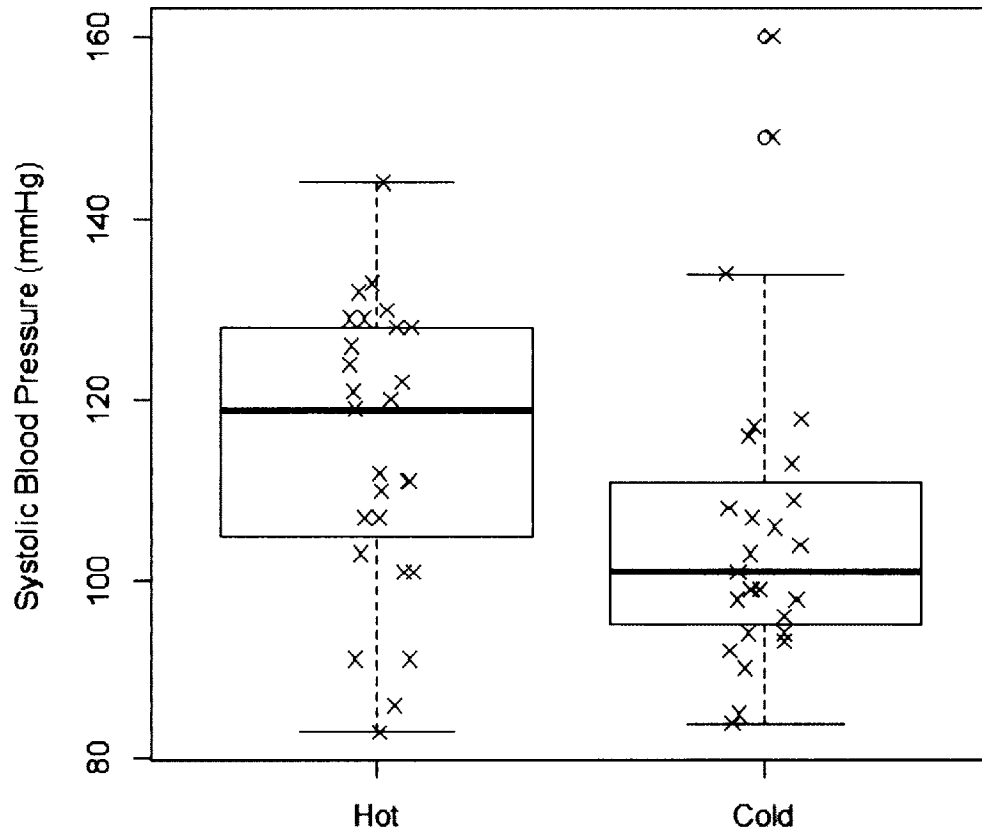
Figure 7-2: Tukey boxplot, with outliers (○). Individual systolic blood pressure observations are shown (X). The average systolic blood pressure was 115 ± 16 mmHg and 106 ± 18 mmHg for hot and cold mice, respectively. A student's t-test demonstrated a p-value of 0.065 (α=0.05).
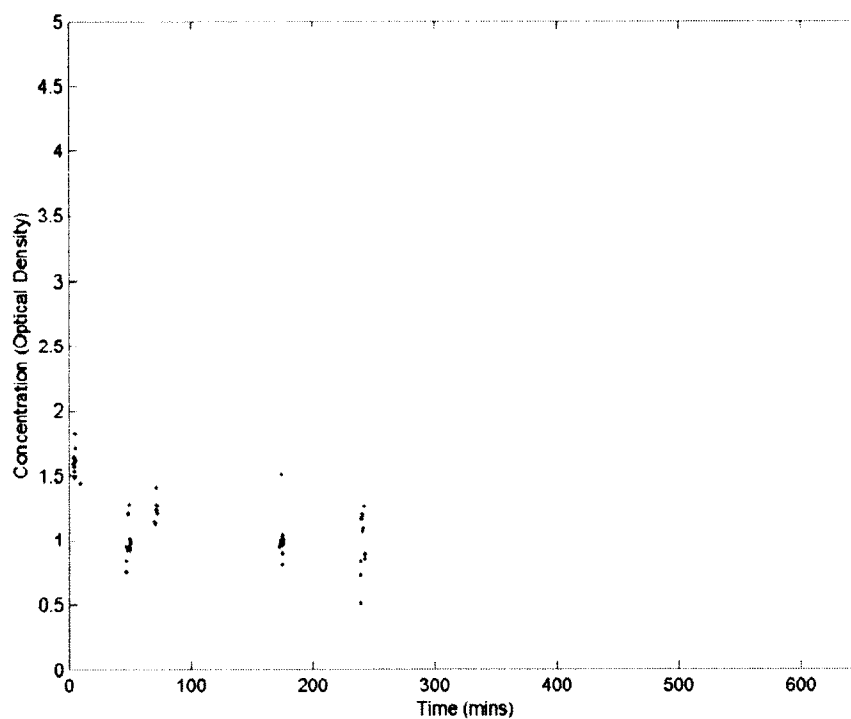
Figure 7-3: All Data Chart for Mouse 20131210B-1: This chart contains every NanoTracker point collected for Mouse 20131210B-1, a member of the hot mouse group.
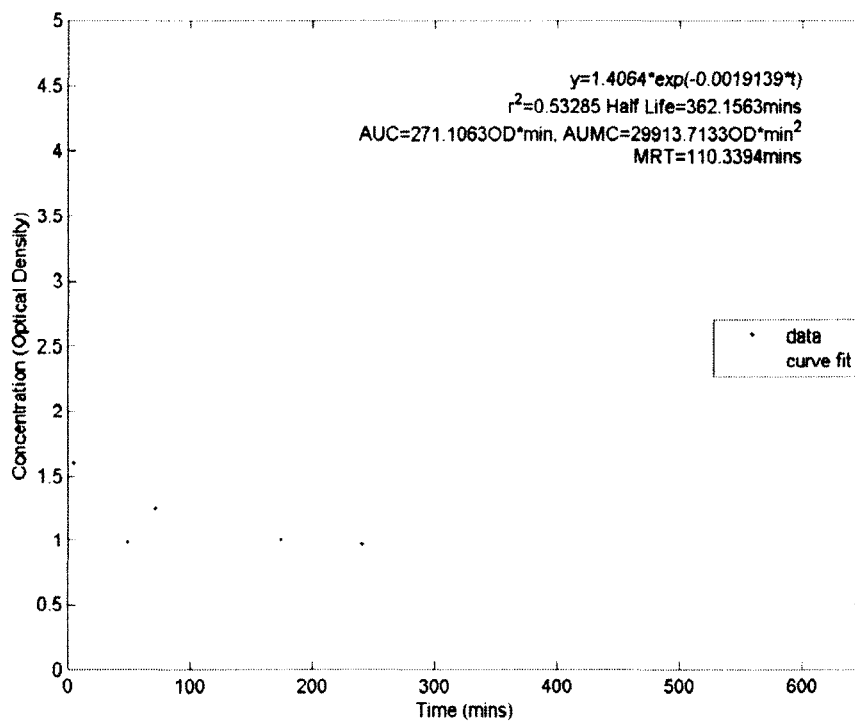
Figure 7-4: Average Data Chart for Mouse 20131210B-1: This chart contains an averaged blood plasma concentration for each representative time point collected for Mouse 20131210B-1, a member of the hot mouse group. The chart also includes values for the exponential fit, half-life, AUC, AUMC, and MRT.
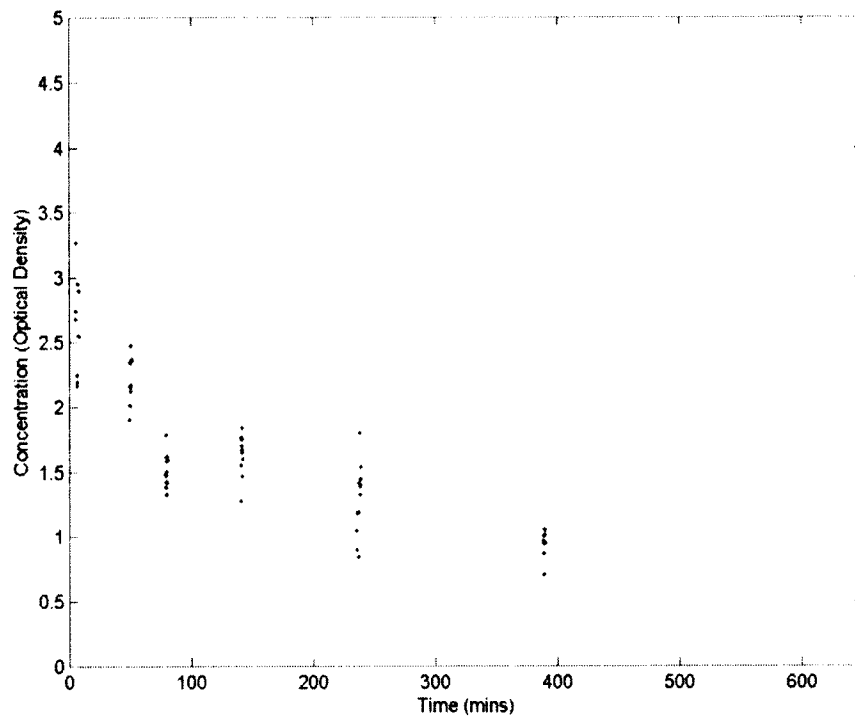
Figure 7-5: All Data Chart for Mouse 20131210A-5: This chart contains every NanoTracker point collected for Mouse 20131210A-5, a member of the cold mouse group.
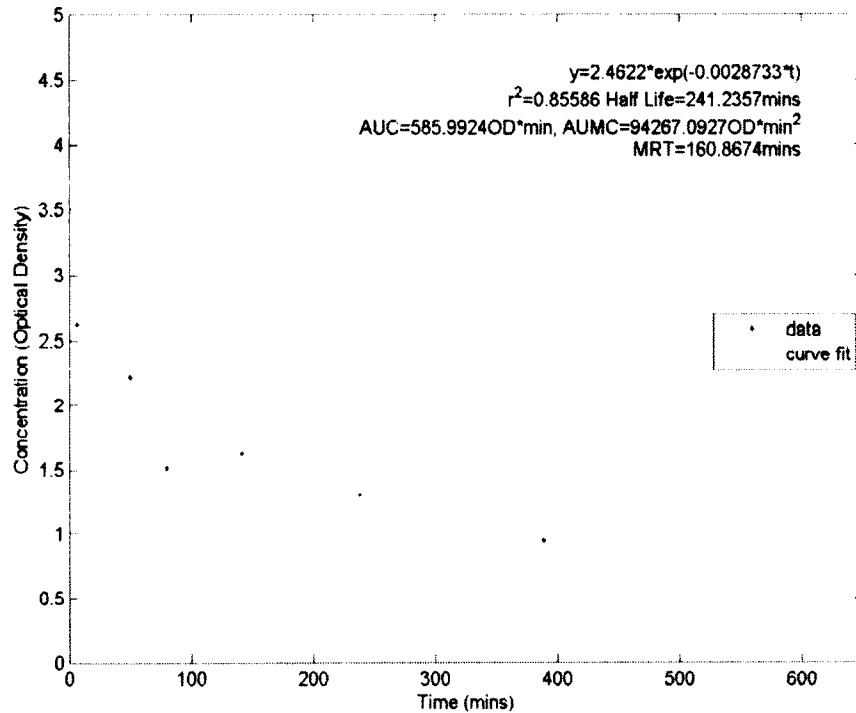
Figure 7-6: Average Data Chart for Mouse 20131210A-5: This chart contains an averaged blood plasma concentration for each representative time point collected for Mouse 20131210A-5, a member of the cold mouse group. The chart also includes values for the exponential fit, half-life, AUC, AUMC, and MRT

7.4 Discussion and Review of Specifications

The hyperthermia protocol was determined to have no effect on the core body temperature of the animal. The average core body temperature of the "hot" group was lower than the average temperature of the "cold" mice. The student's t-test comparing the hot and cold groups revealed a p-value of 0.140. Based on the p-value, we are unable to reject the null hypothesis; the means are not dissimilar. This finding shows that we are not changing the core body temperature using the current ambient temperature protocol. The thermal imaging perfusion protocol was indeterminate, and is currently being redesigned using new instrumentation (Laser Doppler Flowmetry). Future studies (using

Laser Doppler Flowmetry) will have to evaluate the use of this hyperthermia protocol to effect tumor perfusion. The average accumulation values of 13.05 ± 5.23 PPM for the five mice in this data set, and 11.31 ± 5.16 PPM for the eight mice in the 1x data set from zero are very similar. These data sets also produce a p-value of 0.574 when compared using a student's t-test. The cofactors data set of five mice is too small for parametric testing to provide meaningful results, but these values suggest the two data sets are not dissimilar. This comparison suggests the hyperthermia protocol may not be affecting tumor perfusion. The monitoring of blood pressure was determined to be unnecessary. The blood pressure data did not support a difference (based on student's t-test) between the systolic blood pressure of the two groups. In addition, the average systolic blood pressure reading is 110.46 ± 17.22 mmHg. No mouse trended to have higher systolic blood pressures, mice saw transient spikes in blood pressure where high or low values were never seen for more than one point in a row. I was unable to find any trending with time our mouse to describe the behavior of systolic blood pressure. The lack of definitive trends, and the timing difficulty of collecting blood pressure data at each blood plasma concentration reading lead to recommendations to reduce the number of blood pressure readings. The blood pressure readings should be taken at the beginning of the experiment or on multiple days before the experiment to exclude mice with chronic hypertension.

A summary of protocol problems and solutions is presented in Table 7-3, and a subset of this data was presented (presentation title: "The Use of Real-Time Optical Feedback to Improve Outcomes") at Photonics West BiOS on February 2, 2014, with an associated conference proceedings publication. [86]

Table 7-3: Summary of observed protocol problems and solutions.

Observed Problem	Solution
Blood pressure measurements take too long and create delays in data collection	Take fewer blood pressure measurements during accumulation phase.
Ambient temperature protocols do not change the core body temperature of the mouse	Discontinue use of protocols and consider chemically induced systemic hyperthermia
Thermal imaging did not show useable correlations	Consider new instrumentation: Laser Doppler Flowmetry
Blood pressure measurements did not show trends between mice or groups	Suggests lower need for monitoring during accumulation phase.

CHAPTER 8

RETICULOENDOTHELIAL SYSTEM
BLOCKADE AND REDOSING
OF GOLD NANORODS
IN A MURINE
MODEL

8.1   Introduction and Hypothesis

Several types of nanomaterials are under investigation in preclinical and clinical

trials for use in cancer therapies. Current medical-grade particles are constructed from a

variety of materials including lipids, polymers, and metals, [21] and are routinely

delivered intravenously for passive or active accumulation in tumor tissue. [20]

Accumulation via the vascular route increases as the nanoparticle circulation time

increases and the nanoparticle circulation time increases by discouraging their removal

by the reticuloendothelial system (RES). The high removal rate observed by the RES of

charged and hydrophobic particles, [27] which is a requirement of a stable colloidal

system, creates a need to mask the charge by adding a surface coating for nanoparticle

therapies to be most effective.

A common surface coating for stealth nanoparticles is polyethylene glycol (PEG)

which uses steric hindrance to provide for colloidal stability and to prevent the adsorption

of opsonins. [27] PEG, in a liposome formulation, provides a significantly longer half-life

compared to an unshielded type, but some groups show this advantage may diminish in

subsequent injections. [46], [47] Some studies point to PEG as a source of the accelerated

blood clearance (ABC) phenomenon and found that PEG acts as a type-two T cell-

independent antigen. [48], [50] Ichihara and colleagues suggest that the mechanism

responsible for ABC could be anti-PEG IgM [50]; this theory is corroborated by studies

which identified a soluble serum factor as a mediator from serum transfusion studies.

[46], [47]

The Kupffer cells in the liver provide a major removal route of nanoparticles by

the RES. Multiple agents have been evaluated to suppress the actions of the Kupffer cells.

Particles cleared by the RES which can utilize this adjuvant therapy include types of

liposomes, [87] iron oxide nanoparticles, [88] gold nanoshells, [89] gold nanorods, [90]

quantum dots, [91] dendrimers, [92] micelles, [93] and carbon nanotubes. [90] Souhami

and colleagues used dextran sulfate or carbon as a blockade agent and demonstrated

limited success and utility at decreasing clearance. [94] Van Rooijen and colleagues

compared the efficacy of liposome-encapsulated clodronate, propamidine, and

ethylenediaminetetraacetic acid. [95] The results of their study demonstrated propamidine

was the most effective followed by clodronate. [95]

In contrast to the toxic nature of other available RES blockade agents, λ-

Carrageenan demonstrated utility in suppression of hepatic phagocytosis and was

designated as Generally Recognized as Safe (GRAS) by the FDA.[96] This GRAS

designation means that companies might not be required to complete extensive and costly

studies on λ-Carrageenan to prove safety. λ-Carrageenan could be used with particles

currently under investigation as an adjuvant therapy; developers would not have to restart

the trials of their particles due to changes with the surface modification, saving time and money.

This study evaluates RES blockade using λ-carrageenan intravenously administered immediately prior to the injection of PEGylated gold nanorods (NRs). The quantifiable extension of their circulation time was measured using the NanoTracker. [23], [36] The real-time observations were used to create the population pharmacokinetic (PK) model and calculate PK metrics, thus pointing to the potential clinical utility of the optical sensing method.

This study is hypothesis driven work. The hypothesis of this experiment is the use of an adjuvant RES blockade agent will be able to increase the circulation half-life of PEGylated gold nanorods.

8.2   Materials and Methods

8.2.1   Overview

All animals were handled and cared for in accordance with the Louisiana Tech University Institutional Animal Care and Use Committee. Ten BALB/c female mice were initially assigned one of three groups (A, B, or C). In subsequent weeks, some mice were moved between groups B and C and then, after week 3, mice in groups B and C were combined to form group D, as shown in Figure 8-1: Flow chart describing the flow of protocols.. NRs were prepared by Nanospectra Biosciences, Inc. (NBI, Houston, TX) using the methods described by Goodrich and colleagues. [37] Post-manufacturing characterization was performed at NBI prior to shipment (shown in Table 8-1); the extinction spectrum of the gold nanoparticles was measured using a UV-Vis spectrophotometer prior to the injection to quantify concentration and stability.

Intravenous injections and blood plasma concentrations were monitored using the

NanoTracker, and a population pharmacokinetic (PK) model was created from that data.
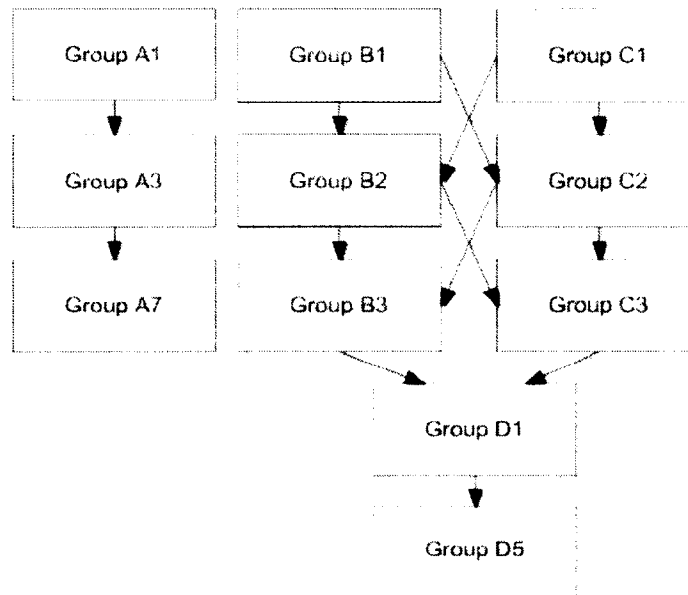
Figure 8-1: Flow chart describing the flow of protocols.

Table 8-1: Post-Manufacturing Characterization.

Approximate Size (TEM)	8 x 24 nm
Absorbance at Peak	91.7 OD @ 762 nm
Absorbance at 800 nm	81.1 OD
Surface Zeta Potential	-11.2mV
CTAB Concentration	60 μM

8.2.2   Injection

Prior to injection, the animals were kept in an incubator set at 37°C for a

minimum of 30 minutes to facilitate intravenous cannulation. Isoflurane inhalation

anesthesia was used to immobilize the animal for injection and to assist with the

collection of the first OD reading. NR (NBI Batch TR20110221) injections were administered via intravenous cannulation of the tail vein. The majority of injections were delivered at a rate of 20 μL/minute by syringe but nine (of 35) injections were made at 40 μL/minute. Optical density data was collected using the NanoTracker. Data was then processed in MATLAB to provide data for pharmacokinetic analysis.

8.2.3 Dose of λ-Carrageenan

A dose of 25 mg/kg body weight was reported [97] to produce sufficient depression of RES functions. The dose was increased to 50 mg/kg to increase the likelihood of a statistically valid result in a small sample group. λ-carrageenan (Sigma 22049-5G-F, CAS 9064-57-7) was added to mammalian normal saline to create a stock solution of 8 mg/mL (chosen due to solubility of λ-carrageenan in saline) and the volume of the stock solution injected was 6.25 μL/g of λ-carrageenan.

8.2.4 Experimental and Control groups

Group A mice were given a standard dose of λ-carrageenan (50 mg/kg) immediately prior to a standard injection of gold NRs (4.5 μL/g of 100 OD NRs). Group B mice received a pre-injection of normal saline equal in volume to that of a standard λ-carrageenan dose immediately prior to a standard NR injection. Group C mice received a standard NR injection. Mice could switch between groups B and C on a weekly basis, as needed. Group D mice received a standard injection of λ-carrageenan immediately prior to a standard NR injection; Group D mice were originally participants in groups B and/or C. Toxicity was not studied during these experiments; however, all animals survived at least 60 days after their last involvement in this study at which point they were assigned to other experimental protocols.

8.2.5 Data collection

Blood plasma concentration in OD was collected using the MWPPG[23], [36] at intervals of approximately: 5, 45, 120, 240, 360, 450, and 720 minutes post injection (see Yendluri 2014 for full blood plasma concentration curves). [98] These times were based on an assumed six-hour half-life, and altered if an extremely long or short half-life was noted. If it was not possible to collect data at those exact times for any reason the data point was taken early or late to get as close to the correct time as possible.

8.2.6 Population Pharmacokinetics

The real-time blood plasma concentration observations were used to create a population PK model to quantify the effect of λ-carrageenan on the circulation of gold NRs. The injected dose was changed from units of μL injected volume to μg of injected gold by multiplying the injected volume by a factor of 2.79 $\mu g/\mu L$ for a 100 OD solution. The blood plasma concentration data was changed from units of OD to units of $\mu g/\mu L$ by multiplying blood plasma concentration in OD by 0.0279 $\mu g/\mu L$ per 1-OD solution, as provided by NBI.

The PK model was fit to blood plasma concentration data in a Bayesian manner using the WinBUGS 1.4.3 [99] software called from R using the R2WinBUGS package. [100] Five chains were used for each analysis with each chain having a burn-in period of 10,000 iterations, a post burn-in period of 10,000 iterations, and every fifth sample was retained. This method results in a total sample of 10,000 iterations. Gelman-Rubin diagnostics were used to confirm convergence of the PK model.

The covariate free PK model compartment structure and variability models were selected by comparing the deviance information criterion of PK models. The following

model components were evaluated: one- and two-compartment structures; absorption; inter-mouse variability and inter-trial variability on PK variables (e.g. clearance and volume of distribution); and additive, proportional, and combined residual error models. Non-informative normal distributions were used as the prior distributions for PK model parameters. Inverse gamma distributions were used for the precision of normally distributed errors.

After selection of the base model, covariate effects of pharmacokinetic model parameters were tested using a backwards elimination technique. The effects of (1) receiving λ-carrageenan (yes/no) on clearance and/or volume of distribution, (2) receiving a pre-injection bolus (yes/no) on clearance and/or volume of distribution, (3) number of previous injections on clearance (Groups B & C only), and (4) an additive model of weight on clearance and volume of distribution were tested. Covariate effects whose 95% credible intervals (CrI) did cross zero were eliminated one-at-a-time until all remaining covariate effects were significant.

The final PK model was used to calculate the circulation half-life and area under the blood plasma concentration versus time curve (AUC) for each mouse trial. A t-test was used to compare the half-life and AUC for mice who received a pre-injection of λ-carrageenan (Groups A &D) with mice that did not (Groups B & C). A P-value less than 0.05 was considered statistically significant.

8.3 Results

A one-compartment model with intravenous injection, inter-trial variability on clearance and volume of distribution, and a proportional error model best fit the data.

Two significant covariates were identified: the effect of pre-injection of carrageenan on clearance rate and pre-injection bolus on volume, shown in Table 8-2.

Table 8-2: Population pharamcokinetic parameters for all trials (n=35).

	Pharmacokinetic Parameter (95% Credible Interval)
Clearance	
... Population Median, No.Carrageenan (Groups: B &C)	18.9 (15.9 - 22.6) μL/min
... Population Median, Carrageenan (Groups: A & D)	11.2 (8.8 - 13.9) μL/min
... Inter-Trial Variability	5.1 (3.4 - 7.8) μL/min
Volume of Distribution	
... Population Median, No Bolus (Group: C)	3,189 (2,392 - 3,906) μL
... Population Median, Bolus (Groups: A, B, & D)	4,180 (3,784 - 4,587) μL
... Inter-Trial Variability	1,041 (772 - 1,420) μL
Residual Variability	14.9% (13.7 - 16.3%)

λ-Carrageenan decreases the median clearance rate from 18.9 (15.9 - 22.6) μL/min to 11.2 (8.8 - 13.9) μL/min, Table 8-2. This decrease results in extending the mean half-life from 160 ± 22 minutes (Groups B & C) to 264 ± 73 minutes (Groups A &D), p<0.01, and raising the AUC of PEGylated gold NRs from 506 ± 142 OD*min (Groups B & C) to 893 ± 324 OD*min (Groups A & D), p<0.01 demonstrated in Figure 8-2. These findings support the previously reported use of λ-carrageenan as a transient RES blockade agent, and extend the circulation of PEGylated gold NRs. Table 8-3 shows the average half-life and AUC values for each sub-group of mice in the experiment.
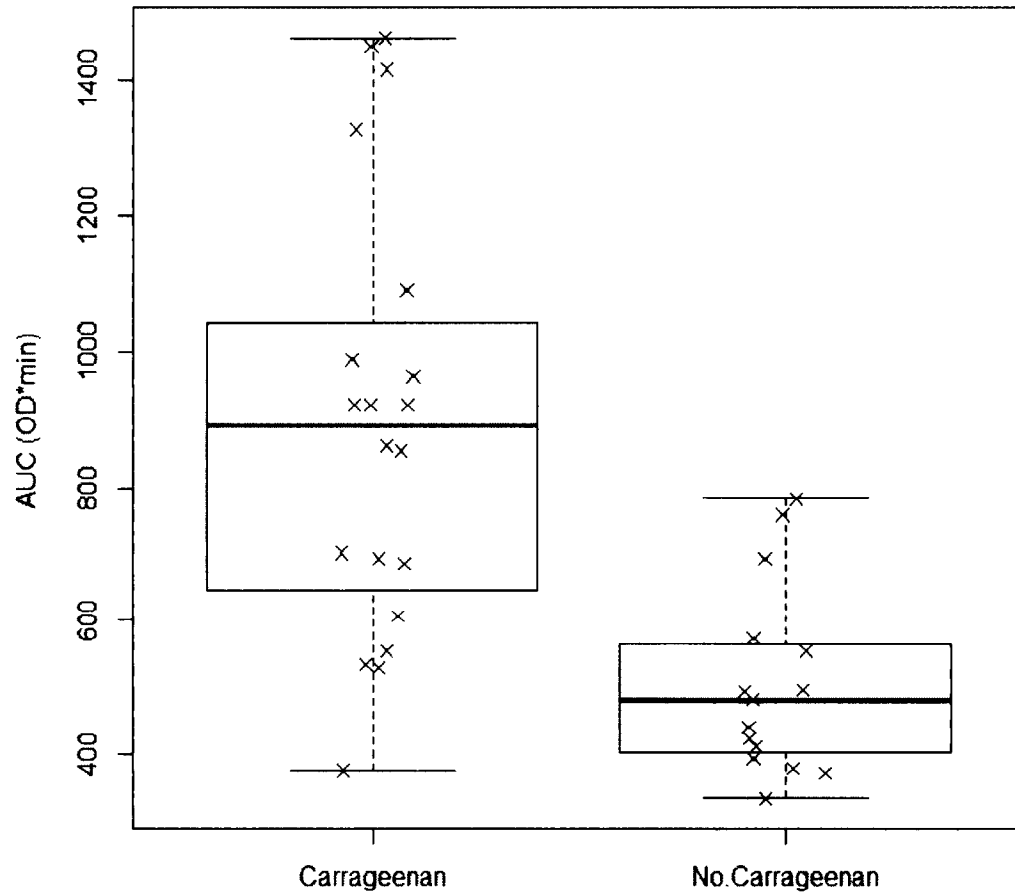
Figure 8-2: Tukey boxplot, with individual trials shown (X). Carrageenan- Groups A & D, No.Carrageenan- Groups B & C.

Table 8-3: Half-life and AUC for each group.

Bolus Type	Group	$t_{1/2}$ (mins) mean ± stdev	AUC (OD*min) mean ± stdev	n
λ-C	A1	358 ± 53	1,301 ± 255	5
	A3	219 ± 47	595 ± 232	4
	A7	173 ± 11	570 ± 53	2
Saline	B1	140 ± 19	435 ± 103	3
	B2	167 ± 20	469 ± 93	3
	B3	161 ± 7	414 ± 80	3
None	C1	190 ± 31	773 ± 17	2
	C2	145 ± 11	487 ± 9	2
	C3	161 ± 26	558 ± 193	2
λ-C	D1	245 ± 42	891 ± 166	4
	D5	257 ± 47	855 ± 143	5

The pre-injection bolus is associated with a significant increase in the volume of distribution. In the trials without a pre-injection bolus the median volume of distribution was 3,198 (95% CrI, 2,392 – 3,906) μL, and in mice with a pre-injection the median volume of distribution was 4,180 (95% CrI, 3,784 - 4,587) μL.

Some additional observations between groups are note-worthy although the small sample size of sub-groups prohibits rigorous statistical analysis. The initial injection following λ-carrageenan pre-injection (A1) appeared to demonstrate a higher AUC value (1,301 OD*min) than the subsequent injections (A3= 595, A7=570 OD*min). This observation seems to support a 4-week redosing cycle similar to PEGylated liposomes as reported by Dams and colleagues. [47] When λ-carrageenan is given to mice with previous NRs exposure, but not previous λ-carrageenan exposure, the AUC increased to near baseline levels (from B2/B3/C2/C3= 474±102 OD*min to D1= 891±166 OD*min), shown in Figure 8-3. In addition, while the PK model did not show a significant redosing effect in groups B & C, there was a trend toward an increase in clearance with redosing
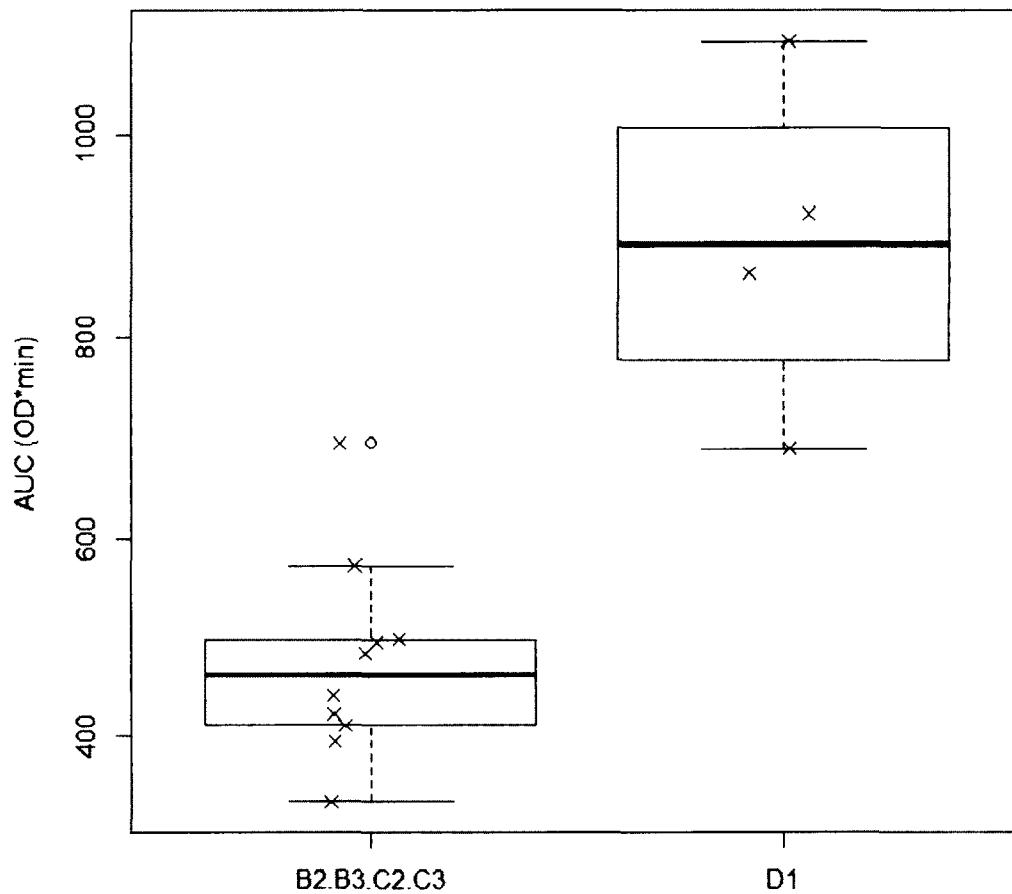
Figure 8-3: Tukey boxplot, with outliers (o). Individual subjects are shown (X). These groups demonstrate the ability of λ-carrageenan to raise the AUC after multiple exposures to PEGylated gold NRs.

8.4 Discussion

The findings of this study demonstrate the utility of λ-carrageenan in increasing

the circulation half-life and AUC of PEGylated gold NRs. In addition, the use of λ-

carrageenan after a series of NR injections was able to increase AUC values to be similar to the AUC of naïve injections. These findings are noteworthy for investigators who wish to achieve the longer circulation times without particle modification, or who wish to use a series of nanoparticle injections.

One finding of note is the significant change in volume of distribution with a pre-injection bolus. This finding is important because of the positive correlation of half-life with volume of distribution; this correlation means an increase in volume of distribution will increase the half-life. A potential for increase in half-life caused by an increase in volume of distribution should be considered during experimental design; investigators should be mindful of pre-injection and injection volumes. Both volumes should be minimized to avoid unnecessary increase in circulation half-life, especially in small animals where small injection volumes are non-negligible relative to the volume of distribution.

A previous study demonstrated an approximated 15% decrease in blood clearance, which suggests a limited utility of RES blockade. [94] However, the current study demonstrates a 59.3% decrease in clearance using a different blockade agent (λ-carrageenan) and using metal nanoparticles in place of liposomes. This demonstrates that RES blockade is a viable mechanism for prolonging the circulation of nanoparticles.

The study design demonstrates the ability to observe changes in volume of distribution based on pre-injection bolus by creating an appropriate number and style of control groups. One limitation of this study is the small sample size in each group. These sample sizes were selected to demonstrate feasibility of λ-carrageenan with the minimal number of animals, and limits the ability to analyze secondary effects such as those noted

as "observations". These observations will require additional testing to confirm the results reported here. In addition, the dosage and dosing strategy will also require further experimentation to optimize. A 50 mg/kg dose of λ-carrageenan was used in this study but the effects on RES blockade and redosing of different λ-carrageenan doses is unknown. No deleterious effects were observed from the use of λ-carrageenan, and all mice survived though 60 days post study when they were assigned to new protocols.

Although the injection rate was double the intended rate (40 μL/min vs. 20 μL/min) for 9 of the 35 injections, because the pharmacokinetic model accounts for the rate of the injection, these deviations are accounted for the pharmacokinetic analysis and do not affect these results. Also, because the time required for all injections (2.5 or 5 minutes) is relatively short compared to the half-life of the NRs (~200 minutes), the effect on the actual OD measurements is minimal.

The same amount of NRs were delivered for all trials and both injection rates are reasonable for mice so physiological differences in the mice (e.g., blowout) at the higher injection rate were neither expected nor observed.

RES blockade, using an agent such as λ-carrageenan, will cause a significant increase in the circulation time and exposure of gold nanorods, which could augment therapeutic efficacy. Future work might seek to establish use and safety guidelines for the intravenous use of λ-carrageenan or identify other viable non-toxic agents for blockade.

This data was presented (presentation title: "The Use of Real-Time Optical Feedback to Improve Outcomes") at Photonics West BiOS on February 2, 2014, with an associated conference proceedings publication, [86] and is the data set for an in-progress

publication titled "Suppression of the Reticuloendothelial System Using λ-Carrageenan to Prolong the Circulation of Gold Nanoparticles"

8.4.1   Summary

1. λ-carrageenan is *generally recognized as safe* by the FDA

2. λ-carrageenan increases the circulation time and AUC of PEGylated gold nanorods, at a higher rate than predicted by previous studies.

3. Increased AUC and circulation time after previous exposure to PEGylated nanoparticles suggests utility to prophylactically minimize ABC.

4. This adjuvant therapy could assist with increasing circulation time and exposure of particles without disrupting experimental trials already underway.

5. Pre-Injection boluses and large injections can increase volume of distribution and therefore increase circulation half-life.

    RES blockade should be effective for all nanoparticles cleared by the RES.

CHAPTER 9

INJECTION NORMALIZATION

9.1   Introduction and Specifications

One noticeable difference in each injection of nanoshells and nanorods in the

large disparity of the initial concentration noticed after injection (noticeable in the data

from

Table 7-2 and Table 8-3, and the graphs in CHAPTER 6 and APPENDIX E). One

theory regarding the large disparity in half-lives and clearance involves the observed

differences in maximum blood plasma concentration. The specification of this work is to

achieve a reproducible maximum blood plasma concentration ± 0.05 OD.

9.2   Methods

The desire to fix this disparity for future testing of importance led to this body of

work to create a more reproducible injection. Three methods have been considered and

tested: equal volumes, 70/30, and rate modified. The equal volumes involved injections

of the same volume regardless of the weight of the mouse (this would completely ignore

the inter-mouse variability on volume of distribution). The 70/30 method would use basic

volume calculations using Eq. 9-1 (where C_x is the concentration of solution one and two,

and V_x is the volume of solution one and two) to calculate an injection volume and inject

70% of that volume. Following a blood plasma concentration reading, the remaining "30%" was injected to appropriately hit a blood plasma concentration target (dose is not conserved).

$$C_1V_1 = C_2V_2 \qquad\qquad \textbf{Eq. 9-1}$$

A sister "Stair Step" protocol where "1/8x" injections were given until close to the target blood plasma concentration when smaller injections could be given at the discretion of the researcher. The final method was designed to inject nanoshells or nanorods until the desired blood plasma concentration was observed (dose is not conserved). The rate is adjusted between ten and 20 µL/min at the discretion of the researcher to ensure the target ±0.05 OD is met.

All of the studies involve animal work conducted under protocol approved by the Louisiana Tech University Institutional Animal Care and Use Committee (IACUC). The animals were handled in accordance with the 'Guide for the Care and Use of Laboratory Animals'.

9.2.1 Intravenous Catheters and Cannulation

Intravenous cannulas ware made using two French Polyurethane Catheter tubing (Access Technologies, Skokie, IL Cat. No BC-2P). On one end, used as the needle for vascular access, a 28-gauge needle was removed from an insulin syringe (Tyco/ Healthcare ½ mL 28G x ½" insulin syringe REF # 1188528012, VWR Cat. # 84009-742) and attached to the tubing. On the other end of the tubing a 27 gauge needle (Becton Dickinson 27G x ½" REF 305109, VWR Cat. # BD305109) was added for slip tip or luer lock access to the cannula. Injection solution was loaded in a one mL insulin syringe (Becton Dickinson 1 mL syringe REF 329650, VWR Cat. # BD329654). Injection

volume and rate were ensured using a syringe pump (New Era Pump Systems, Inc.

Farmingdale, NY. Model # NE-1010).

9.2.2   Temperature Control

Temperature regulation of the mice prior to injection was achieved using a

shaking incubator, with the shaker off (Labnet International, Inc. Edison, NJ. Model #

211DS). During injection and while the mice were under anesthesia the temperature was

controlled using a heating pad (Physitemp Instruments, Inc. Clifton, NJ. Model # TCAT-

2LV) and a space heater for ambient air temperature (Sunbeam Products, Boca Raton,

FL. Model # SFH111).

9.2.2.1   *Blood Plasma Concentration Observations*

Blood plasma concentration was collected using the NanoTracker. Data was

saved in a raw data directory named "injection". The file was imported to Microsoft

Excel for manual filtering to exclude data that does not meet data standards. Graphs of

the injections curves were then plotted in Microsoft Excel.

9.2.3   One-Compartment Pharmacokinetic Model

Each saved data file (per observation) was processed through MATLAB

(APPENDIX B: Sample MATLAB processing code). The MATLAB code was able to

provide filtering for noise and unreliable data points. In addition, the MATLAB code

created data files and exported charts. The files and charts included metrics of standard

one-compartment pharmacokinetic models including: exponential trend line, r^2, half-life,

area under the curve, area under the first moment curve, and mean residence time.

9.3   Results

9.3.1   Equal Volumes

The approximate maximum blood plasma concentration for the equal volumes

was demonstrated to range from two and one tenth to three and one tenth OD,

demonstrated in Table 9-1. Figure 9-1 through Figure 9-7 are the injection profile for

each injection given under this protocol.

Table 9-1: Maximum blood plasma concentrations for equal volumes experiments.

Figure	Approximate Max Blood Plasma (OD)
Figure 9-1	2.8
Figure 9-2	2.6
Figure 9-3	2.4
Figure 9-4	2.4
Figure 9-5	2.1
Figure 9-6	3.1
Figure 9-7	2.7
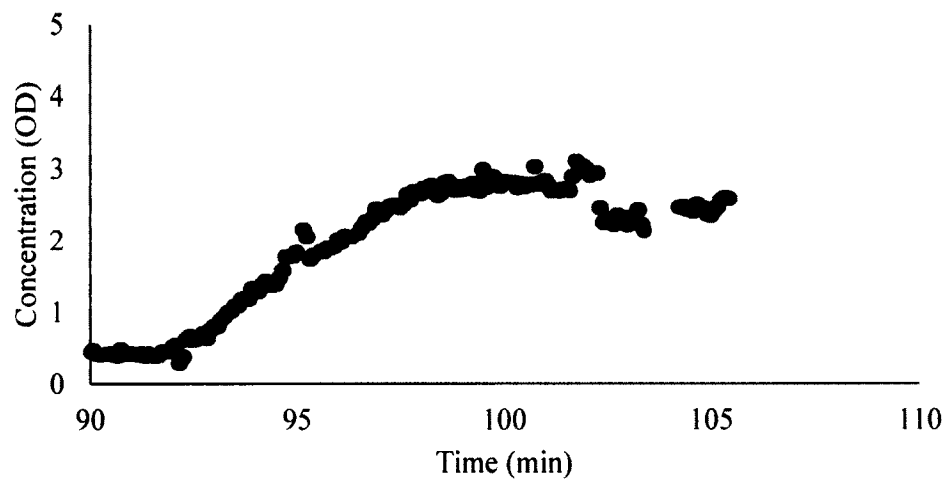
Figure 9-1: Blood Plasma Concentration Curve Mouse A Equal Volumes Injection 1.
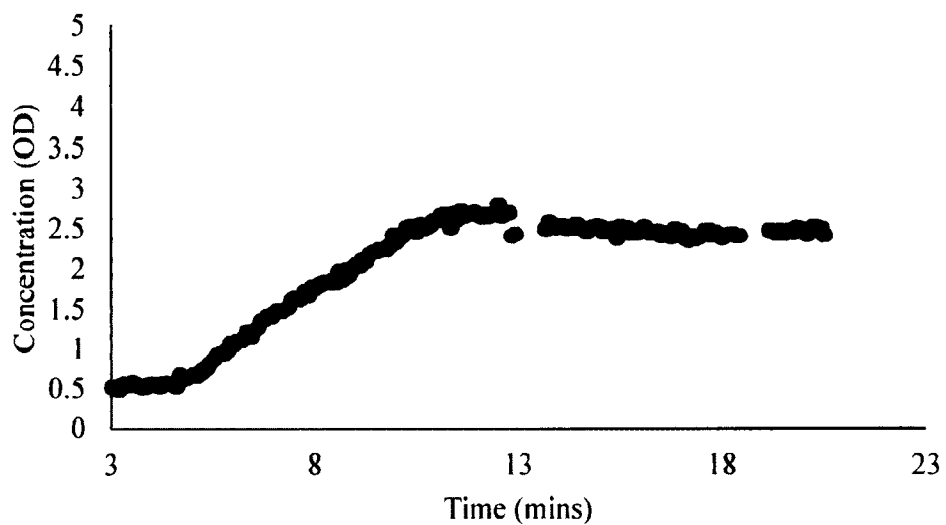
Figure 9-2: Blood Plasma Concentration Curve Mouse A Equal Volumes Injection 2.
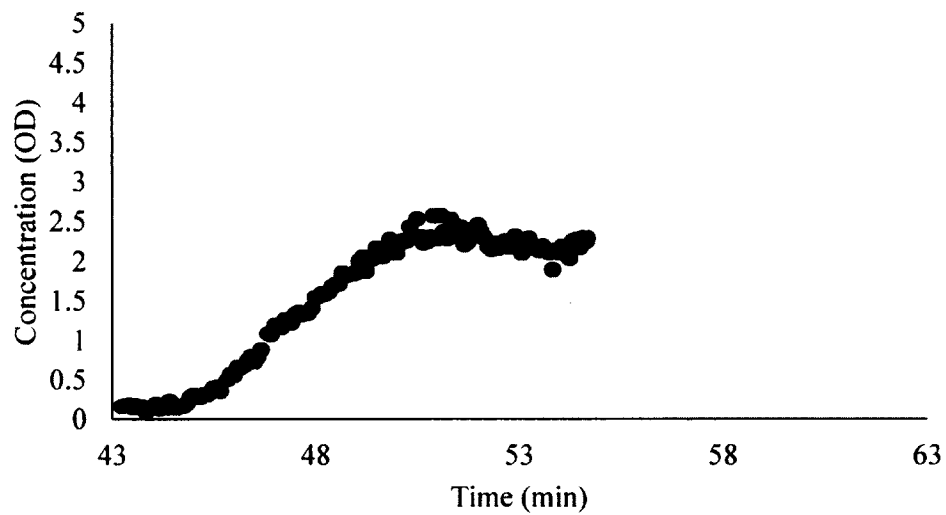
Figure 9-3: Blood Plasma Concentration Curve Mouse B Equal Volumes Injection 1.
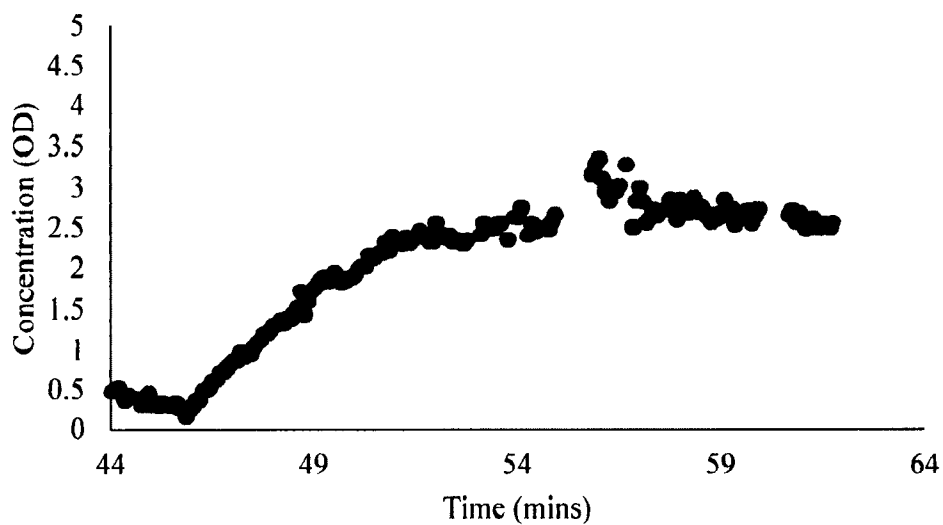
Figure 9-4: Blood Plasma Concentration Curve Mouse B Equal Volumes Injection 2.
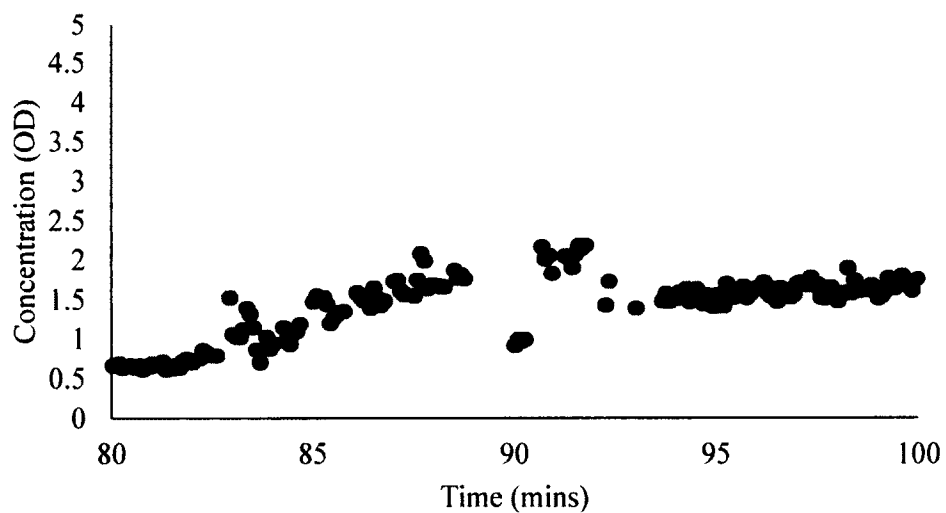
Figure 9-5: Blood Plasma Concentration Curve Mouse 20140728B-0 Equal Volumes Injection.
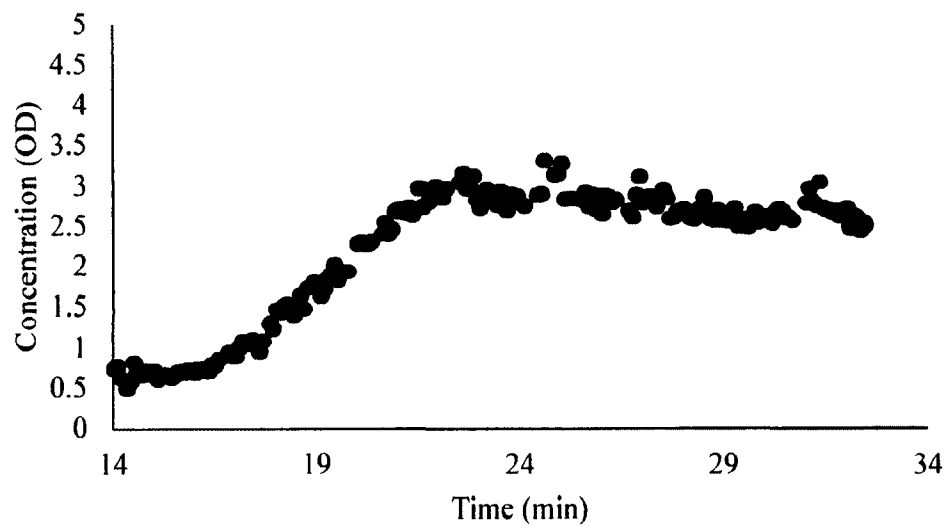
Figure 9-6: Blood Plasma Concentration Curve Mouse 20140728B-2 Equal Volumes Injection.
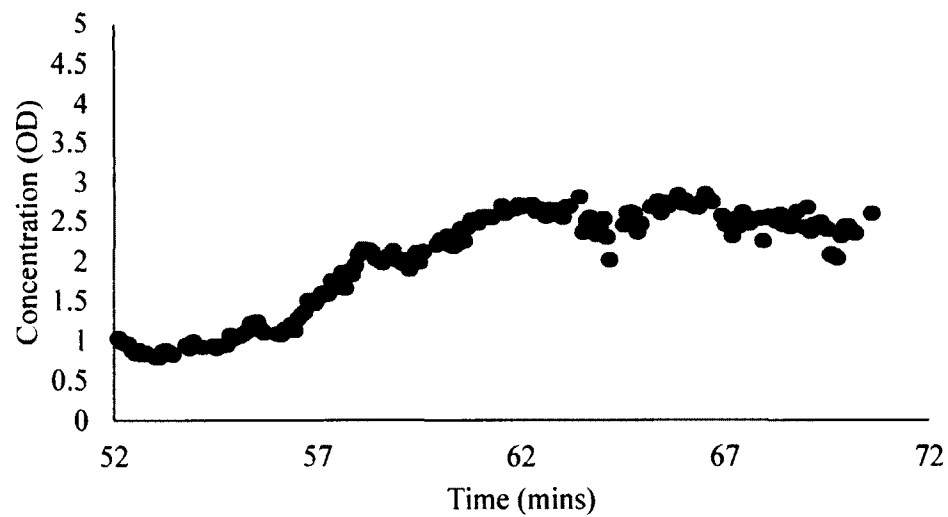
Figure 9-7: Blood Plasma Concentration Curve Mouse 20140728B-3 Equal Volumes Injection.

9.3.2   Step Injections

Table 9-2 shows a sample worksheet for the how calculations were made in the 70/30 step injection with the observed injection profile shown in Figure 9-8. The injection profile of the 1/8x stair step injection is shown in Figure 9-9.

Table 9-2: Mouse 20140728B-1 Stair Step Worksheet.

Mouse #	20140728B-1		70% Volume Target	76.384
Date	2014-11-18 21:38		70% OD Target	3.85
Mouse Weight	24.8		70% OD Observed	3
Mouse Blood Volume	1984		% Observed	77.92%
Target OD	5.5			
Solution OD	100		30% Volume Target	32.736
Target Injection	109.12		Adjusted Volume	42.0112
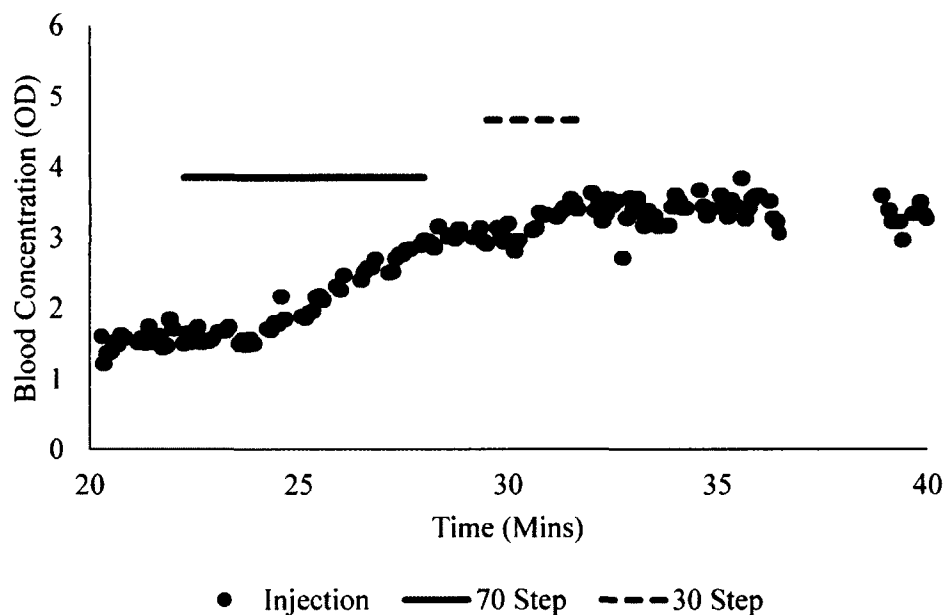
Figure 9-8: Blood Plasma Concentration Curve for Mouse 20140728B-1 70/30 Stair Step. With each observed data point (•), the 70% target (solid line), and the 30% target (dashed line).
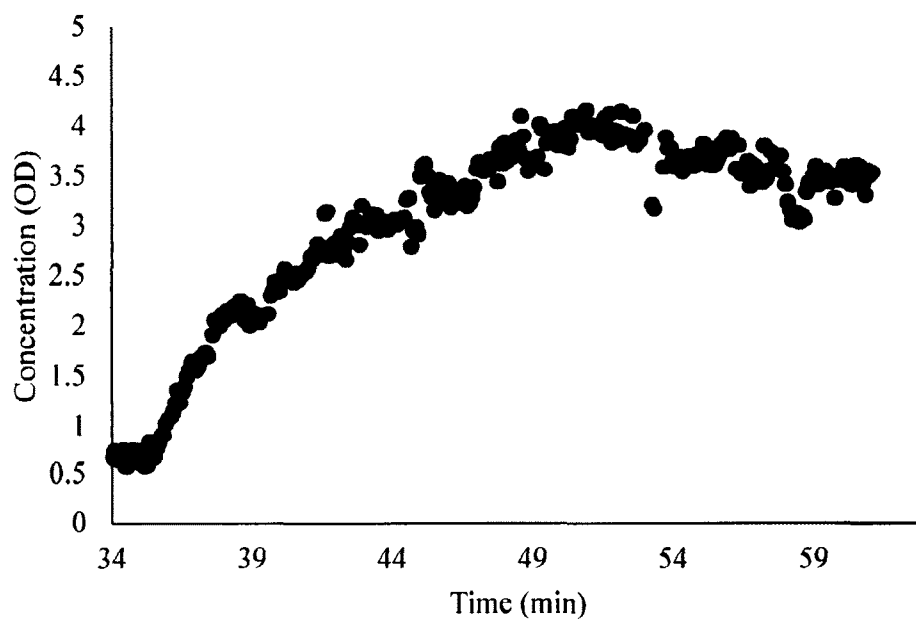
Figure 9-9: Blood Plasma Concentration Curve for Mouse 20140728B-1 1/8x dose Stair Step.

9.3.3   Continuous Infusion

The final protocol, deemed successful, is demonstrated through two successful

injections profiles (Figure 9-10 and Figure 9-11).
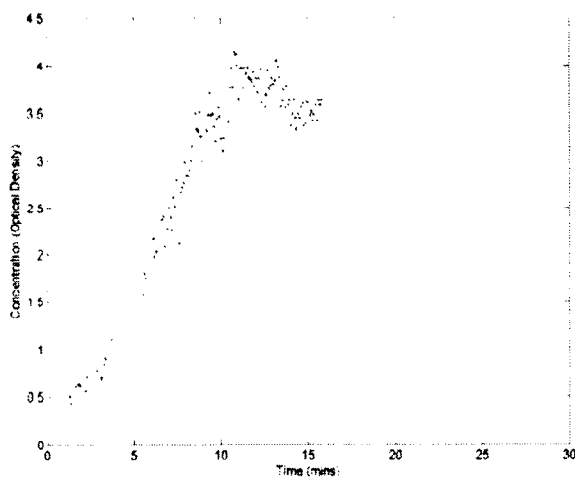
Figure 9-10: Injection phase blood plasma concentration curve for Mouse 20140804-0.
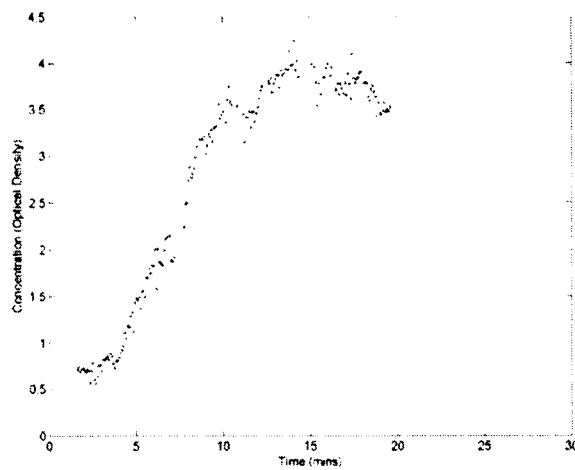
Figure 9-11: Injection phase blood plasma concentration curve for Mouse 20140804-2.

9.4   Discussion and Review of Specifications

9.4.1   Equal Volumes

The equal volumes method was not expected to be meet specifications, but potentially narrow the spread of maximum blood plasma concentrations. It was based on the idea that we were injecting different volumes in different mice and observing different maximum concentrations; we should trying injecting the same volume to observe the outcome. Table 9-1 shows the spread of the data from this group, ranging from 2.1-3.1 OD. This range of data did not meet specifications and the next method was attempted.

9.4.2   Step Injections

The 70/30 stair step shown in Figure 9-8 was created using a convoluted protocol that was not able to attain the level of precision desired. As demonstrated by the target being five and a half OD and the observed maximum blood plasmas concentration being closer to three and a half. The convoluted nature of the injection scheme was filled with problems, such as a difficult to follow protocol regarding the volume of the 30 % step. This particular mistake was made during the injection and caused the final target blood plasma concentration to drop from 5.5-4.65 OD by not attempting to make up for the previously lost concentration in the 70% step. The problems found in the protocol, and ease of mistakes (even by the person who created the protocol) lead to create a more simple "stair step" injection pattern (shown in Figure 9-9). This injection method was successful (and met specifications) in reaching the target blood plasma concentration of

four OD. The idea of discrete injections was abandoned for the creation of the more simple continuous infusion targeted injections.

9.4.3   Continuous Infusion

The continuous infusion method is successful for targeting of maximum blood plasma concentration. The initial plan where injection rate was 20 μL/min for the first 80% of the injection and then slowed to ten microliters per minute caused the noise or discontinuity seen around ten minutes in Figure 9-10 and Figure 9-11. Due to these discontinuities, it is recommended to pick one injection rate (the current recommendation is 15 μL/min) and use it throughout the entire injection. Table 9-3 outlines the summary of specifications and which methods were effective.

Table 9-3: Summary of Specifications.

Specification	Status
Achieve a reproducible maximum blood plasma concentration ± 0.05 OD	Met by both the "Stair Step" and the "Continuous Infusion" method. With the Recommendation: use the "Continuous Infusion" method with a set flow rate of 15 μL/min.

CHAPTER 10

PROTOCOL UPDATES

The experiments discussed throughout this dissertation developed a set of

recommendations on providing more reproducible experiments in a murine model. Each

chapter discusses some of the lessons learned and how these lessons were turned into

specifications for future experiments. This chapter outlines some of the more important

protocol recommendations that are omnipresent in the experimentation of the O'Neal

group.

10.1   Injection

The setup of the catheter system for pre-clinical use can create a loss of fluid that

is a large given the scale of a mouse injection. When using the injection pump system to

give a specified volume to the mouse it is suggested to minimize the number of times a

syringe is changed out. Each time a syringe is changed out some fluid is lost by dripping

out from around the blunt tip connection to the catheter. In a human injection, the loss of

a few microliters from drips during syringe change would be negligible, but with the

small volumes injected for a mouse, it is proportionately large. For this reason the revised

recommendation for injection is to estimate the volume of saline in the tubing prior to

animal catheterization, and add that "dead" volume of saline to the volume of intended

injection and set the syringe pump to the new total volume (injection volume combined

with "dead" volume). When the syringe pump has moved the combined volume into the animal this should minimize the loss of nanoparticles and provide a more reproducible injection. In addition, the use of the same length of catheter tubing (six inches) and needles with the same gauge and length should improve the precision of nanoparticle delivery.

10.2   NanoTracker

10.2.1   Animal Heating

Animals with poor peripheral circulation are difficult to get NanoTracker signals from, due to the location of the probe on the tail. The use of a deltaphase isothermal pad or physitemp feedback heating pad is recommended. In addition to the heating pad, the use of space heaters to ensure the airflow around the mouse is 35-39°C will assist in providing peripheral circulation for an adequate signal.

10.2.2   Data Collection and Analysis

To ensure the reproducible analysis of NanoTracker data a series of MATLAB codes have been developed. These MATLAB codes ensure the basic data standards are met (including: the heart rates from each channel should be ±20% of the computed mean, the AC amplitude should be greater than three millivolts and less than 100 millivolts, and the standard deviation of the optical density readings of the averaged time should be less than 0.03). A sample MATLAB code is shown in APPENDIX B: Sample MATLAB processing code. This code does the following:

- imports the raw data from a saved file

- evaluates each line for the data standards (above)

- ensures the entire time period (default of five seconds) is considered good data

- removes the unnecessary lines of data (the four duplicate lines of the five second time period)

- creates a new array with only the filtered data

- graphs the data (both averaged for a time point and each good data point)

- provides the following (on the graph of time point averaged data)

  o an exponential regression

  o area under the curve (by trapezoidal rule)

  o area under the first moment curve

  o the mean residence time

  o half-life (based off the exponential regression)

- Saves the data files as excel spreadsheets

- Exports the graphs as JPEG and MATLAB figure files

- Can create a "WinBUGS import file"

10.3   Hatteras Blood Pressure System

The Hatteras blood pressure system should be started approximately 30 minutes before the intended use to ensure the animal platform has ample time to warm up. This need for the platform to be warm means the settings must be entered not just the machine being switched on. The balloon should be replaced a minimum of once a week, and pressure tested each day. The high (150 mmHg) and low (50 mmHg) pressure calibration should be performed a minimum of every three days. The mouse tail should be held in

place manually or by restraint system during measurement. The mouse is unlikely to remain motionless for the amount of time needed and will require immobilization of the tail. A set of typical system parameters is given in Table 10-1.

Table 10-1: Summary Hatteras Blood Pressure System Settings.

Parameter	Recommended Value
Preliminary Cycles	3
Measurement Cycles	8
Movement Detection	On
Minimum Pulse Amplitude	6
Number of Peaks	40
Minimum peaks	0.5
Maximum pressure	200
Pulse timeout	30 seconds
Measurement	60 seconds
Time between measurements	2.5 seconds
Systolic threshold	20
Signal below threshold	90
Time below	0.5
Diastolic threshold	80
Signal below	90
Time below	0.5
Temperature	100-110

CHAPTER 11

CONCLUSIONS AND FUTURE WORK

A series of protocol updates and recommendations have been presented. These recommendations are made based on meeting specifications outlined in Table 1-1. The specifications were developed from observed real-world problems in the original pre-clinical and clinical methods, some of which are still in use today. These protocols have been implemented in pre-clinical studies and are driving our work toward a set of "best" practices for nanomedicine. This body of work demonstrates the beginning of a long road of improvements to pre-clinical protocols. Our industrial partner (Nanospectra Biosciences, Inc.) currently conducting pre-clinical and clinical studies has not adopted the protocol improvements made in this dissertation. Closing the gap between the developed pre-clinical practices (in an academic setting) and pre-clinical and clinical setting (in industry) is part of future work that is necessary for a set of best practices to fully develop. The primary goal of these recommendations is improved clinical outcomes. The primary work toward improved clinical outcomes is developing through:

- Making treatment decisions through observation of clinical signs (real-time blood plasma concentration and rapid elemental analysis of biopsied tissue

- Quantifying influential factors, and continuing to search for new factors

- Improved particle characterization (ensuring the solution is what you think you are injecting through UV/vis and/or DLS)

- Ensuring the proper dose is found circulating through real-time blood plasma concentration readings

- Acknowledging problems with the animal model and de-prioritizing model specific problems (i.e. stop solving problems with no clinical relevance, and focus on problems that can improve clinical outcomes)

- Realize not all problems have been found yet and we need to continually reevaluate for new methods of improving clinical outcomes.

In advance of the implementation of industry standard popPK modeling techniques, the NanoTracker and current MATLAB coding were able to create individualized pk models. These individual one-compartment pk models are designed for near-real-time clinical implementation. The personalized one-compartment models provide the ability for comparison of physiological responses to the treatment and allow us to head toward personalized cancer treatments. The popPK models can assist NBI with their ongoing pre-clinical and clinical trials, and provide useful starting point information tailored to the patient (provided from the popPK models).

The protocols associated with the use of the NanoTracker have been evaluated, and modified as needed for use with PEGylated gold nanoshells and nanorods. The protocol updates implemented in this work emphasize the ability to record data for post processing that is more sophisticated. This sophistication includes the ability to reproducibly enforce data quality standards and create graphs, currently with MATLAB. The importance of standardized data analysis and monitoring is found primarily when

future protocols use these devices to inform clinical decisions in real time. Early

academic or pre-clinical studies have the luxury of time for making decisions, but clinical

decisions will be made using this information in an urgent and life threatening climate.

The climate these decisions will be made in highlights the need for standardized and

easily interpreted results. The path toward data driven medicine will involve the

personalized one compartment modeling from real-time blood plasma monitoring, and

ability to observe tumor uptake metrics. The ability to collect tumor uptake data is

available through rapid elemental analysis.

The proposed rapid elemental analysis technique (EDXRF- used in this work)

allows for the quantitative analysis of gold in animal tissues. With a focus on future

clinical implementation, elemental analysis will be required to be completed in under 12

hours. The current 12-hour window is based on timing of currently implemented clinical

treatment protocols. This elemental analysis technique meets these requirements, and

continues to be used in our animal research due to its ease of use and short turnaround

time. Additional quantitative studies would be required to fully validate the technique and

characterize the sources of errors in the protocol prior to human clinical use.

Future work should build on the set of one-compartment models to create a

desired blood plasma concentration curve. From the desired curve there is potential for

the implementation of traditional electrical engineering controls methods [79] to attempt

to ensure a uniform blood plasma concentration curve. In future clinical settings, it will

be possible for the delivery of nanoparticles to be different and contain new dosing

strategies to ensure optimization of tumor uptake. The limitations of our current murine

model only allow for one injection over a short period (limited by the time an animal is

capable of safely being under anesthesia), but clinical work can be conducted with longer infusions (because human infusions can be given with larger variation). In addition to the ability to create a more uniform blood plasma concentration curve from patient to patient, the one-compartment models will be able to assist with the detection of undesired reactions (e.g. anaphylaxis). The use of popPK models could be used to explore individual variables from previous experiments for significant cofactors, and potentially explore minor protocol differences between research groups using particles provided by Nanospectra Biosciences, Inc. As future studies search for improving clinical outcomes, it is important to remember the ideas, protocol updates, and specifications listed here are a starting point. Some factors of clinical importance may not have been discovered yet.

APPENDIX A

MOUSE BLOOD DRAW PROTOCOL

A.1   Theory

Blood draws taken from a mouse post injection of nanoshells can be used to

measure the concentration of circulating nanoshells. UV-Vis spectra of the diluted blood

draws can be analyzed using Beer's Law to separate extinction caused by the

oxyhemoglobin and nanoshells in the sample. This is done by observing the value at the

peak extinction wavelength for nanoshells and by using Eq. A-1:

$$A_{peak} = (\varepsilon_{NS} C_{NS} + \varepsilon_{HbO2} C_{HbO2})D. \qquad \textbf{Eq. A-1}$$

Where A is the extinction at the peak wavelength, the ε's are the extinction

coefficients for the two compounds of interest (oxyhemoglobin(compound b) and

nanoshells(compound a) in this case) at the peak wavelength, and c_{NS} and c_{HbO2} are the

concentrations nanoshells and HbO2. Note that we are using the extinction coefficient

for oxyhemoglobin because the blood samples have been exposed to air in the sampling

process. Therefore, we assume that the hemoglobin is fully oxygenated. Also note that

the extinction is pathlength dependent, but we assume that D is one centimeter.

The concentration of nanoshells in the sample can be expressed using Eq. A-2:

$$C_{NS} = \frac{A_{peak} - \varepsilon_{HbO2} C_{HbO2}}{\varepsilon_{NS}}.$$

<div align="right">**Eq. A-2**</div>

A.1.1   Finding the Extinction Coefficients for Nanoshells

Since Beer's Law expresses concentrations as moles/liter, we will examine the nanoshells as if each one was one atom. Therefore, you will notice that the molarities of nanoshells that are found in each sample are extremely low, but since they are such good extinguishers of light, their molar extinction coefficients will be extremely high. As reported, batches of nanoshells are manufactured to have a peak optical density of 100 at a wavelength between 760 and 820 nm. We will use an optical density of 100 for 760 nm. The molar extinction coefficient is found using Eq. A-3:

$$\varepsilon_{NS} = \frac{A_{NS}}{C_{NS}}.$$

<div align="right">**Eq. A-3**</div>

The concentration of the nanoshells is reported as a number of particles/ml. We can find a molarity from Eq. A-4:

$$\frac{NP\prime s}{ml} * \frac{1000ml}{1L} * \frac{mol}{6.02*10^{23}\ NP\prime s} = \frac{moles\ NP\prime s}{L}.$$

<div align="right">**Eq. A-4**</div>

A.1.2   Blood Draws and Measurements

Once the extinction coefficient used in Eq. A-1 & Eq. A-2 is found, we can inject nanoparticles into a mouse, take blood samples, and examine them. The procedure for taking a blood sample and analyzing it is as follows:

1. Fill a micro-cuvette with 95 µl of 10% Triton-X 100. Blank the spectrometer using that micro-cuvette.

2. Heparinize a ten microliter pipette tip by sucking in five microliter of heparin and then releasing it leaving a layer of heparin inside the tip

3. Obtain a five microliter blood sample using the heparinized tip and mix this with the Triton-X in the cuvette

4. Scan this cuvette using the previously specified wavelengths (500-1100nm) and record the extinction at 805 nm (Let's say that is μ_{805})

5. Dilute the sample using 100 µl Triton-X and scan again and record the extinction at 560 nm (μ_{560})

6. The formula for optical density is as follows, in Eq. A-5:

$$\left(\mu_{805} - \left(\frac{\mu_{560}}{32613}\right) * 2 * 840\right) * 20 = OD. \qquad \textbf{Eq. A-5}$$

A.2 Adjustments

There will be an error in volume. To adjust for that multiply the final OD value by

$$\frac{1.95}{\mu_{560}}.$$

A.3 Calibration Curve/Typical Results

The spectra from blood draws taken from a mouse injected with nanoparticles can be seen in Figure A-1, and the calibration curve is shown in Figure A-2.

Blood/NS Extinction Spectra

Optical Density (Abs. Units)

0.45
0.4
0.35
0.3
0.25
0.2
0.15
0.1
0.05
0

650   750   850   950   1050

Wavelength

— Raw Blood
— 1.70E10 NP/mL
— 1.36E10 NP/mL
— 1.02E10 NP/mL
— 6.8E9 NP/mL
— 3.40E9 NP/mL

Note: Concentrations in NP/mL blood
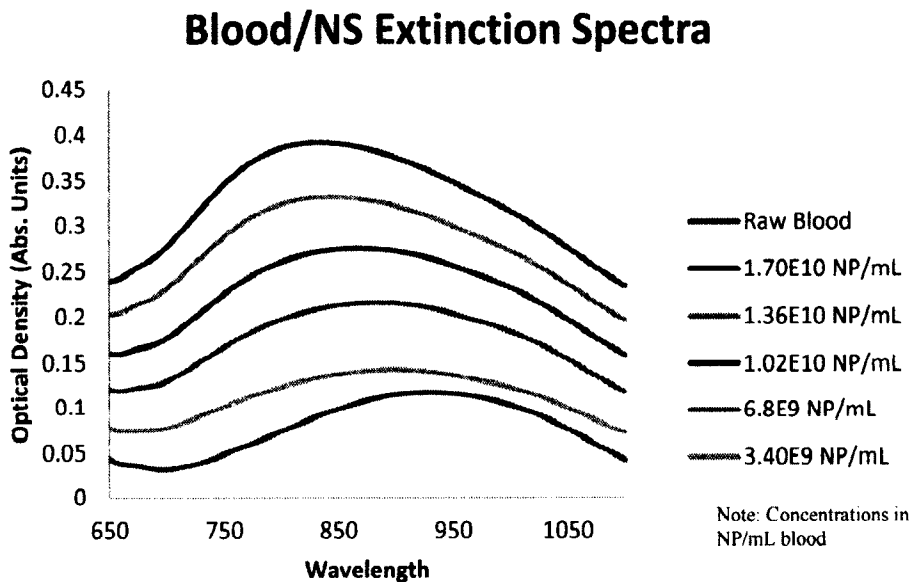
Figure A-1: Extinction spectra of blood prior to (raw blood) and post (all other spectra) injection. Note how the extinction at 760 nm increases greatly in comparison to 940 nm and then begins to return to a spectrum more like that for raw blood.

Calibration Data for Nanoshell Concentrations in Blood

Calculated NS/ml blood

2E+10
1.5E+10
1E+10
5E+09
0

$y = 0.6671x + 5E+08$
$R^2 = 0.9744$

0   1E+10   2E+10   3E+10

Known NS/ml blood
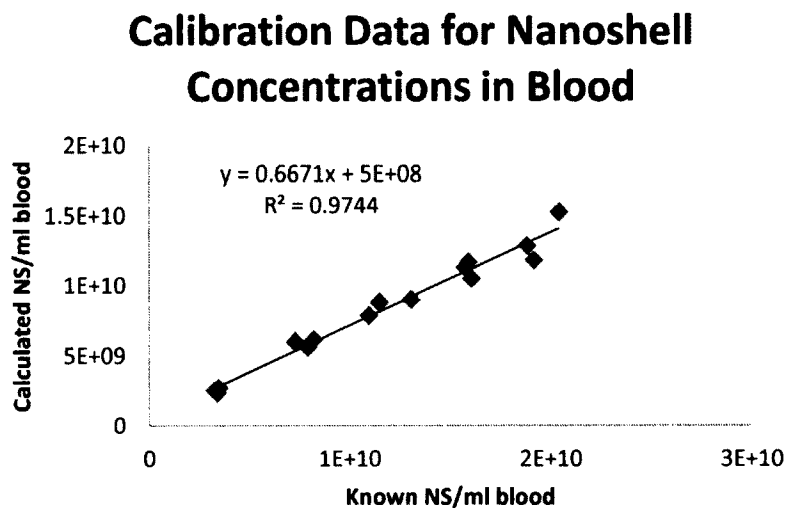
Figure A-2: Calibration curve comparing the calculated nanoshell concentration in samples containing blood and nanoshells to samples containing only known concentrations of nanoshells.

APPENDIX B

SAMPLE MATLAB PROCESSING CODE

The code below is an example of the MATLAB processing code used to process NanoTracker data. The purpose of this particular code is to extract the data from the RES Blockade experiments, process and create basic blood plasma concentration graphs, and create the input files for WinBUGS.

```
clear all

clc

close all

mousenumber=input('enter mouse number as YYYYMMDD(CAGE)-(MOUSE): ','s');

InjectionVolume1=input('enter the volume of 100 OD NS or NR ');

InjectionVolume=InjectionVolume1-75;

MouseWeight=input('enter the weight of the mouse ');

group=input('enter the group number ','s');

Dose=(InjectionVolume)/(4.5*MouseWeight);

InjectionVolumeSTR=num2str(InjectionVolume);

MouseWeightSTR=num2str(MouseWeight);

DoseSTR=num2str(Dose);

nonmem(1,:)={'#ID','TIME','AMT','RATE','DV','MDV','DOSE','WT'};
```

```
nonmem(2,:)={'ID' '0' InjectionVolumeSTR '0' '.' '1' DoseSTR MouseWeightSTR};

alldata=zeros(1,24);

numberofdp=input('enter the number of data points: ');

countdp=1;

while countdp <=numberofdp

clear rawdatafile; clear rawdata; clear timeresolveddata;

clear prelimfiltereddata; clear filtereddata

%PULL DATA FILE & TIME RESOLVE


filestarttime=input('Enter start time of file ', 's');

rawdatafile=['C:\Users\ibmag_000\Documents\Dropbox\NCTSG Lab\Raw
Data\Carrageenan Eperiments\WinBUGS\',mousenumber,'\',filestarttime];

filestarttime=str2double(filestarttime);

rawdata=load(rawdatafile);

initialtime=rawdata(1,10);

timeresolveddata=rawdata;

timeresolveddata(:,10)=rawdata(:,10)-initialtime+filestarttime;



count=1;

count2=1;

length=size(rawdata);

length1=length(1,1);

while count <= length1 %the purpose of this while loop is to remove rows with bad data
```

```
%CHECK HR STDEV

clear X;

X=[timeresolveddata(count,1) timeresolveddata(count,2) timeresolveddata(count,3)];

average=mean(X);

averageminus=average*0.8;

averageplus=average*1.2;


if timeresolveddata(count,1) <= averageplus

    includeHR=1;

else

    includeHR=0;

end

if timeresolveddata(count,2) <= averageplus

    includeHR1=1;

else

    includeHR1=0;

end

if timeresolveddata(count,3) <= averageplus

    includeHR2=1;

else

    includeHR2=0;

end
```

```
%------------------------------

if averageminus <= timeresolveddata(count,1)

    includeHR3=1;

else

    includeHR3=0;

end

if averageminus <= timeresolveddata(count,2)

    includeHR4=1;

else

    includeHR4=0;

end

if averageminus <= timeresolveddata(count,3)

    includeHR5=1;

else

    includeHR5=0;

end

%CHECK AC AMPLITUDE

if timeresolveddata(count,7) <= 0.10

    includeAC=1;

else

    includeAC=0;

end

if timeresolveddata(count,8) <= 0.10
```

```
    includeAC1=1;

else

    includeAC1=0;

end

if timeresolveddata(count,9) <= 0.10

    includeAC2=1;

else

    includeAC2=0;

end

%------------------

if 0.003 <= timeresolveddata(count,7)

    includeAC3=1;

else

    includeAC3=0;

end

if 0.003 <= timeresolveddata(count,8)

    includeAC4=1;

else

    includeAC4=0;

end

if 0.003 <= timeresolveddata(count,9)

    includeAC5=1;

else
```

```
        includeAC5=0;

end

%CHECK STDEV

if timeresolveddata(count,13) <= 0.03

    includeSTDEV=1;

else

    includeSTDEV=0;

end

if timeresolveddata(count,16) <= 0.03

    includeSTDEV1=1;

else

    includeSTDEV1=0;

end




INCLUDE=includeHR*includeHR1*includeHR2*includeHR3*includeHR4*includeHR5
*includeSTDEV*includeSTDEV1*includeAC*includeAC1*includeAC2*includeAC3*in
cludeAC4*includeAC5;




    if INCLUDE == 1

        prelimfiltereddata(count2,:)=timeresolveddata(count,:);

        count2=count2+1;

    else

    end
```

```
    count=count+1;

end



%REMOVE DUPLICATE LINES

count=3;

count1=1;

length2=size(prelimfiltereddata);

length3=length2(1,1)-2;

while count <= length3 %remove duplicate values

%EXTRACT BY STDEV1

    if prelimfiltereddata(count,13)== prelimfiltereddata(count+2,13);

        includeplustwo1=1;

    else

        includeplustwo1=0;

    end
%-----------------------------------

    if prelimfiltereddata(count,13)== prelimfiltereddata(count-2,13);

        includeminustwo1=1;

    else

        includeminustwo1=0;

    end
%-----------------------------------

INCLUDE1=includeplustwo1*includeminustwo1;
```

```
if INCLUDE1 ~=0

    filtereddata(count1,:)=prelimfiltereddata(count,:);

    count1=count1+1;

else

end

count=count+1;

end

numberofgooddatapoints=size(filtereddata);


averagedata(countdp,1)=mean(filtereddata(:,10)); %time

averagedata(countdp,3)=mean(filtereddata(:,18)); %optical density

averagedata(countdp,2)=numberofgooddatapoints(1,1); %number of points being
averaged


alldata=[alldata;filtereddata];


TimeSTR=num2str(averagedata(countdp,1));

OD_STR=num2str(averagedata(countdp,3));


nonmem(countdp+2,:)={'ID' TimeSTR '0' '0' OD_STR '0' DoseSTR MouseWeightSTR};


countdp=countdp+1;

clear TimeSTR
```

```
clear OD_STR

end
```

%Exponential Regression

```
mdl=@(a,x)(a(1)*exp(-a(2)*x));

a0=[7;0.004];

beta=nlinfit(averagedata(:,1),averagedata(:,3),mdl,a0);

xrange=0:0.01:1030;

uganda=mdl(beta,xrange);

averagedata(:,4)=mdl(beta,averagedata(:,1));

r=corr2(averagedata(:,3),averagedata(:,4));

rsquarred=r^2;

halflife=log(.5)/-beta(2,1);
```

%Calculate AUC

```
data1= [0 0 averagedata(1,3) 0];

data2=[data1;averagedata];

data2(:,5)=data2(:,1).*data2(:,3);

AUC=trapz(data2(:,1),data2(:,3));

AUMC=trapz(data2(:,1),data2(:,5));

MRT=AUMC/AUC;
```

```
AUCs=num2str(AUC);

AUMCs=num2str(AUMC);

MRTs=num2str(MRT);



fig1=figure(1);

MM=num2str(filtereddata(1,20));

DD=num2str(filtereddata(1,21));

YYYY=num2str(filtereddata(1,19));

doe=[MM,'/',DD,'/',YYYY];

plot(averagedata(:,1),averagedata(:,3),'b.',xrange,uganda,'g-.')

titlestr=['CARRAGEENAN Mouse ',mousenumber,' Date of Experiment: ',doe];

title(titlestr);

betaA=num2str(beta(1,1));

betaB=num2str(beta(2,1));

halflifestr=num2str(halflife);

rsquarred2=num2str(rsquarred);

annotationstr{1}=['y=',betaA,'*exp(-',betaB,'*t) r^2=',rsquarred2,' Half
Life=',halflifestr,'mins'];

annotationstr{2}=['AUC=',AUCs,'OD*min. AUMC=',AUMCs,'OD*min^2
MRT=',MRTs,'mins'];

text(25,0.5,annotationstr)

legend('data','curve fit')

xlabel('Time (mins)');

ylabel('Concentration (Optical Density)');
```

```
axis([0 400 0 4.5]);



fig2=figure(2);

plot(alldata([2:end],10),alldata([2:end],18),'b.')

titlestr=['CARRAGEENAN Mouse ',mousenumber,' Date of Experiment: ',doe];

title(titlestr);

xlabel('Time (mins)');

ylabel('Concentration (Optical Density)');

axis([0 400 0 4.5]);




savestr=['C:\Users\ibmag_000\Documents\Dropbox\NCTSG
Lab\Carrageenan\Data\WinBUGS\Group ',group,'\Group',group,'Mouse',mousenumber];

%--------Save Average Data Sheet and Figures

saveas(fig1,[savestr,'averagedata']);

saveas(fig1,[savestr,'averagedata.jpg']);

header={'Time','Number of Points','Average OD','Curve Fit OD at time'};

xlswrite([savestr,'averagedata'],header,'sheet1');

xlswrite([savestr,'averagedata'],averagedata,'sheet1','A2');

%--------Save All Data Sheet and Figures

alldataheader={'HR1','HR2','HR3','DC1','DC2','DC3','AC1','AC2','AC3','TIME','R1','AV
G R1','STDEV R1','R2','AVG R2','STDEV
R2','SPO2','OD','YEAR','MONTH','DAY','HOUR','MIN','SEC'};

saveas(fig2,[savestr,'alldata']);

saveas(fig2,[savestr,'alldata.jpg']);

xlswrite([savestr,'alldata'],alldata,'sheet1','A1');
```

```
xlswrite([savestr,'alldata'],alldataheader,'sheet1','A1');

%--------Save nonmem

xlswrite([savestr,'nonmem'],nonmem,'sheet1','A1');

beep
```

APPENDIX C

2,2,2-TRIBROMOETHANOL (AVERTIN)

Avertin is useful for use in procedures where immobilization is less than 20 minutes and with no significant pain or distress. Avertin should provide good skeletal muscle relaxation and a moderate degree of respiratory depression.

C.1   Contraindication

Repeated administrations of avertin are contraindicated.

Do **NOT** inject intravenous, animal death would be expected within minutes.

C.2   Materials

2,2,2-tribromoethanol (Sigma-Aldrich T48402)

2-Methyl-2-Butanol (Alfa Aesar A18304)

C.3   Avertin Stock Solution

Mix:

1. 15 g 2,2,2-tribromoethanol

2. 15.5 mL 2-Methyl-2-Butanol

3. Mix overnight in dark (amber) bottle at room temperature. (be sure to use clean stir bar)

The stock solution has a shelf life of six months when stored wrapped in foil in a dark cabinet at room temperature. The following information **MUST** be on the outside of the bottle and the box the bottle is stored in: Solution, Expiration date, grams of 2,2,2-tribromoethanol and lot number, mL 2-Methyl-2-Butanol and lot number.

C.4   Avertin Working Solution

Mix:

1. 0.1 mL Avertin Stock Solution

2. 7.9 mL 0.9% Sterile Saline

3. Mix in a dark bottle and store overnight

4. Filter sterilize with 0.22 μm filter, label and store at four to six degrees Celsius.

    Working solution has a shelf life of six months if unopened.

    Once the working solution has been opened it has a shelf life of **one week**.

All containers of working solution must be labeled with the following information: Solution, Expiration date (once opened), Date of sterilization, Your Initials, mL Avertin stock solution, mL saline.

C.5   Animal Injection

Avertin is given via intraperitoneal (IP) injection of Avertin Working Solution at the following dose:

Normal injection for slow particle infusion: 25 μL/g body weight.

Normal injection for standard immobilization: 20 μL/g body weight.

APPENDIX D

# USE OF REAL-TIME PHARMACOKINETICS
TO PREDICT TUMOR UPTAKE
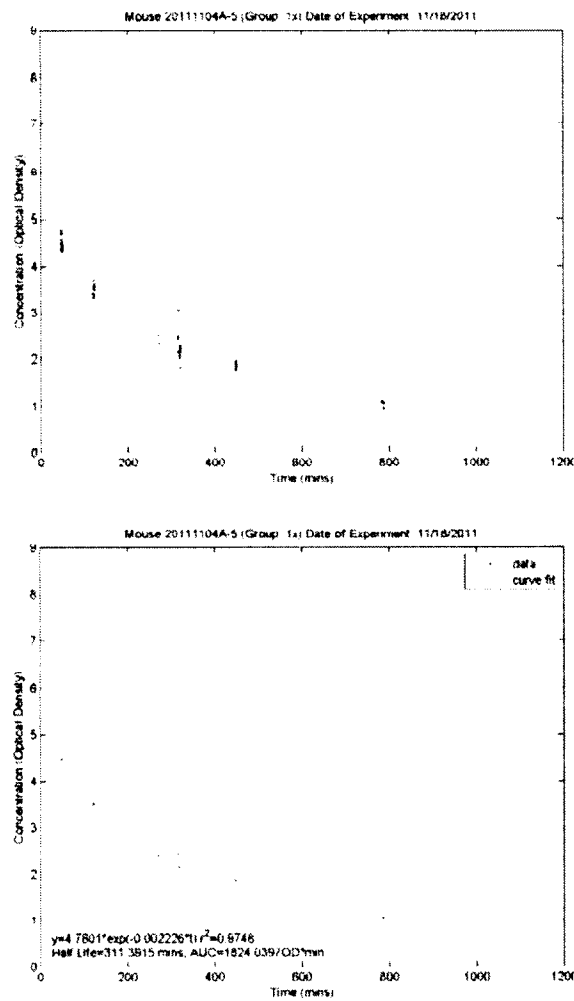
Figure D-1: Charts for mouse 20111104A-5 (Group A- 21.08PPM). Top: All Data, Bottom: Averaged Data.
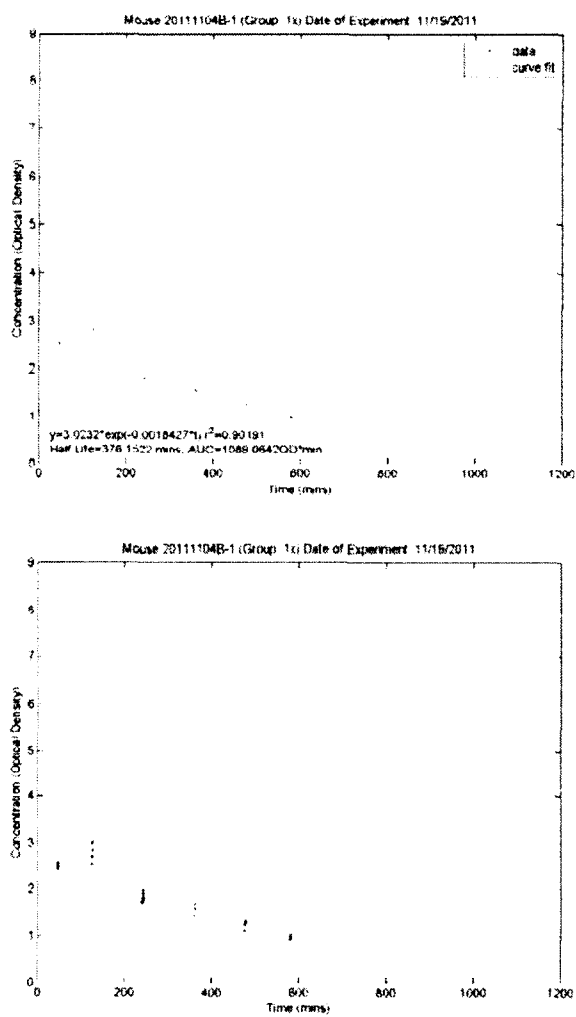
**Figure D-2:** Charts for mouse 20111104B-1 (Group A- 12.83 PPM). Top: All Data, Bottom: Averaged Data.
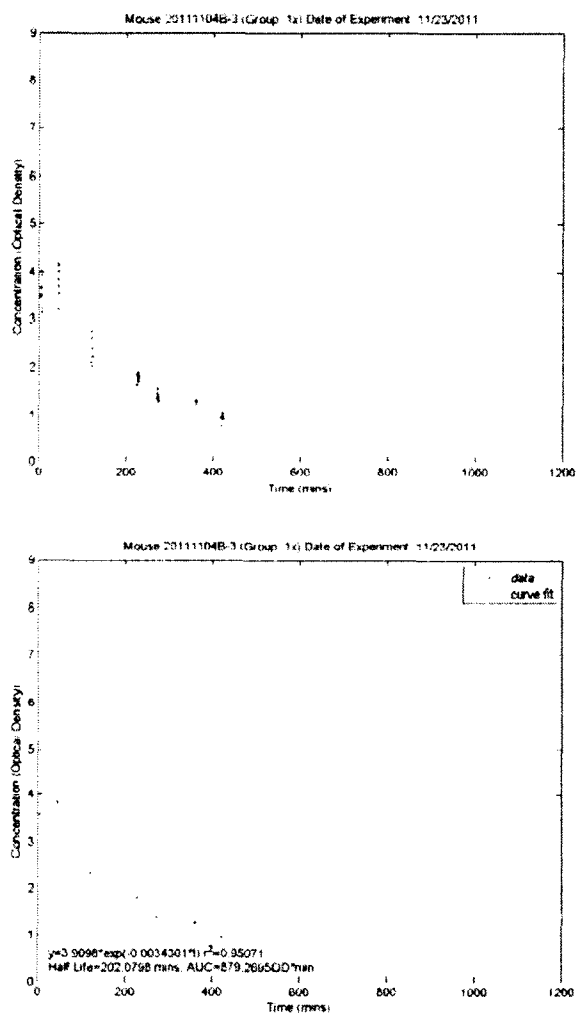
Figure D-3: Charts for mouse 20111104B-3 (Group A- 7.74 PPM). Top: All Data, Bottom: Averaged Data.
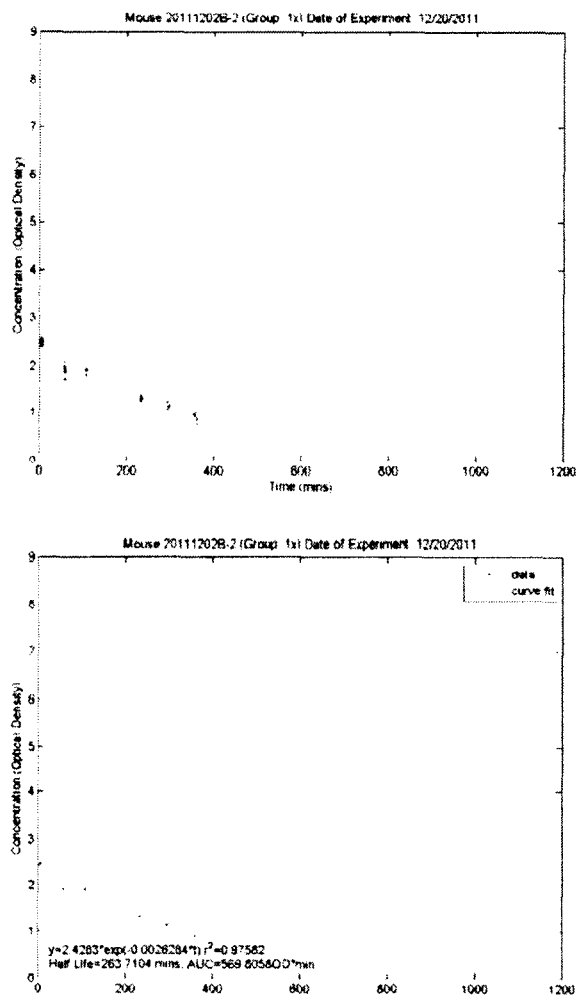
Figure D-4: Charts for mouse 20111202B-2 (Group A-8.44 PPM). Top: All Data, Bottom: Averaged Data.
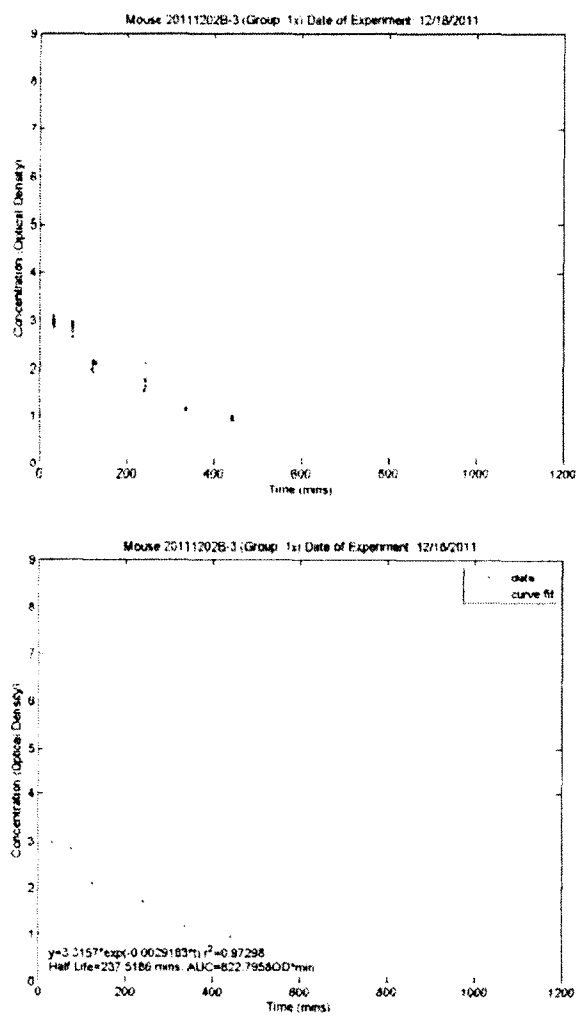
**Figure D-5:** Charts for mouse 20111202B-3 (Group A- 9.46 PPM). Top: All Data, Bottom: Averaged Data.
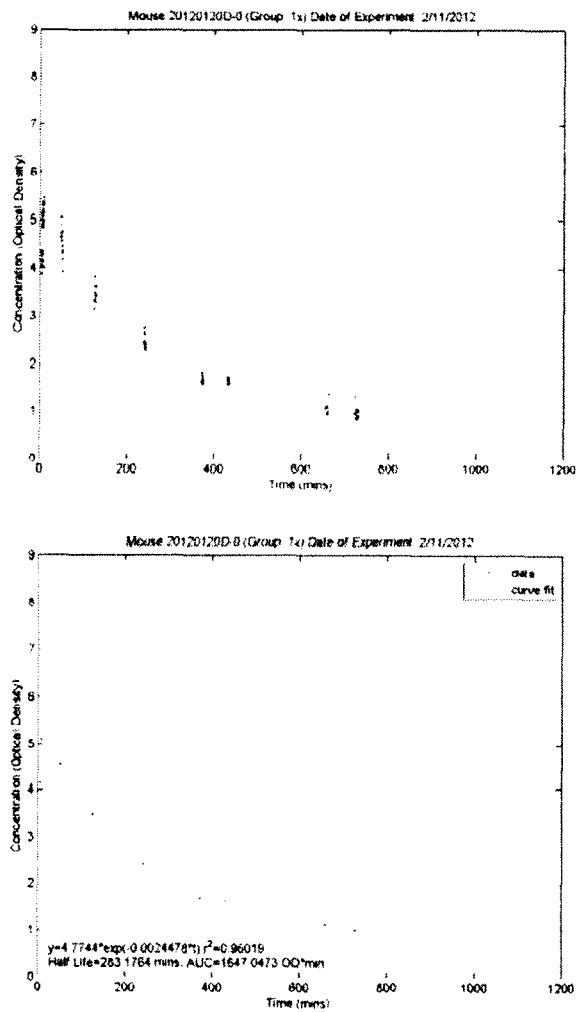
Figure D-6: Charts for mouse 20120120D-0 (Group A- 6.89 PPM). Top: All Data, Bottom: Averaged Data.
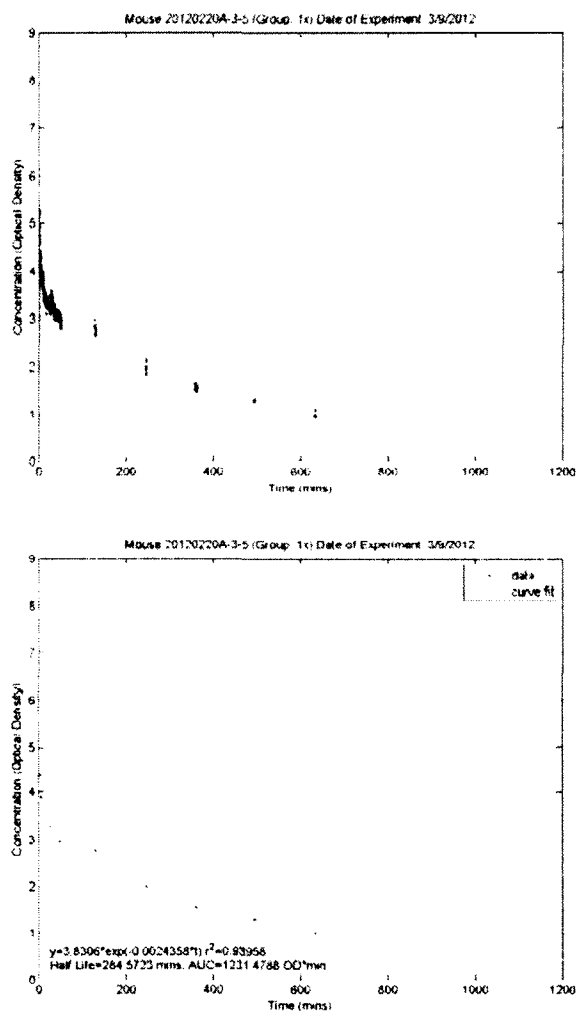
Figure D-7: Charts for mouse 20120220A-3-5 (Group A- 16.69 PPM). Top: All Data, Bottom: Averaged Data.
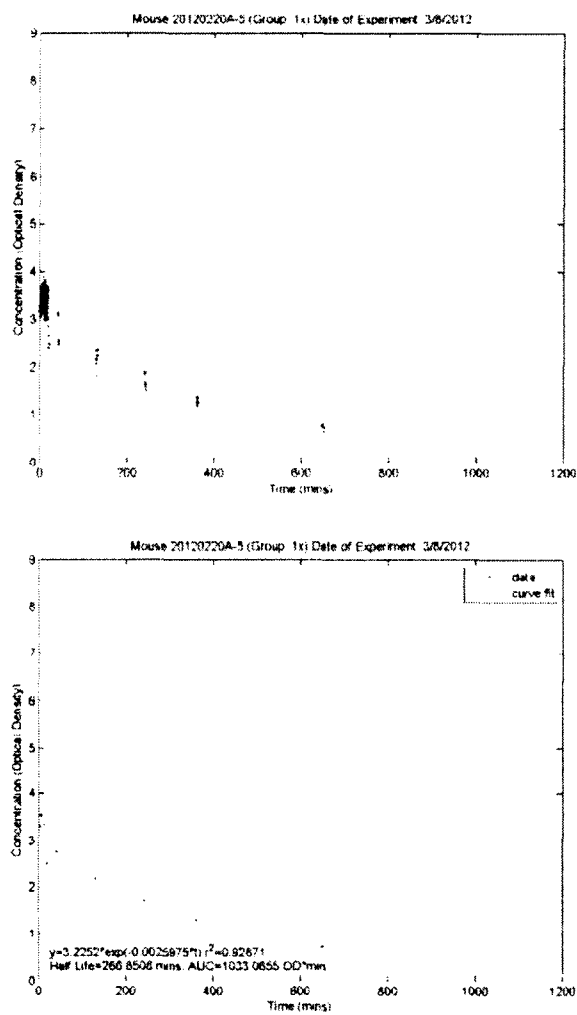
Figure D-8: Charts for mouse 20120220A-5 (Group A- 7.36 PPM). Top: All Data, Bottom: Averaged Data.
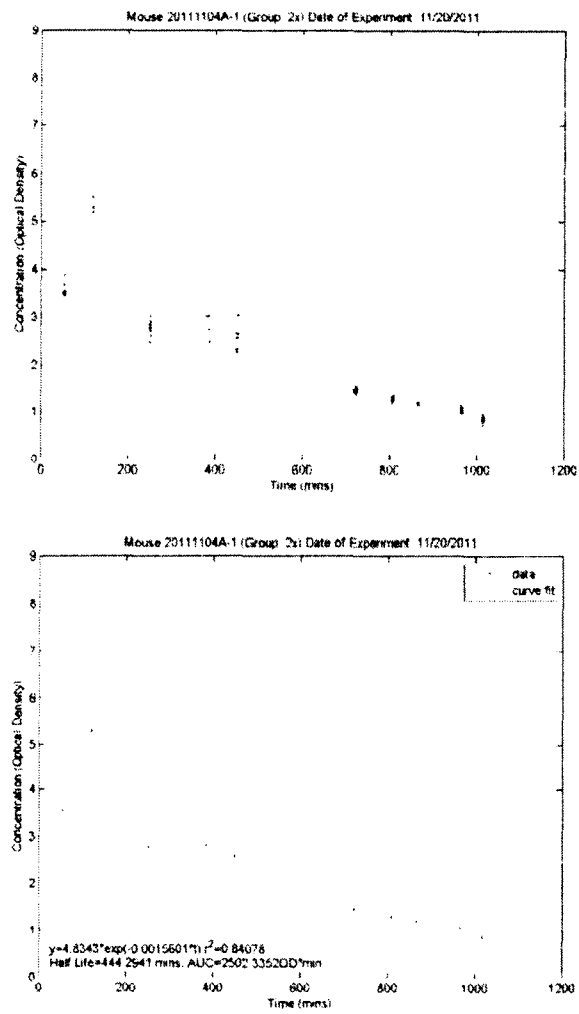
Figure D-9: Charts for mouse 20111104A-1 (Group B-23.59 PPM). Top: All Data, Bottom: Averaged Data.
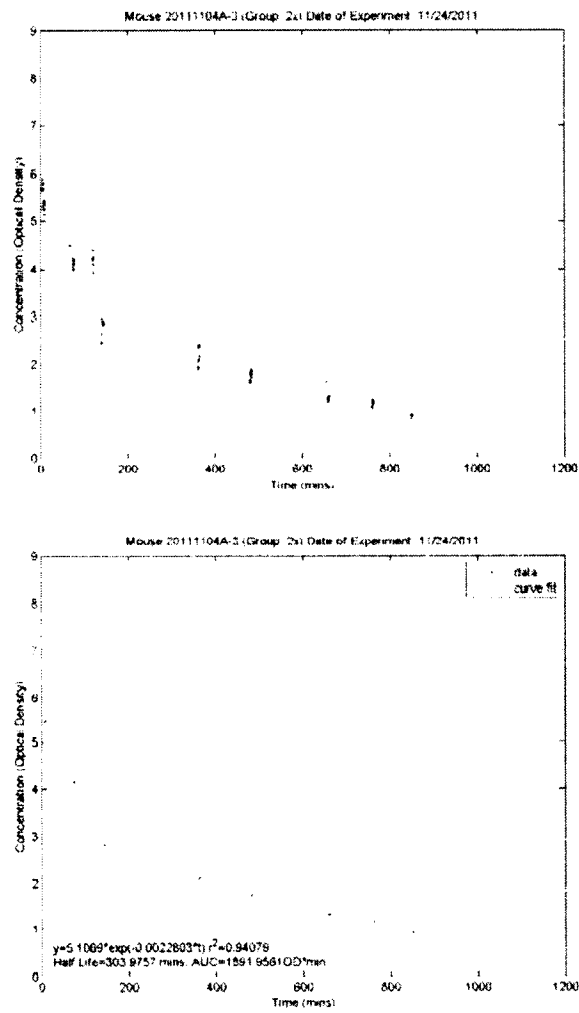
Figure D-10: Charts for mouse 20111104A-3 (Group B- 38.35 PPM). Top: All Data,
Bottom: Averaged Data.
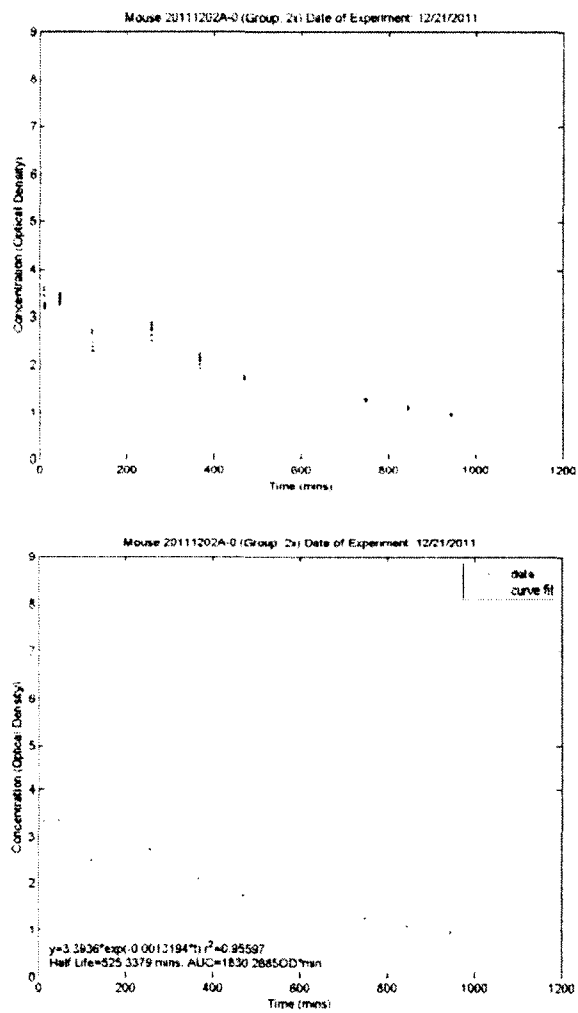
Figure D-11: Charts for mouse 20111202A-0 (Group B- 23.24 PPM). Top: All Data, Bottom: Averaged Data.
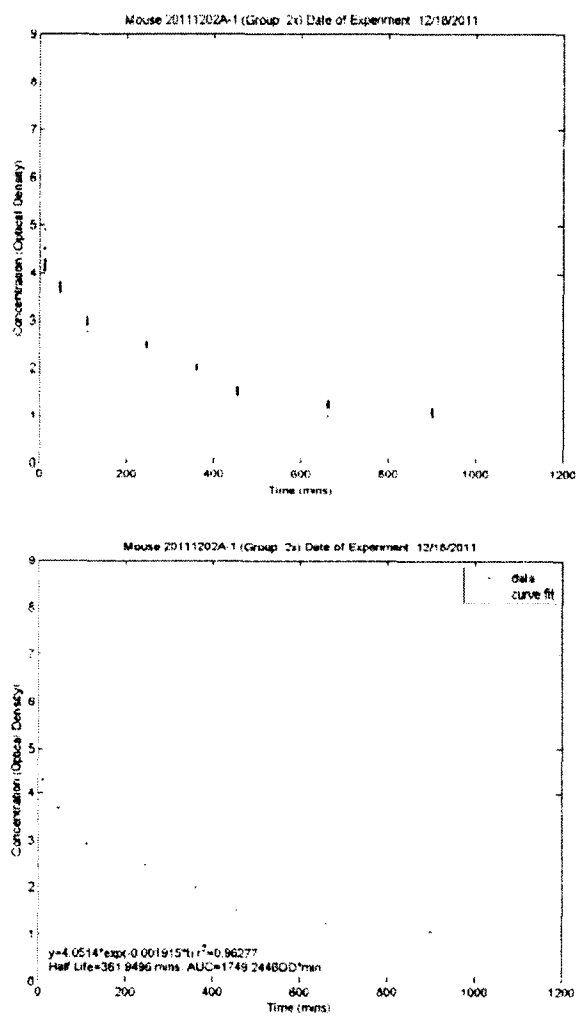
Figure D-12: Charts for mouse 20111202A-1 (Group B- 21.64 PPM). Top: All Data, Bottom: Averaged Data.

Mouse 20111202A-2 (Group 2x) Date of Experiment 12/20/2011

Mouse 20111202A-2 (Group 2x) Date of Experiment 12/20/2011

$y=4.5098 \cdot \exp(-0.0023282 \cdot t)$ $r^2=0.91183$
Half Life=297.7232 mins, AUC=1653.6994 OD*min
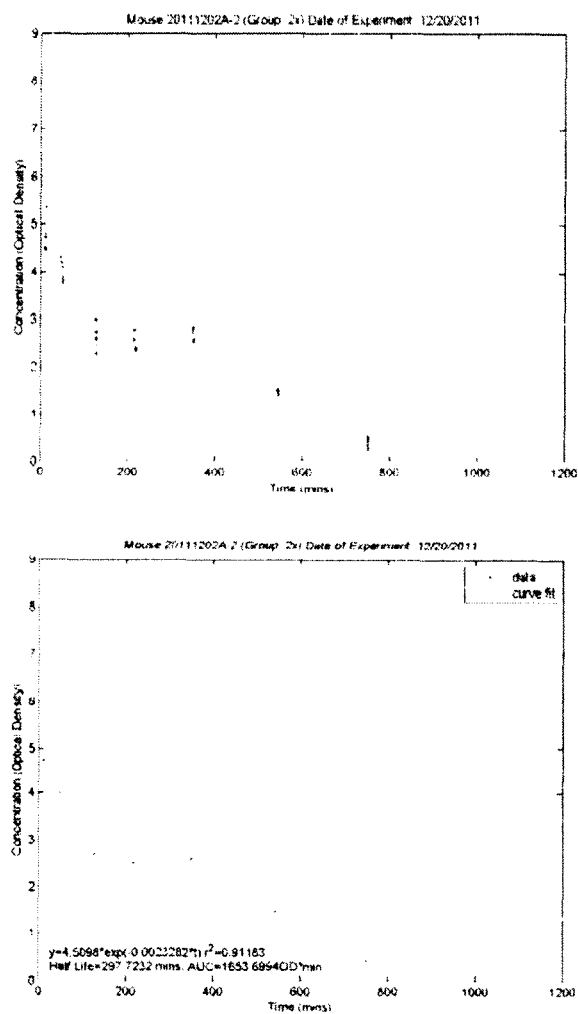
Figure D-13: Charts for mouse 20111202A-2 (Group B- 30.03 PPM). Top: All Data, Bottom: Averaged Data.
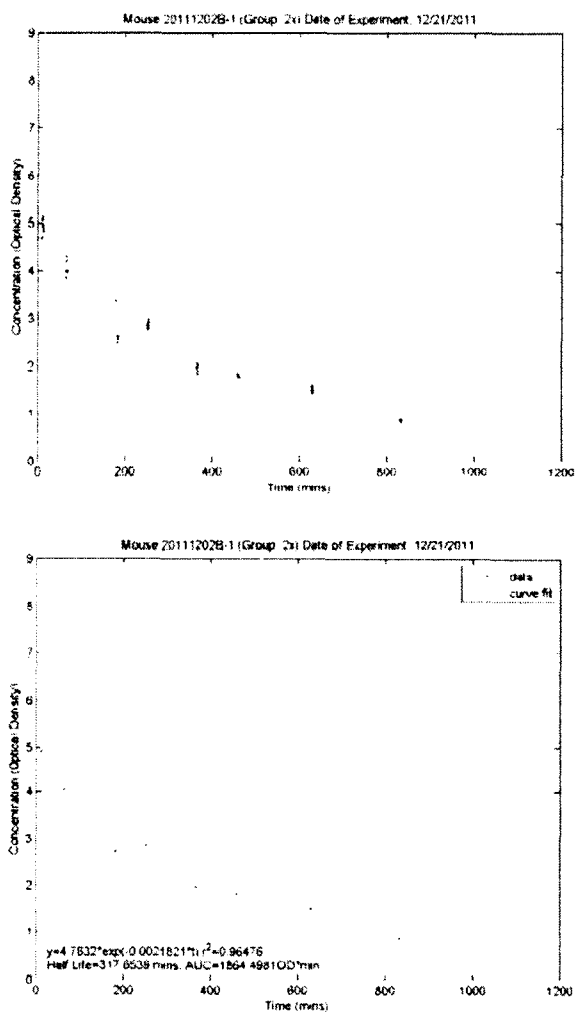
Figure D-14: Charts for mouse 20111202B-1 (Group B- 24.82 PPM). Top: All Data, Bottom: Averaged Data.
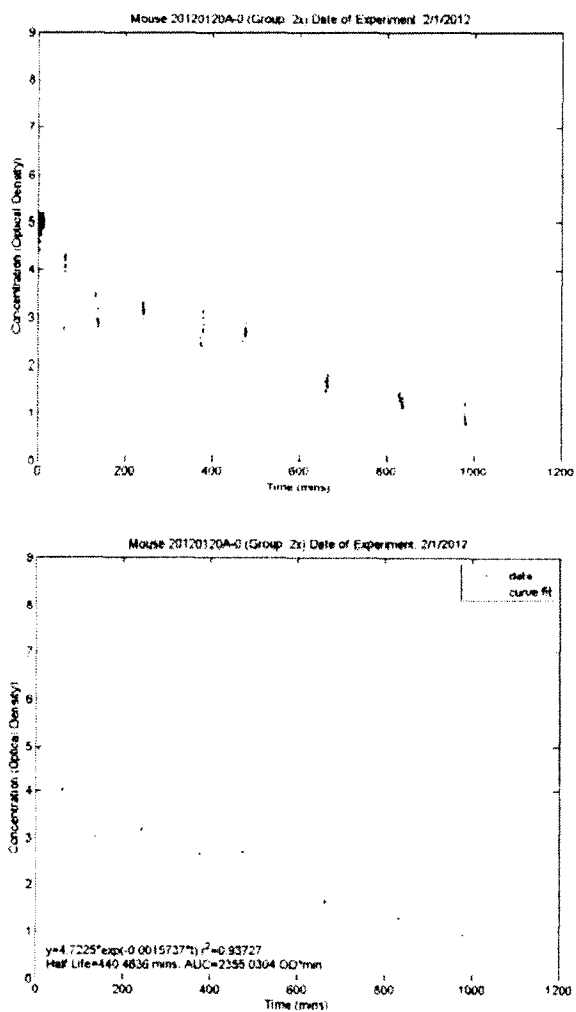
Figure D-15: Charts for mouse 20120120A-0 (Group B- 17.43 PPM). Top: All Data, Bottom: Averaged Data.
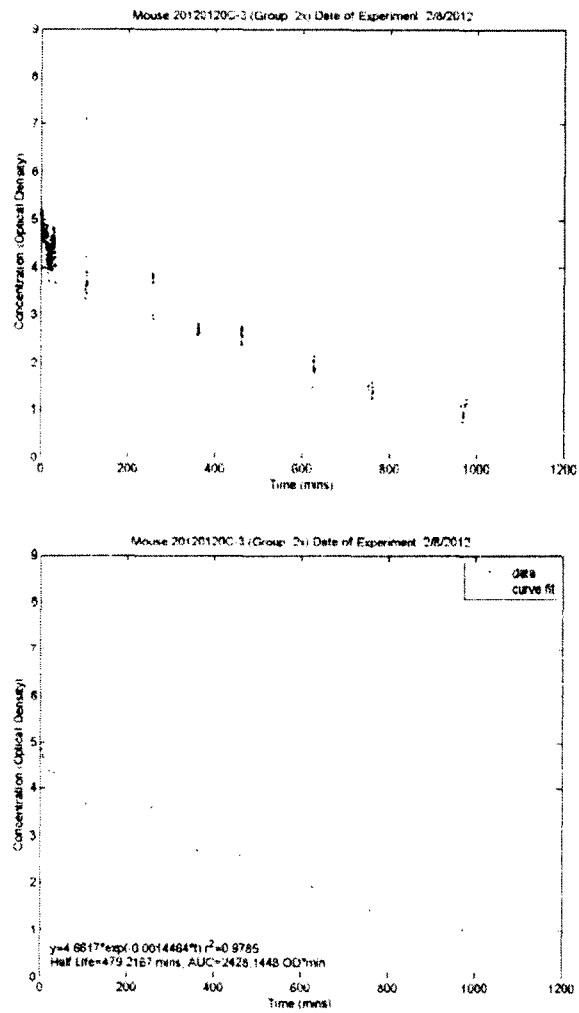
**Figure D-16:** Charts for mouse 20120120C-3 (Group B- 23.30 PPM). Top: All Data, Bottom: Averaged Data.
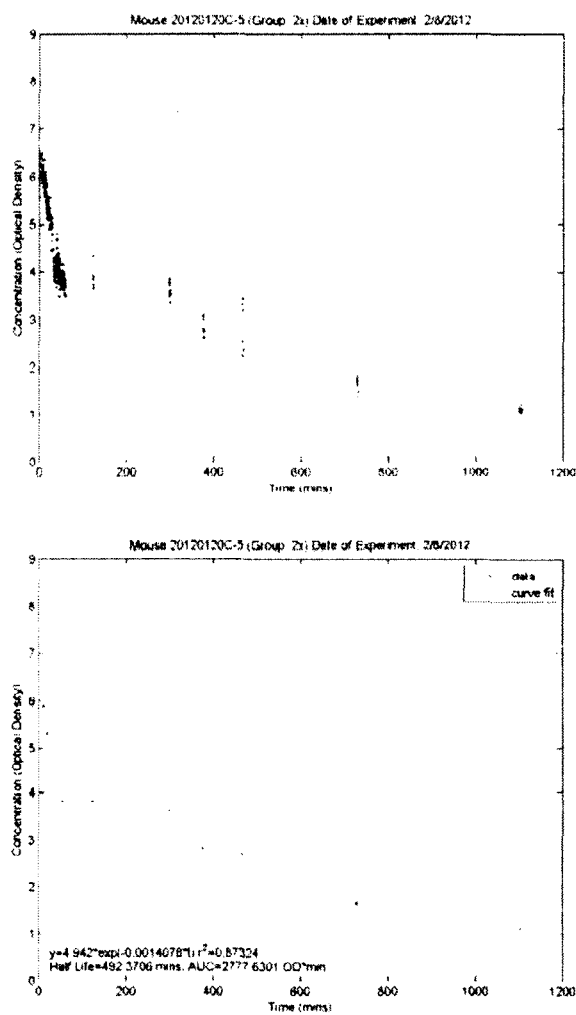
Figure D-17: Charts for mouse 20120120C-5 (Group B- 23.95 PPM). Top: All Data, Bottom: Averaged Data.

APPENDIX E

CONTINUATION OF DATA FOR CHAPTER 7:
OBSERVATION OF COFACTORS ON
PREDICTION OF TUMOR UPTAKE
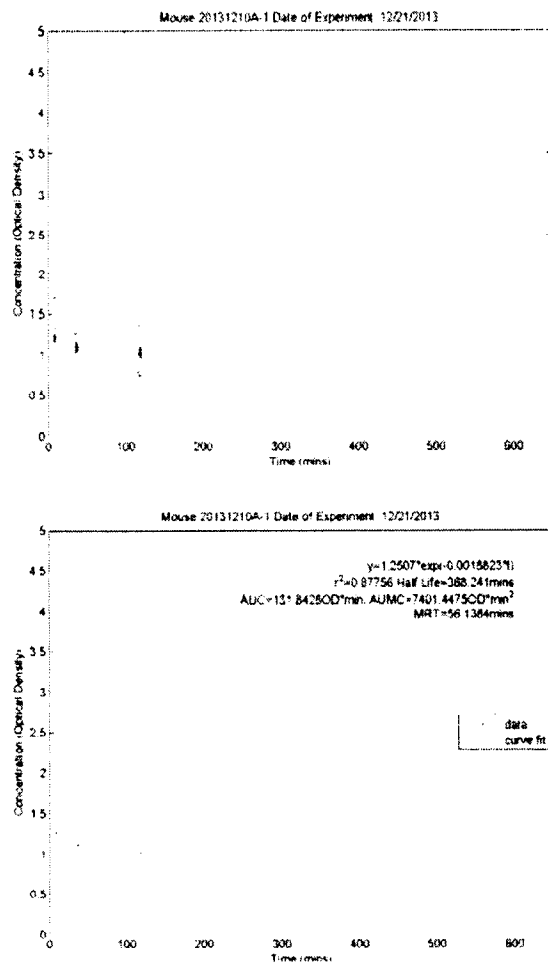
Figure E-1: Charts for mouse 20131210A-1 (hot mouse). Top: All Data, Bottom: Averaged Data.
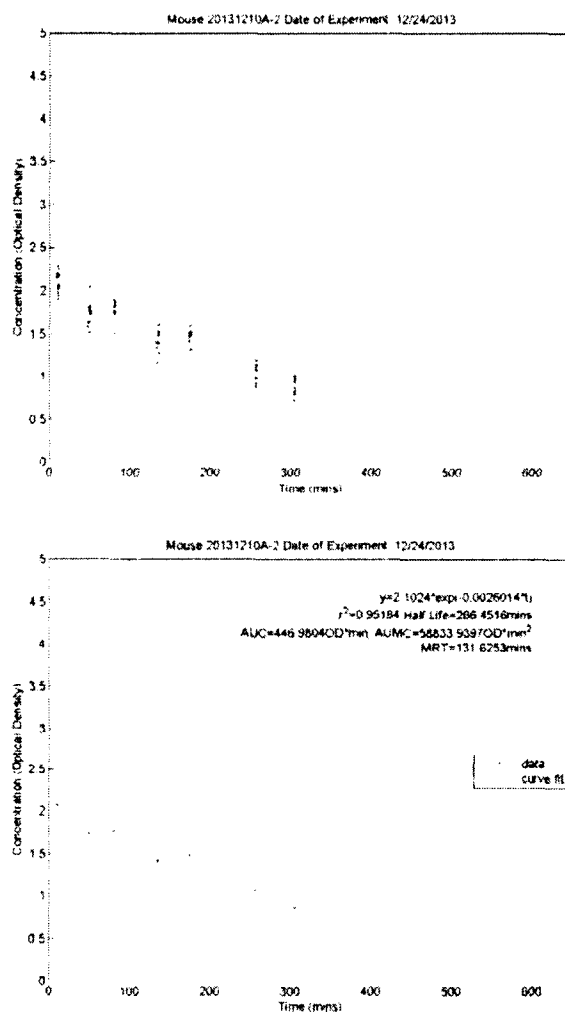
Figure E-2: Charts for mouse 20131210A-2 (cold mouse). Top: All Data, Bottom: Averaged Data.
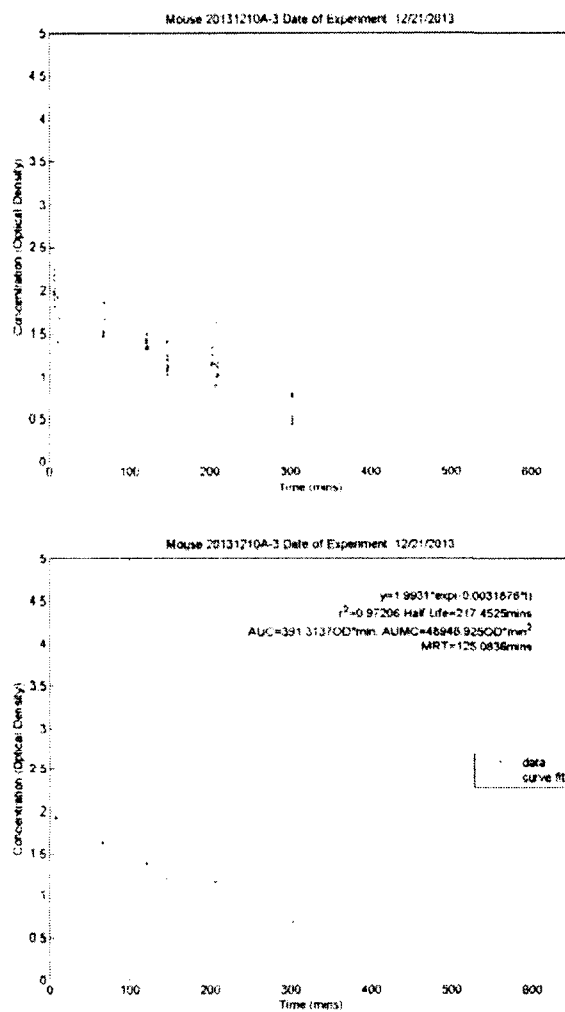
Figure E-3: Charts for mouse 20131210A-3 (cold mouse). Top: All Data, Bottom: Averaged Data.
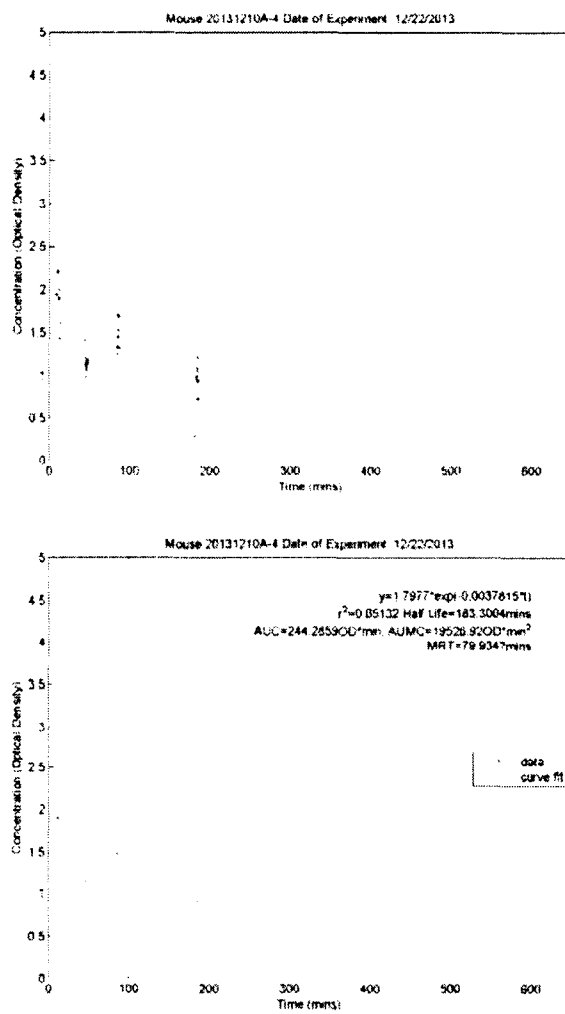
Figure E-4: Charts for mouse 20131210A-4 (hot mouse). Top: All Data, Bottom: Averaged Data.
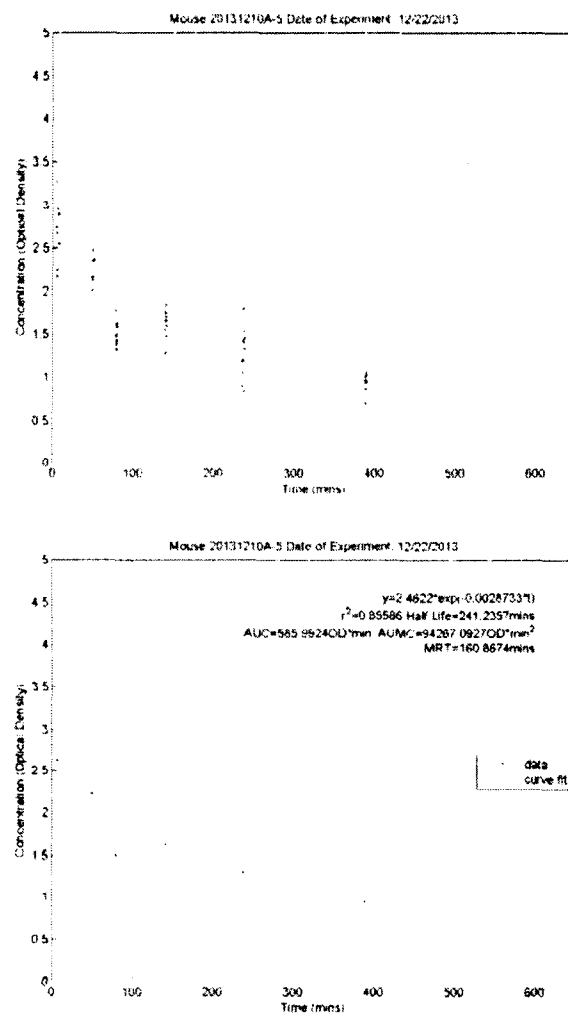
Figure E-5: Charts for mouse 20131210A-5 (cold mouse). Top: All Data, Bottom: Averaged Data.
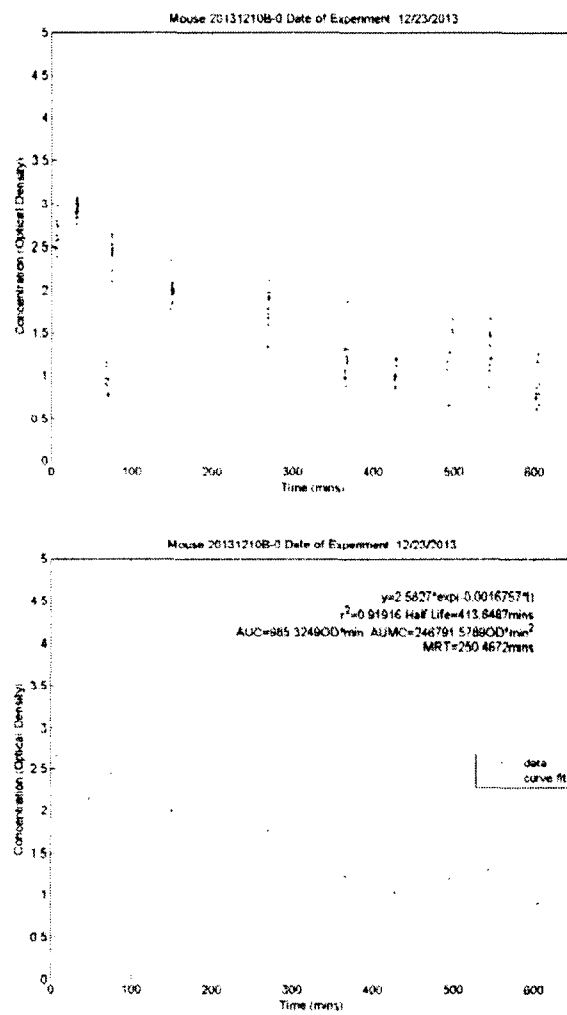
Figure E-6: Charts for mouse 20131210B-0 (hot mouse). Top: All Data, Bottom: Averaged Data.
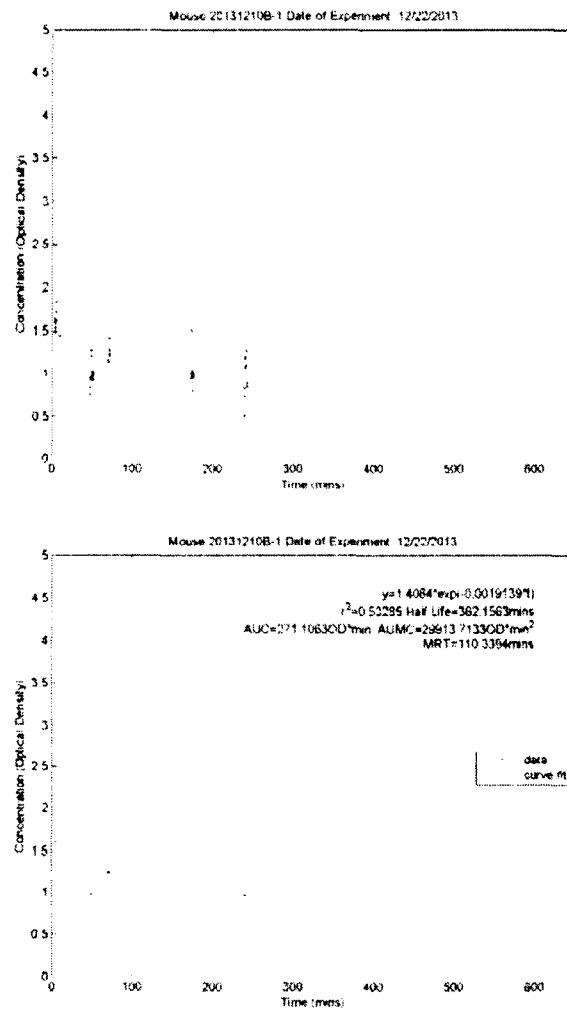
Figure E-7: Charts for mouse 20131210B-1 (hot mouse). Top: All Data, Bottom: Averaged Data.
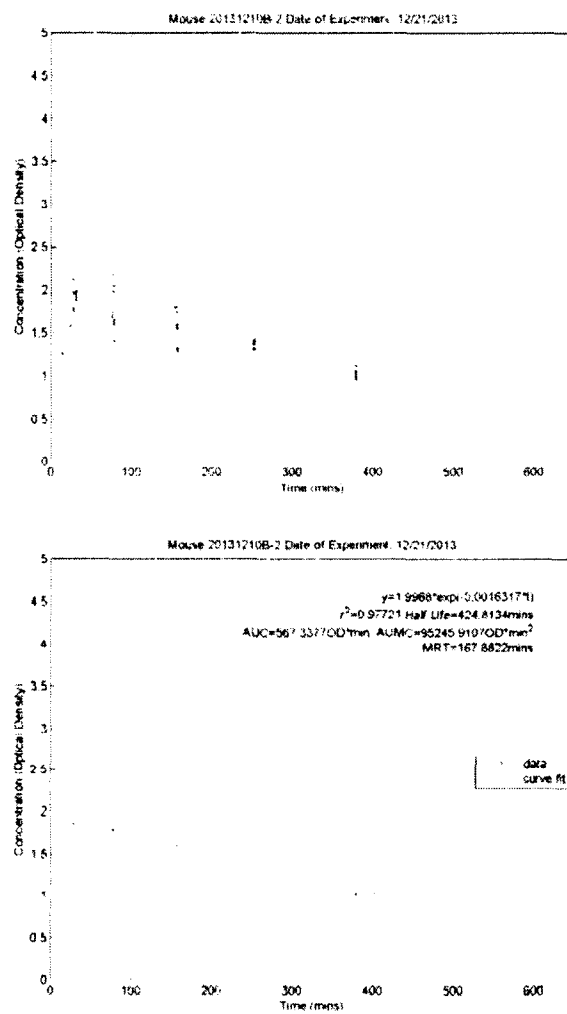
Figure E-8: Charts for mouse 20131210B-2 (hot mouse). Top: All Data, Bottom: Averaged Data.
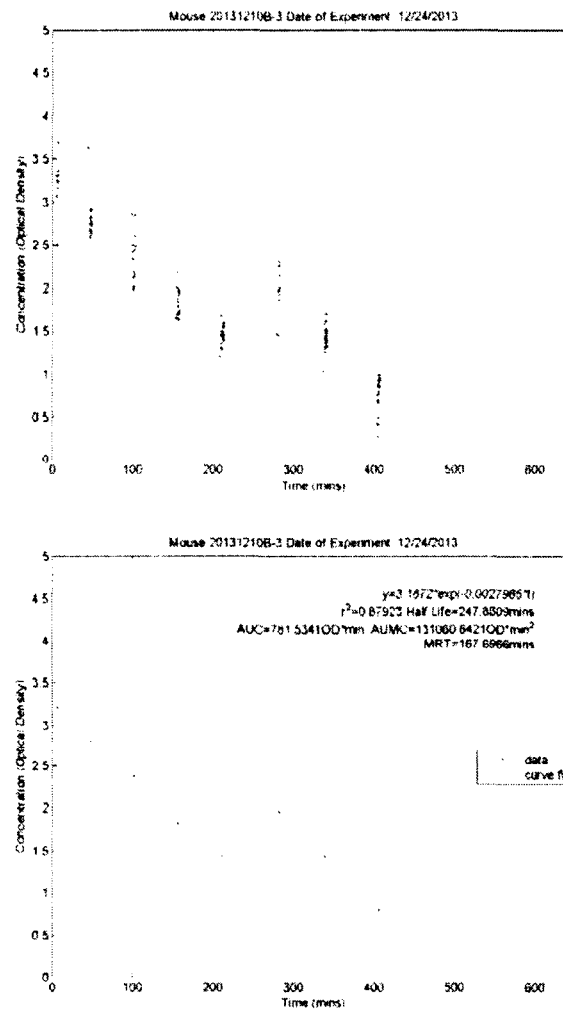
**Figure E-9:** Charts for mouse 20131210B-3 (cold mouse). Top: All Data, Bottom: Averaged Data.

APPENDIX F

INSTITUTIONAL ANIMAL CARE AND USE COMMITTEE APPROVAL LETTER

INSTITUTIONAL ANIMAL CARE AND USE COMMITTEE
Louisiana Tech University

25 October 2011
Dr. Patrick O'Neal, Ph.D.
Biomedical Engineering
Louisiana Tech University
Campus Box # 58

Dear Dr. O'Neal:

The Louisiana Tech University's Institutional Animal Care and Use Committee (IACUC) met on 17 October and approved your amended protocol entitled:

Nanoparticle Tracking For Cancer Therapy

The committee members feel that the transport of mice from Houston that have been inoculated with cancer cells is appropriate, and in keeping with your previous protocols. Please make sure that the animals are in a transport box with adequate water and that the vehicle be air-conditioned at all times so that the animals will not become dehydrated or overheated.

You and the students have been approved for a limit of 50 animals in this initial study beginning 1 November 2011. Please remember that you are required to keep adequate and accurate records of all procedures, results, and the number of animals used in this protocol. You are required to provide a progress report each year by 1 October. If the project should need to be extended beyond 31 October 2014, the third year, you will be required to submit a new protocol. Any changes you need to make in the protocol before the termination date must be submitted to the IACUC on the amendment form for approval before implementation.

Keep for your research records and results for three years after termination of the project. These records must be available for review by the IACUC or state and federal animal use agencies. Each year by 31 October you will be required to complete a summary of number of animals used in this protocol used for the United States Agricultural Agency (USDA). Note that failure to follow this protocol as approved may result in the termination of research. If you have any questions please call me at 318-243-0796 or via e-mail at jgspauld@latech.edu.

Sincerely,

James G. Spaulding, Chair
Louisiana Tech University IACUC

REFERENCES

[1]   American Cancer Society, "Cancer Facts and Figures 2013," American Cancer

       Society, Atlanta, GA, 2013.

[2]   American Cancer Society, "Cancer Treatment & Survivorship Facts & Figures,"

       American Cancer Society, Atlanta, GA, 2012.

[3]   C. M. Croce, "Oncogenes and cancer," *N. Engl. J. Med.*, vol. 358, no. 5, pp. 502–

       511, 2008.

[4]   D. Hanahan and R. A. Weinberg, "The hallmarks of cancer," *Cell*, vol. 100, no. 1,

       pp. 57–70, 2000.

[5]   S. H. Jang, M. G. Wientjes, D. Lu, and J. L.-S. Au, "Drug delivery and transport to

       solid tumors," *Pharm. Res.*, vol. 20, no. 9, pp. 1337–1350, 2003.

[6]   F. Bray, J.-S. Ren, E. Masuyer, and J. Ferlay, "Global estimates of cancer

       prevalence for 27 sites in the adult population in 2008," *Int. J. Cancer*, vol. 132,

       no. 5, pp. 1133–1145, Mar. 2013.

[7]   J. Ferlay, I. Soerjomataram, M. Ervik, S. Eser, C. Mathers, M. Rebelo, D. Parkin,

       D. Forman, and F. Bray, "Cancer Incidence and Mortality Worldwide: IARC

       CancerBase No. 11," International Agency for Research on Cancer, Lyon, France.

[8]   M. Horner, L. Ries, M. Krapcho, N. Neyman, R. Aminou, N. Howlader, S.

       Altekruse, E. Feuer, L. Huang, and A. Mariotto, "SEER Cancer Statistics Review,

       1975-2006, National Cancer Institute. Bethesda, MD," 2009.

[9]   Y.-I. Chang, W.-Y. Cheng, and C.-Y. Gu, "Application of the network model for

        studying the delivery of colloidal drugs," *Colloid Polym. Sci.*, vol. 289, no. 13, pp.

        1479–1492, 2011.

[10]   H. Xue, M. B. Sawyer, P. E. Wischmeyer, and V. E. Baracos, "Nutrition

        modulation of gastrointestinal toxicity related to cancer chemotherapy: From

        preclinical findings to clinical strategy," *J. Parenter. Enter. Nutr.*, vol. 35, no. 1,

        pp. 74–90, 2011.

[11]   M. Soltani and P. Chen, "Numerical modeling of fluid flow in solid tumors," *PLoS

        ONE*, vol. 6, no. 6, 2011.

[12]   R. B. Livingston and F. J. Esteva, "Chemotherapy and Herceptin for HER-2+

        metastatic breast cancer: The best drug?," *Oncologist*, vol. 6, no. 4, pp. 315–316,

        2001.

[13]   R. K. Jain, "Transport of molecules across tumor vasculature," *CANCER

        METASTASIS Rev.*, vol. 6, no. 4, pp. 559–593, 1987.

[14]   R. K. Jain, "Transport of molecules in the tumor interstitium: A review," *Cancer

        Res.*, vol. 47, no. 12, pp. 3039–3051, 1987.

[15]   S. K. Hobbs, W. L. Monsky, F. Yuan, W. G. Roberts, L. Griffith, V. P. Torchilin,

        and R. K. Jain, "Regulation of transport pathways in tumor vessels: Role of tumor

        type and microenvironment," *Proc. Natl. Acad. Sci. U. S. A.*, vol. 95, no. 8, pp.

        4607–4612, 1998.

[16]   R. B. Campbell, "Tumor physiology and delivery of nanopharmaceuticals,"

        Anticancer Agents Med. Chem., vol. 6, no. 6, pp. 503–512, 2006.

[17] W. L. Monsky, D. Fukumura, T. Gohongi, M. Ancukiewcz, H. A. Weich, V. P. Torchilin, F. Yuan, and R. K. Jain, "Augmentation of transvascular transport of macromolecules and nanoparticles in tumors using vascular endothelial growth factor," *Cancer Res.*, vol. 59, no. 16, pp. 4129–4135, 1999.

[18] O. Ishida, K. Maruyama, K. Sasaki, and M. Iwatsuru, "Size-dependent extravasation and interstitial localization of polyethyleneglycol liposomes in solid tumor-bearing mice," *Int. J. Pharm.*, vol. 190, no. 1, pp. 49–56, 1999.

[19] S. T. Stern, J. B. Hall, L. L. Yu, L. J. Wood, G. F. Paciotti, L. Tamarkin, S. E. Long, and S. E. McNeil, "Translational considerations for cancer nanomedicine," *J. Controlled Release*, vol. 146, no. 2, pp. 164–174, 2010.

[20] D. Peer, J. M. Karp, S. Hong, O. C. Farokhzad, R. Margalit, and R. Langer, "Nanocarriers as an emerging platform for cancer therapy," *Nat. Nanotechnol.*, vol. 2, no. 12, pp. 751–760, 2007.

[21] B. Y. S. Kim, J. T. Rutka, and W. C. W. Chan, "Current concepts: Nanomedicine," *N. Engl. J. Med.*, vol. 363, no. 25, pp. 2434–2443, 2010.

[22] J.-L. Li and M. Gu, "Gold-nanoparticle-enhanced cancer photothermal therapy," *IEEE J. Sel. Top. Quantum Electron.*, vol. 16, no. 4, pp. 989–996, 2010.

[23] G. J. Michalak, G. P. Goodrich, J. A. Schwartz, W. D. James, and D. P. O'Neal, "Murine photoplethysmography for in vivo estimation of vascular gold nanoshell concentration," *J. Biomed. Opt.*, vol. 15, no. 4, 2010.

[24] G. J. Michalak, H. A. Anderson, and D. P. O'Neal, "Feasibility of using a two-wavelength photometer to estimate the concentration of circulating near-infrared extinguishing nanoparticles," *J. Biomed. Nanotechnol.*, vol. 6, no. 1, pp. 73–81, 2010.

[25] G. Truskey, *Transport Phenomena in Biological Systems*, 2nd ed. Upper Saddle River, NJ: Prentice Hall, 2004.

[26] M. Al-Olama, A. Wallgren, B. Andersson, K. Gatzinsky, R. Hultborn, A. Karlsson-Parra, S. Lange, H.-A. Hansson, and E. Jennische, "The peptide AF-16 decreases high interstitial fluid pressure in solid tumors," *Acta Oncol.*, vol. 50, no. 7, pp. 1098–1104, 2011.

[27] Z. Amoozgar and Y. Yeo, "Recent advances in stealth coating of nanoparticle drug delivery systems," *Wiley Interdiscip. Rev. Nanomed. Nanobiotechnol.*, vol. 4, no. 2, pp. 219–233, 2012.

[28] V. P. Podduturi, I. B. Magaña, D. P. O'Neal, and P. A. Derosa, "Simulation of transport and extravasation of nanoparticles in tumors which exhibit enhanced permeability and retention effect," *Comput. Methods Programs Biomed.*, vol. 112, no. 1, pp. 58–68, 2013.

[29] G. Kong, R. D. Braun, and M. W. Dewhirst, "Characterization of the effect of hyperthermia on nanoparticle extravasation from tumor vasculature," *Cancer Res.*, vol. 61, no. 7, pp. 3027–3032, 2001.

[30] X. Huang, X. Peng, Y. Wang, Y. Wang, D. M. Shin, M. A. El-Sayed, and S. Nie, "A reexamination of active and passive tumor targeting by using rod-shaped gold nanocrystals and covalently conjugated peptide ligands," *ACS Nano*, vol. 4, no. 10, pp. 5887–5896, 2010.

[31] T. M. Allen, W. W. K. Cheng, J. I. Hare, and K. M. Laginha, "Pharmacokinetics and pharmacodynamics of lipidic nano-particles in cancer," *Anticancer Agents Med. Chem.*, vol. 6, no. 6, pp. 513–523, 2006.

[32] J. R. Tauro and R. A. Gemeinhart, "Matrix metalloprotease triggered delivery of cancer chemotherapeutics from hydrogel matrixes," *Bioconjug. Chem.*, vol. 16, no. 5, pp. 1133–1139, 2005.

[33] E. Brewer, J. Coleman, and A. Lowman, "Emerging technologies of polymeric nanoparticles in cancer drug delivery," *J. Nanomater.*, vol. 2011, 2011.

[34] S. C. A. Michel, T. M. Keller, J. M. Fröhlich, D. Fink, R. Caduff, B. Seifert, B. Marincek, and R. A. Kubik-Huch, "Preoperative breast cancer staging: MR imaging of the axilla with ultrasmall superparamagnetic iron oxide enhancement," *Radiology*, vol. 225, no. 2, pp. 527–536, 2002.

[35] E. S. Day, J. G. Morton, and J. L. West, "Nanoparticles for thermal cancer therapy," *J. Biomech. Eng.*, vol. 131, no. 7, 2009.

[36] G. J. Michalak, J. A. Schwartz, G. P. Goodrich, and D. P. O'Neal, "Three-wavelength murine photoplethysmography for estimation of vascular gold nanorod concentration," *Opt. Express*, vol. 18, no. 25, pp. 26535–26549, 2010.

[37] G. P. Goodrich, L. Bao, K. Gill-Sharp, K. L. Sang, J. Wang, and J. Donald Payne,
      "Photothermal therapy in a murine colon cancer model using near-infrared
      absorbing gold nanorods," *J. Biomed. Opt.*, vol. 15, no. 1, 2010.

[38] J. R. Cole, N. A. Mirin, M. W. Knight, G. P. Goodrich, and N. J. Halas,
      "Photothermal efficiencies of nanoshells and nanorods for clinical therapeutic
      applications," *J. Phys. Chem. C*, vol. 113, no. 28, pp. 12090–12094, 2009.

[39] S. Oldenburg, R. Averitt, S. Westcott, and N. Halas, "Nanoengineering of optical
      resonances," *Chem. Phys. Lett.*, vol. 288, no. 2, pp. 243–247, 1998.

[40] W. D. James, L. R. Hirsch, J. L. West, P. D. O'Neal, and J. D. Payne, "Application
      of INAA to the build-up and clearance of gold nanoshells in clinical studies in
      mice," *J. Radioanal. Nucl. Chem.*, vol. 271, no. 2, pp. 455–459, 2007.

[41] N. R. Jana, L. Gearheart, and C. J. Murphy, "Wet chemical synthesis of high
      aspect ratio cylindrical gold nanorods," *J. Phys. Chem. B*, vol. 105, no. 19, pp.
      4065–4067, 2001.

[42] C. J. Murphy, T. K. Sau, A. M. Gole, C. J. Orendorff, J. Gao, L. Gou, S. E.
      Hunyadi, and T. Li, "Anisotropic metal nanoparticles: synthesis, assembly, and
      optical applications," *J. Phys. Chem. B*, vol. 109, no. 29, pp. 13857–13870, 2005.

[43] J. M. Tucker-Schwartz, K. R. Beavers, W. W. Sit, A. T. Shah, C. L. Duvall, and
      M. C. Skala, "In vivo imaging of nanoparticle delivery and tumor microvasculature
      with multimodal optical coherence tomography," *Biomed. Opt. Express*, vol. 5, no.
      6, pp. 1731–1743, 2014.

[44] D. E. Owens III and N. A. Peppas. "Opsonization, biodistribution, and pharmacokinetics of polymeric nanoparticles," *Int. J. Pharm.*, vol. 307, no. 1, pp. 93–102, 2006.

[45] X. Yan, G. L. Scherphof, and J. A. A. M. Kamps, "Liposome opsonization," *J. Liposome Res.*, vol. 15, no. 1–2, pp. 109–139, 2005.

[46] T. Ishida, R. Maeda, M. Ichihara, K. Irimura, and H. Kiwada, "Accelerated clearance of PEGylated liposomes in rats after repeated injections," *J. Controlled Release*, vol. 88, no. 1, pp. 35–42, 2003.

[47] E. T. M. Dams, P. Laverman, W. J. G. Oyen, G. Storm, G. L. Scherphof, J. W. M. Van Der Meer, F. H. M. Corstens, and O. C. Boerman, "Accelerated blood clearance and altered biodistribution of repeated injections of sterically stabilized liposomes," *J. Pharmacol. Exp. Ther.*, vol. 292, no. 3, pp. 1071–1079, 2000.

[48] T. Ishida, X. Wang, T. Shimizu, K. Nawata, and H. Kiwada, "PEGylated liposomes elicit an anti-PEG IgM response in a T cell-independent manner," *J. Controlled Release*, vol. 122, no. 3, pp. 349–355, 2007.

[49] J. K. Armstrong, G. Hempel, S. Koling, L. S. Chan, T. Fisher, H. J. Meiselman, and G. Garratty, "Antibody against poly(ethylene glycol) adversely affects PEG-asparaginase therapy in acute lymphoblastic leukemia patients," *Cancer*, vol. 110, no. 1, pp. 103–111, 2007.

[50] M. Ichihara, T. Shimizu, A. Imoto, Y. Hashiguchi, Y. Uehara, T. Ishida, and H. Kiwada, "Anti-PEG IgM response against PEGylated liposomes in mice and rats," *Pharmaceutics*, vol. 3, no. 1, pp. 1–11, 2011.

[51] T. Ishida, S. Kashima, and H. Kiwada, "The contribution of phagocytic activity of liver macrophages to the accelerated blood clearance (ABC) phenomenon of PEGylated liposomes in rats," *J. Controlled Release*, vol. 126, no. 2, pp. 162–165, 2008.

[52] R. Notari, *Biopharmaceutics and Pharmacokinetics; an Introduction*. New York, NY: Marcel Dekker Inc., 1971.

[53] W. H. De Jong, W. I. Hagens, P. Krystek, M. C. Burger, A. J. A. M. Sips, and R. E. Geertsma, "Particle size-dependent organ distribution of gold nanoparticles after intravenous administration." *Biomaterials*, vol. 29, no. 12, pp. 1912–1919, 2008.

[54] L. Aarons, "Population pharmacokinetics: theory and practice.," *Br. J. Clin. Pharmacol.*, vol. 32, no. 6, pp. 669–670, 1991.

[55] D. P. O'Neal, L. R. Hirsch, N. J. Halas, J. D. Payne, and J. L. West, "Photo-thermal tumor ablation in mice using near infrared-absorbing nanoparticles," *Cancer Lett.*, vol. 209, no. 2, pp. 171–176, 2004.

[56] G. Hoffman, "Methods of Analysis by the U.S. Geological Survey National Water Quality LAboratory- Preparation Procedure for Aquatic Biological Material Determined for Trace Metals." U.S. Department of the Interior, Denver, CO, Open-File Report 96-362, 1996.

[57] J. Anzelmo, A. Seyfarth, and L. Arias, "Approaching a Universal Sample Preparation Method for XRF Analysis of Powder Materials," *Diffr. Data*, vol. 44, pp. 368–373, 2001.

[58] J. Börjesson and S. Mattsson, "Medical applications of X-ray fluorescence for trace element research," *Powder Diffr.*, vol. 22, no. 2, pp. 130–137, 2007.

[59] J. Scott and S. Lillicrap, "133Xe for the x-ray fluorescence assessment of gold in vivo," *Phys. Med. Biol.*, vol. 33, no. 7, pp. 859–864, 1988.

[60] M. Szczerbowska-Boruchowska, "Sample thickness considerations for quantitative X-ray fluorescence analysis of the soft and skeletal tissues of the human body - theoretical evaluation and experimental validation," *X-Ray Spectrom.*, vol. 41, no. 5, pp. 328–337, 2012.

[61] J. Bacso, I. Uzonyi, and B. Dezso, "Determination of gold accumulation in human tissues caused by gold therapy using x-ray fluorescence analysis," *Appl. Radiat. Isot.*, vol. 39, no. 4, pp. 323–326, 1988.

[62] "Terminology for nanomaterials," British Standards Institution, Publically Available Specification PAS 136:2007, 2004.

[63] R. K. Jain, R. T. Tong, and L. L. Munn, "Effect of vascular normalization by antiangiogenic therapy on interstitial hypertension, peritumor edema, and lymphatic metastasis: Insights from a mathematical model," *Cancer Res.*, vol. 67, no. 6, pp. 2729–2735, 2007.

[64] S. J. Chapman, R. J. Shipley, and R. Jawad, "Multiscale modeling of fluid transport in tumors," *Bull. Math. Biol.*, vol. 70, no. 8, pp. 2334–2357, 2008.

[65] H. B. Frieboes, X. Zheng, C.-H. Sun, B. Tromberg, R. Gatenby, and V. Cristini, "An integrated computational/experimental model of tumor invasion," *Cancer Res.*, vol. 66, no. 3, pp. 1597–1604, 2006.

[66] D. M. Howard, K. J. Kearfott, S. J. Wilderman, and Y. K. Dewaraja, "Comparison of I-131 radioimmunotherapy tumor dosimetry: Unit density sphere model versus patient-specific monte carlo calculations," *Cancer Biother. Radiopharm.*, vol. 26, no. 5, pp. 615–621, 2011.

[67] Y.-M. F. Goh, H. L. Kong, and C.-H. Wang, "Simulation of the delivery of doxorubicin to hepatoma," *Pharm. Res.*, vol. 18, no. 6, pp. 761–770, 2001.

[68] R. K. Jain and L. T. Baxter, "Mechanisms of heterogeneous distribution of monoclonal antibodies and other macromolecules in tumors: Significance of elevated interstitial pressure." *Cancer Res.*, vol. 48, no. 24 I, pp. 7022–7032, 1988.

[69] J. Scallan, V. H. Huxley, and R. J. Korthuis, "Capillary fluid exchange: regulation, functions, and pathology," presented at the Colloquium Lectures on Integrated Systems Physiology-\ nl\ hspace* 18pt From Molecules to Function, 2010, vol. 2, pp. 1–94.

[70] L. Xiaoxiao, W. Wangyi, W. Gongbi, and C. Jiaoguo, "Mass transport in solid tumors (I) - Fluid dynamics." *Appl. Math. Mech. Engl. Ed.*, vol. 19, no. 11, pp. 1025–1032, 1998.

[71] T. T. Goodman, J. Chen, K. Matveev, and S. H. Pun, "Spatio-temporal modeling of nanoparticle delivery to multicellular tumor spheroids," *Biotechnol. Bioeng.*, vol. 101, no. 2, pp. 388–399, 2008.

[72] T. Stylianopoulos, B. Diop-Frimpong, L. L. Munn, and R. K. Jain, "Diffusion anisotropy in collagen gels and tumors: The effect of fiber network orientation," *Biophys. J.*, vol. 99, no. 10, pp. 3119–3128, 2010.

[73] H. B. Frieboes, M. Wu, J. Lowengrub, P. Decuzzi, and V. Cristini, "A

      Computational Model for Predicting Nanoparticle Accumulation in Tumor

      Vasculature," *PLoS ONE*, vol. 8, no. 2, 2013.

[74] S. Mishra, V. K. Katiyar, and V. Arora, "Mathematical modeling of chemotherapy

      strategies in vascular tumor growth using nanoparticles," *Appl. Math. Comput.*,

      vol. 189, no. 2, pp. 1246–1254, 2007.

[75] A. L. Van De Ven, P. Kim, O. Haley, J. R. Fakhoury, G. Adriani, J. Schmulen, P.

      Moloney, F. Hussain, M. Ferrari, X. Liu, S.-H. Yun, and P. Decuzzi, "Rapid

      tumoritropic accumulation of systemically injected plateloid particles and their

      biodistribution," *J. Controlled Release*, vol. 158, no. 1, pp. 148–155, 2012.

[76] G. Kong, R. D. Braun, and M. W. Dewhirst, "Hyperthermia enables tumor-specific

      nanoparticle delivery: Effect of particle size," *Cancer Res.*, vol. 60, no. 16, pp.

      4440–4445, 2000.

[77] G. S. Kwon, "Polymeric micelles for delivery of poorly water-soluble

      compounds," *Crit. Rev. Ther. Drug Carr. Syst.*, vol. 20, no. 5, 2003.

[78] B. S. Zolnik and N. Sadrieh, "Regulatory perspective on the importance of ADME

      assessment of nanoscale material containing drugs," *Adv. Drug Deliv. Rev.*, vol.

      61, no. 6, pp. 422–427, 2009.

[79] P. Adhikari, S. S. Bracey, K. A. Evans, I. B. Magana, and D. P. O'Neal, "LQR

      tracking of a delay differential equation model for the study of nanoparticle dosing

      strategies for cancer therapy," 2013, pp. 2068–2073.

[80] M. M. Appenheimer, Q. Chen, R. A. Girard, W.-C. Wang, and S. S. Evans, "Impact of fever-range thermal stress on lymphocyte-endothelial adhesion and lymphocyte trafficking," *Immunol. Invest.*, vol. 34, no. 3, pp. 295–323, 2005.

[81] I. Magaña, M. Carroll, A. Rodgers, and P. O'Neal, "Intravascular Bioavailability of Therapeutic Nanoparticles as a Function of Hyperthermia and Injection Rate," in *International Journal of Medical Implants and Devices*, 2011, vol. 5, p. 69.

[82] K. Ricketts, A. Castoldi, C. Guazzoni, C. Ozkan, C. Christodoulou, A. P. Gibson, and G. J. Royle, "A quantitative x-ray detection system for gold nanoparticle tumour biomarkers," *Phys. Med. Biol.*, vol. 57, no. 17, pp. 5443–5555, 2012.

[83] I. B. Magaña, P. Adhikari, M. C. Smalley, S. E. Eklund, and D. P. O'Neal, "Feasibility of energy dispersive X-ray fluorescence determination of gold in soft tissue for clinical applications," *Anal. Methods*, vol. 5, no. 12, pp. 3148–3151, 2013.

[84] S. Nie, "Editorial: Understanding and overcoming major barriers in cancer nanomedicine," *Nanomed.*, vol. 5, no. 4, pp. 523–528, 2010.

[85] M. Amiji, "Nanotechnology- Improving Targeted Delivery," 2007.

[86] I. B. Magaña, P. Adhikari, R. B. Yendluri, G. P. Goodrich, J. A. Schwartz, and D. P. O'Neal, "The use of real-time optical feedback to improve outcomes," presented at the Progress in Biomedical Optics and Imaging - Proceedings of SPIE, 2014, vol. 8955.

[87] T. Ishida, H. Harashima, and H. Kiwada, "Liposome clearance," *Biosci. Rep.*, vol. 22, no. 2, pp. 197–224, 2002.

[88] J. A. Tate, A. A. Petryk, A. J. Giustini, and P. J. Hoopes, "In vivo biodistribution of iron oxide nanoparticles: An overview," presented at the Progress in Biomedical Optics and Imaging - Proceedings of SPIE, 2011, vol. 7901.

[89] J. C. Y. Kah, K. Y. Wong, K. G. Neoh, J. H. Song, J. W. P. Fu, S. Mhaisalkar, M. Olivo, and C. J. R. Sheppard, "Critical parameters in the pegylation of gold nanoshells for biomedical applications: An in vitro macrophage study," *J. Drug Target.*, vol. 17, no. 3, pp. 181–193, 2009.

[90] G. Prencipe, S. M. Tabakman, K. Welsher, Z. Liu, A. P. Goodwin, L. Zhang, J. Henry, and H. Dai, "PEG branched polymer for functionalization of nanomaterials with ultralong blood circulation," *J. Am. Chem. Soc.*, vol. 131, no. 13, pp. 4783–4787, 2009.

[91] M. L. Schipper, G. Iyer, A. L. Koh, Z. Cheng, Y. Ebenstein, A. Aharoni, S. Keren, L. A. Bentolila, J. Li, J. Rao, X. Chen, U. Banin, A. M. Wu, R. Sinclair, S. Weiss, and S. S. Gambhir, "Particle size, surface coating, and PEGylation influence the biodistribution of quantum dots in living mice," *Small*, vol. 5, no. 1, pp. 126–134, 2009.

[92] L. M. Kaminskas, B. D. Kelly, V. M. McLeod, G. Sberna, D. J. Owen, B. J. Boyd, and C. J. H. Porter, "Characterisation and tumour targeting of PEGylated polylysine dendrimers bearing doxorubicin via a pH labile linker," *J. Controlled Release*, vol. 152, no. 2, pp. 241–248, 2011.

[93] K. Xiao, Y. Li, J. Luo, J. S. Lee, W. Xiao, A. M. Gonik, R. G. Agarwal, and K. S.

Lam, "The effect of surface charge on in vivo biodistribution of PEG-oligocholic

acid based micellar nanoparticles," *Biomaterials*, vol. 32, no. 13, pp. 3435–3446,

2011.

[94] R. L. Souhami, H. M. Patel, and B. E. Ryman, "The effect of reticuloendothelial

blockade on the blood clearance and tissue distribution of liposomes," *Biochim.

Biophys. Acta*, vol. 674, no. 3, pp. 354–371, 1981.

[95] N. Van Rooijen and A. Sanders, "Kupffer cell depletion by liposome-delivered

drugs: Comparative activity of intracellular clodronate, propamidine, and

ethylenediaminetetraacetic acid," *Hepatology*, vol. 23, no. 5, pp. 1239–1243, 1996.

[96] V. M. Rumjanek, S. R. Watson, and V. S. Sljivic, "A re-evaluation of the role of

macrophages in carrageenan induced immunosuppression," *Immunology*, vol. 33,

no. 3, pp. 423–432, 1977.

[97] C. Schleicher, J. C. Baas, H. Elser, H. A. Baba, and N. Senninger,

"Reticuloendothelial system blockade promotes progression from mild to severe

acute pancreatitis in the opossum," *Ann. Surg.*, vol. 233, no. 4, pp. 528–536, 2001.

[98] R. B. Yendluri, *Prolonging the circulation time of gold nanoparticles using

[lambda]-carrageenan as a reticuloendothelial system blocking agent.* 2013.

[99] D. J. Lunn, A. Thomas, N. Best, and D. Spiegelhalter, "WinBUGS - A Bayesian

modelling framework: Concepts, structure, and extensibility," *Stat. Comput.*, vol.

10, no. 4, pp. 325–337, 2000.

[100] S. Sturtz, U. Ligges, and A. Gelman, "R2WinBUGS: A package for running

WinBUGS from R," *J. Stat. Softw.*, vol. 12, pp. 1–16, 2005.